2019

DEVELOPMENT OF A PAPER-BASED MICROFLUIDIC DEVICE FOR THE DETECTION OF ORTHOPHOSPHATE IN WATER

Brenno Ribeiro
University of Rhode Island, brenno_ribeiro@my.uri.edu

DEVELOPMENT OF A PAPER-BASED MICROFLUIDIC DEVICE FOR THE DETECTION OF ORTHOPHOSPHATE IN WATER

BY

BRENNO RIBEIRO

A THESIS SUBMITTED IN PARTIAL FULFILLMENT OF THE

REQUIREMENTS FOR THE DEGREE OF

MASTER OF SCIENCE

IN

MECHANICAL ENGINEERING

UNIVERSITY OF RHODE ISLAND

2019

MASTER OF SCIENCE THESIS

OF

BRENNO RIBEIRO

APPROVED:

Thesis Committee:

Major Professor Mohammad Faghri

Constantine Anagnostopoulos

Stephen Powers

Yi Zheng

Nasser H. Zawia

DEAN OF THE GRADUATE SCHOOL

UNIVERSITY OF RHODE ISLAND

2019

ABSTRACT

Phosphate is an essential nutrient for plant life in water that when in abundance can have a series of adverse effects on an ecosystem. As such it is of great interest to scientists and environmentalists alike to detect phosphate in the environment. The current state of detection technology leaves much to be desired however as devices are insensitive, ineffective, and sometimes expensive. This study presents a series of methods, systems, and devices that were developed in the pursuit of advancing the state of detection of orthophosphate in water. A lab-on-chip device was created utilizing the molybdenum blue reaction with a novel configuration that allows sensitive measurements to be taken without exposing the user to dangerous chemicals. The device houses the molybdenum complex in a bubble while the acid is spotted in a separate paper-based section. Button activation joins the two reagents and a colorimetric reaction is induced upon sample addition. The architecture was able to achieve a limit of detection in the parts per billion (ppb) range, a superior performance to currently available commercial devices. An accompanying light box was created so that colorimetric measurements could be taken in the field using a stable lighting environment. In addition, an iOS app was developed that could instantly and reliably quantify measurement concentrations based on obtained RGB values and programmed calibration curves. The app features a data architecture that connects to an online data center offering a highly scalable worldwide system for tracking and analyzing field measurements. An inexpensive infrared detection system was also developed with an infrared camera and Raspberry Pi to take advantage of the peak absorbance of the molybdenum blue reaction. The system was able to increase the limit of detection on a popular commercial device by a factor greater than 10, greatly improving its capacity and showing potential for commercial adaptation.

ACKNOWLEDGMENTS

This project would not be possible without the assistance and guidance of several key people.

I would first like to thank professors Mohammad Faghri and Constantine Anagnostopoulos for allowing me to work under them and providing me with constant support and guidance throughout my Masters at the Microfluidics Laboratory. Needless to say that none of this would have been possible without their help.

A special thanks to Stephen Powers whose helpful recommendations in the field of chemistry and biology helped the direction of not only this project but several others in our lab.

I would also like to express my gratitude to my colleagues Amer Charbaji, Wayne Smith, and Nicholas Lemos. Me and Amer worked together on almost every academic endeavor in the last two years and its difficult to imagine completing this work nevertheless completing my degree without his aid. His constant support which came in the form of suggestions, guidance, and sometimes afternoon snacks were invaluable to me. Wayne has been an incredible source of ideas. His creativity and inventiveness are truly astonishing. Our long talks and late night food journeys kept me sane as we worked late at night in the lab. Nick provided me with my initial training in microfluidics when I started. His prototyping experience was of great help throughout this work in addition to his positive personality that always brightened up the lab.

Much thanks to Joanie Racicot who is as every part responsible for the device created in this work as I am. She performed countless tests in the pursuit of optimizing the chemistry and endured the hell that is the molybdenum blue reaction. Legend says that parts of her lab are still stained blue to this day.

I owe a great deal of gratitude to my intern Jake Gorelikov who performed serial dilutions, chemical reactions, and a considerable amount of other tasks that I did not want to do. His lab competence allowed me to work and obtain results at a much faster rate than I would have been able to alone. For that I will always be grateful.

Lastly, I would like to thank my family who supported me throughout my entire graduate school journey. Their constant love and positivity pushed me to pursue this degree and gave me the strength to complete this project.

TABLE OF CONTENTS

Page

Page

LIST OF FIGURES

Figure **Page**

Figure **Page**

Figure **Page**

Figure **Page**

LIST OF TABLES

CHAPTER 1

Introduction

This chapter provides a brief introduction to the reader on the current state of phosphate detection methods. Background knowledge on phosphate and its importance in water quality will be thoroughly examined. Commercial devices will be discussed along with currently attainable sensitivity levels. The suitability of lab-on-paper and lab-on-chip technologies for application in phosphate detection will also be explored. Lastly, the justification and objective of this thesis will be stated.

1.1 Phosphorus and its Impact on Water Quality

Phosphorus and nitrogen are essential nutrients for plant life in water. An excess of these two chemicals however can cause a series of adverse effects on water quality and as such both nutrients are highly researched and studied [1]. Nutrient pollution in water is a major environmental concern that affects a large number of bodies of water. An overload of these nutrients is the main cause of eutrophication in water. Eutrophication of water, shown in Figure 1, is the process of an excess of nutrient enrichment that has serious ecological impacts. The main ecological threat that accompanies eutrophication is the increased growth of macrophytes, algae, and cyanobacteria. The growth of these aquatic plant organisms is named 'algal blooms'. These algal blooms can be extremely detrimental to water quality.

Algal blooms can create toxic chemicals which are harmful to both humans and aquatic life. These chemicals can make their way into seafood and drinking water, which when consumed may result in deadly long-term consequences. Consumption of neurotoxins found in these blooms can even lead to Alzheimer's and Amyotrophic Lateral Sclerosis (ALS) [2], [3]. In addition, the overgrowth of algae in the water

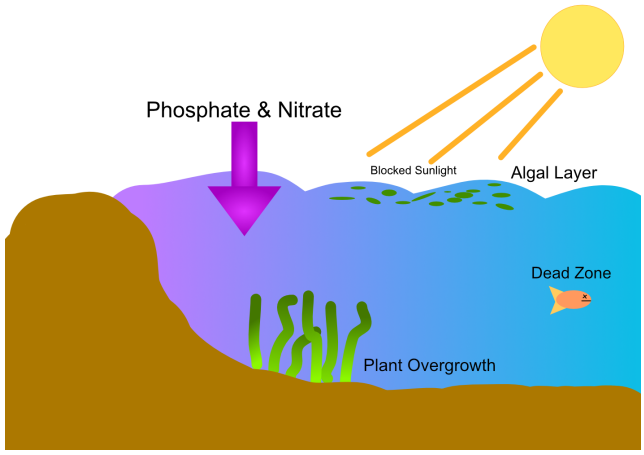

Figure 1. Eutrophication

consumes oxygen and blocks sunlight entering the body of water. When the algae die, this leaves the water in a hypoxic condition where the water is deprived of dissolved oxygen. It is impossible for aquatic life to survive in such an environment and as such dead zones are created in the water [1]. Dead zones can occur in oceans, lakes, and even rivers. One of the biggest dead zones in the world is found in the Gulf of Mexico in the United States. The Mississippi River is the drainage area for 41 percent of the United States where nutrients are continuously dumped in the river as it makes it's way to the Gulf of Mexico [4]. It is estimated that this dead zone shown in Figure 2 is 8,776 square miles in area, about the size of New Jersey [5].

1.2 Economic Impact

The ecological impacts of nutrient enrichment are also accompanied by economic consequences. The water pollution caused by nutrient enriched waters and subsequent algal blooms pose significant economic hazards to several industries. Increase in water treatment costs is a major concern for water companies. Water quality is deteriorated by algal blooms which induces higher treatment costs [7]. The water quality can deteriorate so much at times that it becomes unfit for drink-

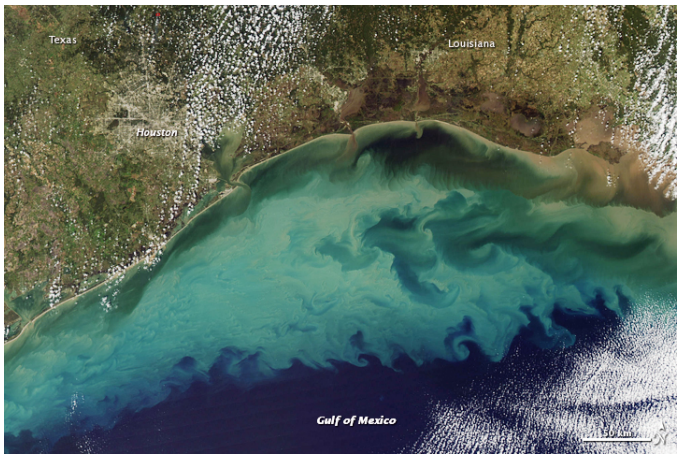

Figure 2. Dead Zone in the Gulf of Mexico [6]

ing and can result in a water ban for customers as was the case in 2014 in the city of Toledo, Ohio, U.S [8]. In addition to treatment costs there are also monitoring and testing costs associated with keeping track of these blooms. These costs can become quite significant.

Algal blooms can also negatively impact the tourism industry [9]. Popular tourist destinations with bodies of water can be heavily affected by algal blooms. Tourists tend to avoid areas where algal blooms are present and as such leads to decreased economic activities in those locales. Property and real estate are also victims of bad water quality. Home prices depreciate significantly as a consequence of nearby lakes affected by blooms [10]. Property owners tend avoid such areas due to the bad smell that emanates from such lakes and the potential health hazards that accompany them.

The fishing industry is affected in several ways by algal blooms [9]. Firstly, the creation of dead zones decreases the availability of fish in the water. Second, the fish caught might be contaminated and therefore harmful for humans to consume. Shellfish poisoning is a common occurrence for bodies of water heavily affected by algal blooms. The consumer then also tends to avoid buying fish which further adds

to economic obstacles. In 2011 for example, it was estimated that marine borne diseases had an impact of 900 million dollars in losses for the fishing industry in the U.S. [11].

1.3 Sources of Contamination

There are various sources of nutrient contamination present in the world. One of the most common sources of nutrient pollution comes from agriculture [12], [13]. Animal manure and fertilizers used on crops contain high amounts of nitrogen and phosphate that can make their way into bodies of water through runoff. These runoffs of nutrients may even contain other harmful compounds such as ammonia and nitrogen oxide which may pose further environmental issues.

Wastewater is another major contributor to nutrient pollution [14]. Nitrogen and phosphorus are present in wastewater through the result of human waste, food, and other common household items. The water is sent from homes to wastewater treatment facilities where the water is treated in order to remove nutrients and other chemicals. The water is then deposited into local bodies of water carrying varying amounts of nitrogen and phosphate.The effectiveness and efficiency of these treatment facilities vary greatly and some are not able to treat the water as well as others. Improving wastewater treatment systems can have a significant impact on reducing nutrient pollution as is the case in the Netherlands where advanced treatment systems can remove up to 78 percent of nitrogen compared to only 5 percent by conventional systems in the U.S. [15].

Septic systems introduce nutrients into the environment in a similar way to wastewater treatment facilities. Many households across the globe still commonly utilize septic systems for sewage disposal. The nitrogen and phosphate present in the waste of these systems can make their way towards groundwater and surface water when improperly maintained. Septic systems can also fail due to a variety of

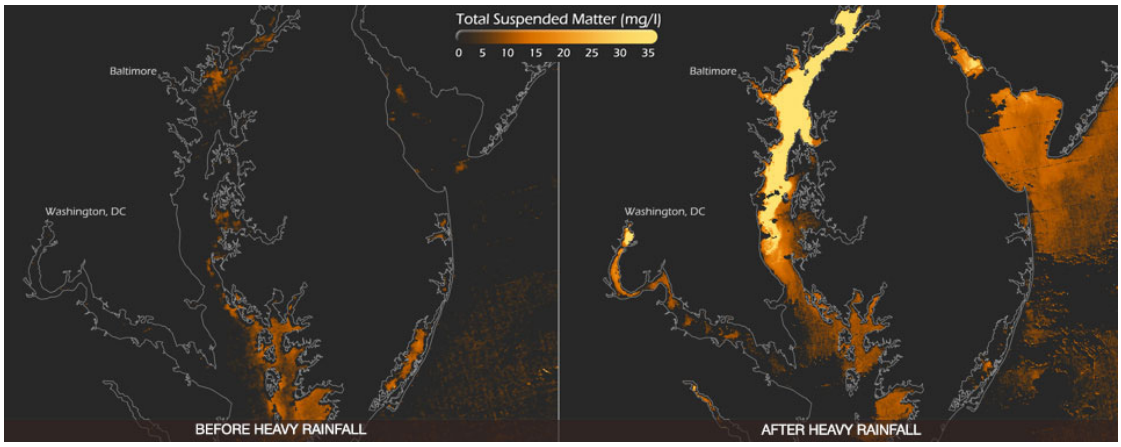

Figure 3. Stormwater Pollution [17]

reasons that range from structural failure to inadequate designs. These failed systems can then become serious threats to nearby bodies of water. Considering that nearly one fifth of households in the U.S. use septic systems, they are undeniably a potential major source of water pollution [16].

Stormwater dispenses large amounts of pollutants into waterways including phosphorus and nitrogen [14]. Rainfall water makes its way throughout cities picking up and carrying nutrients and compounds from various sources along the way. This stormwater then enters storm drains or local bodies of water without any form of filtering or treatment. The runoff after days of heavy storm can add immense quantities of pollutants into groundwater and surface water. The figure below, Fig. 3, shows how effective stormwater is at introducing matter into Chesapeake Bay after an episode of heavy rainfall [17].

While this thesis concerns itself with the detection of phosphate, it is important to mention another major source of contamination that contributes to nutrient pollution in water. Fossil fuels emit nitrogen oxide into the atmosphere when burned. These fossil fuels are burned in automobiles, airplanes, power plants, industrial facilities, and in many other forms of human activity. The surplus of nitrogen in the atmosphere will make its way back onto land where it will eventually

be deposited into nearby water through different forms of runoff. The pollution resulting from the burning of fossil fuels is a major global issue that has many hazardous implications associated with it.

1.4 Phosphates

Phosphorus like nitrogen is one of the main nutrients responsible for nutrient pollution in water. Phosphorus however, is not found in its elemental form because it is far too reactive by itself [18]. In nature, phosphorus is present in the form of phosphates. The terms phosphorus and phosphate are sometimes used interchangeably, but phosphate is the plant nutrient that is found in nature. The detection and quantification efforts are therefore geared towards phosphate and not elemental phosphorus.

There are many different kinds of phosphates [19]. They are all classified in three different forms: orthophosphates, condensed phosphates, and organic phosphates. Orthophosphates are reactive phosphates which occur naturally and are found in agricultural products such as fertilizers. Condensed (inorganic) phosphates are compounds which contain metals or salts. These compounds are used in some industrial applications. Organic phosphates are phosphates that are typically formed through biological processes. These phosphates are found everywhere in nature through animal or human waste. Both organic and inorganic phosphate can be dissolved or suspended in water.

Detection methods are concerned with detecting orthophosphate in water as it is found in fertilizers, wastewater and is the only form that autotrophs can assimilate [20]. Orthophosphates provide a very good measure of available phosphorus present in water. The orthophosphate ion is also quite simple as it only contains one phosphorus atom and four oxygen atoms. The orthophosphate ion is PO_4^{3-} and is shown in Fig 4.

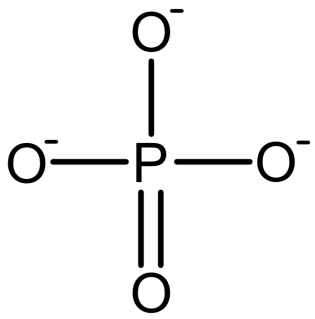

Figure 4. Orthophosphate Ion

1.5 LOD Sensitivity Needs

Phosphate concentrations need not be very high in bodies of water to cause significant changes to the ecosystem. Mackenthun [21] suggested that phosphorus levels should not exceed 50 $\mu g/l$ where waters enter a lake, reservoir, or other standing water body in order to prevent biological nuisances. Unfortunately this means that detection methods must be very sensitive in order to detect these minuscule concentrations of phosphate. Most of the world's oceans contain levels of phosphate that are in fact too low for most traditional detection methods. The main reason behind this is that phosphate is mainly detected at the surface level of water and the concentration of phosphate increases significantly with depth as shown in Figure 5 [22]. This adds a major complication to current detection techniques because it signifies that very sensitive methods are needed when testing for phosphate in ocean waters.

Phosphate detection methods must then have a particular limit of detection (LOD) target to achieve. It is clear that detection limits in the ppm or milligram per liter (mg/L) are far too crude for current sensitivity needs. A proper device will have to achieve low parts per billion (ppb) or micrograms per liter (μ/g) detection levels in order to successfully be able to measure phosphate in most bodies of water. This thesis concerns itself with a general device to be used in any body of water in the detection of phosphate concentrations. In order to achieve this, a low

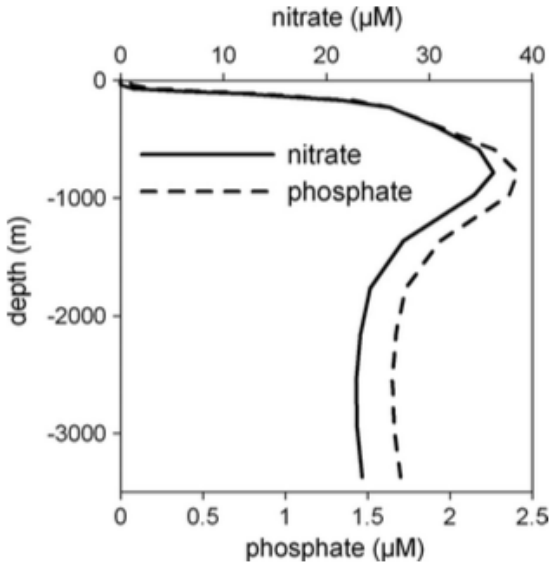

Figure 5. Phosphate Concentration vs. Water Depth [22]

ppb LOD will be the target.

1.6 Detection Methods

There are several detection methods currently used in the detection of phosphate in water. These methods range from colorimetric chemical reactions to electrochemical and fluorescence methods [23], [24], [25]. Colorimetric methods are ideal for paper based applications and as such will be the focus in terms of chemistry. The most commonly used method currently is the molybdenum blue method by Murphy and Riley [23]. The molybdenum blue method has been the standard for over 50 years and most detection methods are based off of this method. This method is a colorimetric method where the solution made up of several reagents becomes blue once in contact with phosphate as shown in Figure 6 [26]. The more intense the blue is, the higher the concentration of phosphate present in the water. Because this method is so commonplace and fairly effective in the field, it will be the starting point for the device built in this thesis.

There are two other common colorimetric methods the can be used in the

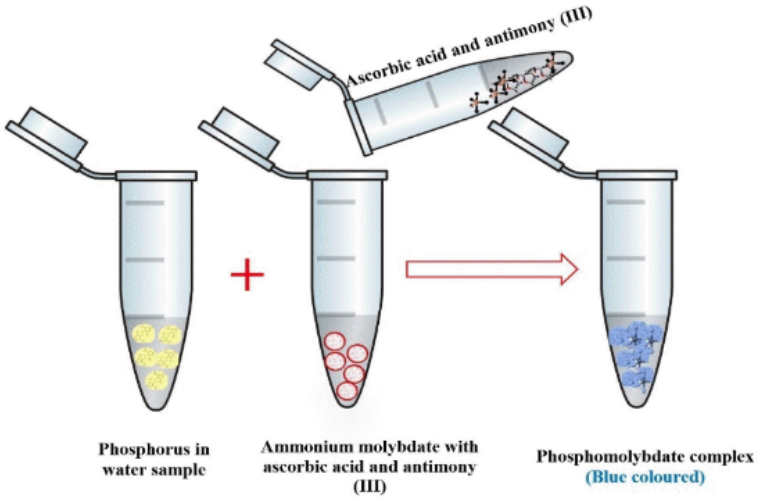

Figure 6. The Molybdenum Blue Method [26]

field. These methods are the molybdovanadate method [27] or yellow method and the malachite green method [28]. These methods are similar to the molybdenum blue method in the sense that once the solution comes in contact with phosphate, they will turn into a color that intensifies with concentration. This color is yellow in the case of the molybdovanadate method and green in the case of the malachite green method. These two methods will be researched along with the molybdenum blue method in order to determine the optimal colorimetric reaction to achieve high sensitivity with lab on paper/lab on chip technology.

Other methods will also be considered for application with lab on chip technology. Electrochemical methods will be studied due to their high potential for low sensitivity [24], as will fluorescence methods [25]. The main objective of these methods is to have very high sensitivity while also being suitable for use in the field in a package that could be manufactured and sold at a low-cost. The various different detection methods and their suitably for the device objectives of this thesis will be discussed further and in detail in the Literature Review section.

1.7 Commercial Devices

The various commercial devices currently available on the market range from low-cost devices that have low sensitivity to higher-priced complex devices with better sensitivity. Commercially available devices also vary from easy to use to complex operation that is not suitable in the field. The most common and by far the easiest to use type is the dip strip. One must simply 'dip' the strip into the water in order to cause a reaction. A dip strip device usually employs colorimetric methods that the user can then compare to a color chart in order to determine levels of phosphate present in the water. These devices are usually not very sensitive and unsuitable for most bodies of water [29]. Some dip strips add sensitivity by requiring that the user handles certain reagents [30]. The handling of reagents by users is to be avoided however in order to remove human error and reduce risk of injury. The device built in this thesis will be autonomous in order to minimize both human error and health hazards associated with the handling of potentially dangerous reagents.

There are commercially available fluorescence reagents that change fluorescence intensity in contact with phosphate [31]. These reagents are very sensitive and effective but demand significant storage conditions that are simply impractical and unsuitable for use in the field. Fluorescence methods do however offer much promise and will be considered as a potential solution to sensitivity needs if field use applicability could be achieved.

The LOD achieved by the majority of these commercial devices are in the ppm range. This is highly insufficient for many bodies of water and as such serious improvement is needed. While there are phosphate assay kits in the market that can achieve ppb levels of LOD, they require some experience and input from the user performing the tests. The goal is to achieve high sensitivity while also focusing

on the user. The end-user might be a citizen scientist looking to quickly and easily test for phosphate in their local lake. For such a user, keeping the device autonomous and as simple as possible is essential.

1.8 Lab-on-Paper and Lab-on-Chip Technology

Paper-based technology has continuously increased in popularity over the last couple of years. Devices utilizing paper-based systems have been dubbed the name lab-on-paper. This name represents the idea that the device can replace a full sized laboratory when performing a certain task. This technology has grown significantly in demand due to the low cost and convenience of paper. The simplicity of such devices make them ideal for testing in the field by anyone.

As technology and innovation advances in this field, so will too the capabilities of the devices. Serious research has been undertaken in the past couple of years in the manipulation of fluids in these paper-based devices. There have been many inventions which have made it very feasible to manipulate fluids on such devices. These inventions range from chemically actuated valves [32] to temperature based reagent delivery systems [33]. These innovations have made automation in paper-based devices possible. Automation provides the ultimate convenience for the user in that he or she does not need to be involved in the mixing, timing, and delivery of potentially harmful reagents. This automation can not only provide convenience for the user but also lead to a reduction in human error.

Lab-on-paper devices have actually made their way into the market and are quite common. The simplest and most well known variation is the lateral flow immunoassay device (LFIA) [34]. Most pregnancy tests are in the form of a LFIA. With increasing technology advances more intricate testing procedures will eventually be possible on lab-on-paper device. It is clear that this technology has serious market potential as shown in the widespread use and success of pregnancy tests.

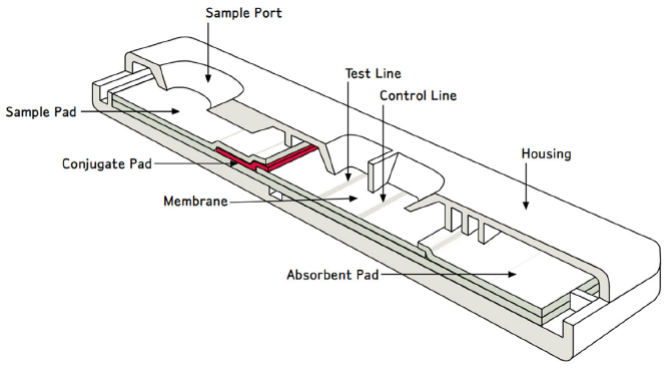

Figure 7. Lateral Flow Device [35]

Figure 7 [35] below shows the architecture of a typical LFA.

Lab-on-Chip (LOC) technology is another field with massive potential. Unlike lab-on-paper devices, lab-on-chip devices perform tests in a fluidic circuit composed of solid materials and may also house various other technologies in one chip [36]. These devices can be built to be low-cost like paper-based devices but come with the caveat of increased manufacturability requirements. Special equipment is usually required in order to build devices with increasingly complex testing demands. The advantage of lab-on-chip devices is improved control achieved by removing paper which has variable parameters such as porosity and pore size.

There are devices that incorporate both technologies in one device. Lab-on-chip devices may utilize solid channels for example but then perform timing and delay operations with paper-based valves. This configuration can potentially be optimal for some applications. Both technologies are considered in this thesis in order to find the best compromise in ease-of-use, manufacturability, and effectiveness. A lab-on-chip prototype device for testing diseases is shown in Figure 8 [37] below.

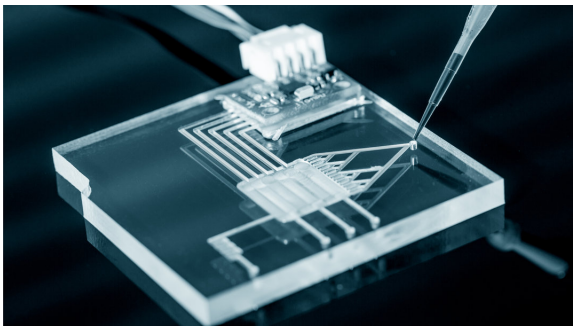

Figure 8. Lab-on-Chip Device [37]

1.9 Justification

Microfluidics and lab-on-paper devices are rapidly growing in popularity due to their simplicity, price, and portability. These devices have the potential to be used in a variety of applications where their many advantages make them ideal systems for field work. Phosphate detection is one of these applications where lab-on-paper devices show a lot of promise. Phosphate is an essential nutrient for the growth of plants and animals in the ocean that has serious adverse effects on water when found in excess. As a result, there is a demand to easily and reliably monitor phosphate levels in water.

Successful systems have been made using filter paper in order to detect phosphate, however there is still much to be desired in terms of robustness, reliability, and applicability for field use [38], [39]. Limit of detection is also a very important aspect for detecting phosphate because in most ocean waters, the level of phosphate at the surface is quite small [22] and a sensitive device is absolutely necessary in order to detect these levels of phosphate. The current technology on phosphate detection lacks not only limit of detection levels but also robustness for field use.

There is a market and a demand for a device that is low-cost, suitable for field use, and most importantly sensitive enough to detect phosphate levels in all different stages of nutrient contamination in any body of water. The objective

is to create this device utilizing a combination of lab-on-paper and lab-on-chip technologies. Manufacturability must also be accounted for as the end-goal is production and sale in the open market. This project is the realization of a multi-disciplinary effort in conjunction with the Chemistry Department at the University of Rhode Island.

1.10 Outline

The structure of the thesis is as following:

Chapter 1: Introduction - This chapter gives the reader an overview of the various topics covered in the thesis. It serves as a primer for background knowledge before venturing into the work done. The justification and objective of the thesis is also covered in this introduction.

Chapter 2: Literature Review - The main factors affecting the success of the device are thoroughly studied and examined in this chapter. Various detection methods, LOP and LOC technologies, and commercial devices are all extensively investigated. Many of the topics covered in Chapter 1 of the thesis are also given further reflection here.

Chapter 3: Methodology - The various experiments and processes used in device creation are discussed in detail in this chapter.

Chapter 4: Findings - The results for experiments and studies performed in Chapter 3 will be examined in this chapter. All the findings for important parameters that affect the success of the device are discussed here.

Chapter 5: Conclusion - All findings are summarized in this chapter and conclusions are given on the results of the work done. This chapter also proposes potential areas of future work on the device.

CHAPTER 2

Literature Review

This section is a literature review of the various parameters and features that affect the overall success of a device. Some of the topics covered in Chapter 1 will be discussed here with greater detail. Currently available detection methods, commercial devices, and both lab-on-chip and lab-on-paper technologies will all be thoroughly covered.

2.1 Colorimetric Detection Methods

Colorimetric detection methods are an ideal solution to the detection of chemical concentrations in water by a citizen scientist. Colorimetric methods are fairly simple, once phosphate comes in contact with certain reagents, a colorimetric response is induced and the concentration of phosphate is directly related to the intensity of the color. This type of system is perfectly suited to the field where the color produced can be either compared to a color chart or measured with a simple RGB application. These methods also have the advantage of working very well with paper-based technology where they have been employed in the form of pregnancy tests, pH readings, and many other systems. In addition, colorimetric methods can be inexpensively integrated into a device leading to an overall economically priced final product.

2.1.1 The Molybdenum Blue Method

The Molybdenum Blue Method has been the gold standard in the colorimetric detection of phosphate for over 50 years. It is a fairly simple method that only requires the use of a couple reagents. It was originally devised by Deniges in 1920 [40]. The method has been modified and improved on for decades since its

creation. Because of its wide-spread use and reasonably sensitive detection limits, the Molybdenum Blue Method will be the baseline chemistry for the device in this thesis.

The original method relies on the formation and reduction of phosphomolybdic acid brought by an acidic molybdate solution containing ascorbic acid. This process however would require a long period of time to form a colorimetric reaction. Murphy and Riley added a potassium antimonyl tartrate solution which significantly sped up the process and resulted in a rapid formation of an intense blue color [23]. The improvement by Murphy and Riley was so significant that their method is now considered the standard when referring to the Molybdenum Blue Method. Only one mixed reagent was used in their reaction and consisted of 125 ml of 5 N sulfuric acid, 37.5 ml of ammonium molybdate, 75 ml of ascorbic acid, and 12.5 ml of potassium antimonyl tartrate solution. This reagent would have to be prepared as required however because it does not keep for more than 24 hours.

There have been numerous variations based around the molybdenum blue method in the many years since its original inception and each have varying reagent concentrations, pH levels, reductants, and so forth. Drummond and Maher examined the various parameters affecting the reaction in order to deduce the optimum conditions for the analysis up to phosphate concentrations of 800 $\mu g/l$ [41]. They found that by selecting a $[H^+]$ / $[MoO_4^{2-}]$ ratio of 70 and a pH 0.57-0.88 in the final solution together with an excess of antimony (0.06 mM) and ascorbic acid (0.009 M), resulted in full color development within a minute. They also found however that using these reagent concentrations with phosphate concentrations above 800 $\mu g/l$ resulted in incomplete color development. A compromise will have to be made when building a device therefore, in order to be able to measure phosphate in both

low concentrations and highly eutrophic systems.

The Molybdenum Blue Method is not without its faults. The method is susceptible to interference from a couple different sources. Both Silicate and Arsenate can potentially interfere with the reaction leading to erroneous results. Drummond and Maher have found that Silicate concentrations of up to 10,000 μg Si/l at room temperature can be found without causing significant phosphate over-estimation [41]. They found however that Silicate at a concentration of 100 mg Si/l caused about a 25 percent over-estimation of phosphate levels. Raising the temperature of the reaction should be avoided therefore as that will raise the rate of silicate reaction with the molybdate reagent [42]. Drummond and Maher also found that arsenate will not cause an error as long as it is present at levels of less than 10 μg As/l. Minimizing interference from these two elements will have to be taken into account when optimizing the chemistry in order to avoid any erroneous readings.

The limit of detection achieved with this method can be fairly low and well suited for measuring phosphate in the vast majority of bodies of water. The target limit of detection for the device in this thesis is in the low ppb ($\mu g/l$) range. The molybdenum blue method can achieve this target but the problem is integrating the reaction into an easy-to-use package with decent shelf life. Phosphate concentrations are normally measured spectrophotometrically in order to measure the intensity of the blue color. A calibration curve can be made from measuring the blue intensity across a wide range of concentrations. A limit of detection is then found by establishing the lowest concentration of phosphate which still offers a discernible colorimetric response that is both repeatable and can fit the calibration curve.

Limits of detection below 1nM have been achieved by measuring phosphate concentrations spectrophotometrically with the Molybdenum Blue Method [22].

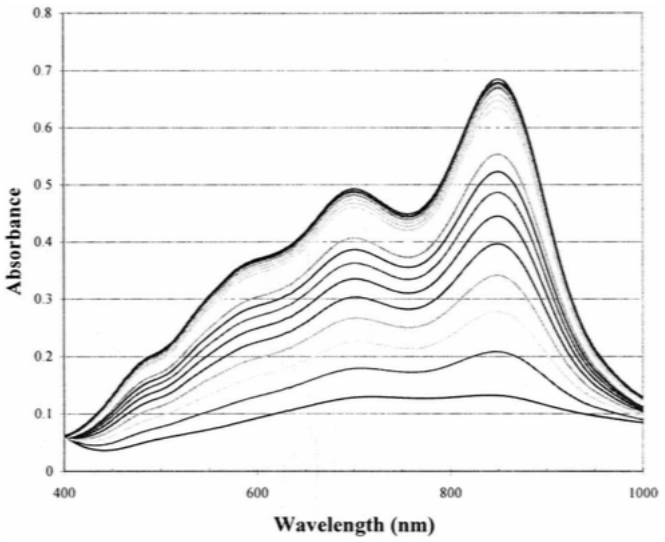

Figure 9. Absorbance Spectrum of the Phosphomolybdenum Blue Complex [43]

While these are great results, He and Honeycutt have shown that the peak absorbance of the method is actually in the infrared range [43]. They measured a peak absorbance at around 850 nm as shown in Figure 9. This signifies that measuring the reaction in the infrared can increase the sensitivity of a device even further. He and Honeycutt found that the linearity of the absorbance at 850 nm made it possible to increase the sensitivity of phosphate determination by 45 percent. This increased sensitivity also adds flexibility to reagent concentrations since any reduction in sensitivity caused by an improvement to reagent stability or device function can be offset by the higher sensitivity provided by infrared detection. An inexpensive infrared detector can then ultimately be built in order to complement a device and provide sensitive phosphate determination. The user will then have the option of measuring spectrophotometrically when high sensitivity is unnecessary and with the infrared detector when precise measurements of low concentrations need to take place.

The reaction will have to be integrated into a device that is suited for the field. The method has been successfully integrated onto filter paper in the past.

Jayawardane et al. have implemented the method into a simple paper-based device [38]. The molybdate reagent and ascorbic acid were dried onto filter paper and separated by an interleaving teflon sheet. Activation simply required removing the teflon sheet and depositing sample onto the filter paper. They achieved very good results with a working range of 0.2 - 10 mg/l Phosphate. The main issues they faced were storage conditions and shelf life which ranged from a couple days in room temperature to over 112 days at temperatures below -20 °C. Improvements can be made in both robustness and storage to provide a product that is suited for commercial use. A device architecture must be developed using both lab-on-paper and lab-on-chip technologies to achieve this goal.

2.1.2 The Malachite Green Method

The Malachite Green Method works in a similar manner to the Molybdenum Blue Method. It produces a colorimetric reaction whose intensity is directly related to the concentration of phosphate present. Unlike the Molybdenum Blue Method however, the colorimetric response induced by the Malachite Green Method is green instead of blue. This method was first introduced in 1966 by Itaya and Ui [28]. The method works on the basis that the malachite green dye at a lower pH forms a complex with phosphomolybdate with a marked shift of the absorption maximum. The reaction involved mixing a solution of the malachite green dye with one third the volume of acidified ammonium molybdate (4.2 percent). The mixture was filtered after 20 minutes and then sample was added to produce a colorimetric response. The response was then measured with a spectrophotometer to deduce the concentration of phosphate present in the sample.

This method has a couple advantages over the Molybdenum Blue Method. It has a very high sensitivity, Linge and Oldham reported four times as sensitivity as the traditional Molybdenum Blue Method with ascorbic acid [44]. It is also

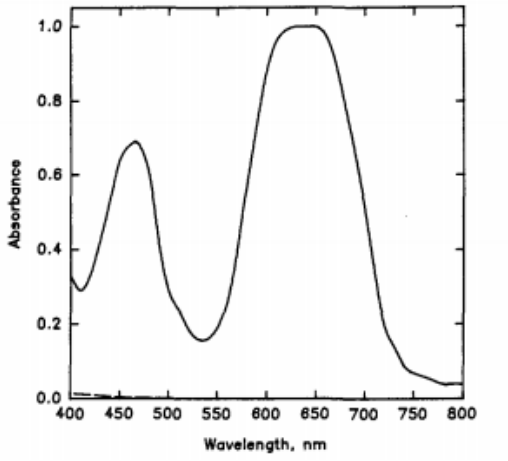

Figure 10. Absorbance Spectrum of the Malachite Green Method [45]

significantly less sensitive to changes in reaction time, temperature, and reagent addition. The absorption spectrum of the reaction also happens to be around 620 - 650 nm as shown on Figure 10 [45]. This peak absorption signifies that the reaction could be measured entirely by spectrophotometric methods and an infrared detector is not needed to increase sensitivity unlike the molybdenum blue method.

The main interferents in the Malachite Green Method are the same as those in the Molybdenum Blue Method as both methods are based on the production of a molybdophosphoric acid. Both silicate and Arsenate pose potential interference threats during the reaction [44] [46]. This method has not been previously implemented into Lab-on-Paper or Lab-on-Chip technology for the determination of phosphate concentrations in water. This provides an interesting research opportunity to test the suitability and feasibility of this method with LOP and LOC technologies. Employing malachite green could prove to be very beneficial in the pursuit of sensitivity if it is found to be compatible with paper-based systems.

2.1.3 The Molybdovanadate Method

The Molybdovanadate Method is another colorimetric method where the reaction produces a colorimetric response. This method produces a yellow color that intensifies with phosphate concentration. It was originally conceived by Misson in 1908 [47] and there have been countless variations since. Unlike both the Malachite Green and Molybdenum Blue Methods, the Molybdovanadate Method is based on the production of a molybdovanadophosphoric acid complex. This results in a number of interesting outcomes because the chemistry is in essence different than the other methods.

While this method was originally measured spectrophotometrically, modifications by Michelson [48] resulted in the ability to measure the reaction in its absorption maximum. This maximum is in the ultraviolet range however as shown on Figure 11 where spectrum 1 is molybdovanadophosphoric acid compared with water, spectrum 2 is a blank compared with water, and spectrum 3 is molybdovanadophosphoric acid compared with a blank. Similar to the Molybdenum Blue method having an absorption maximum in the infrared, this results in an interesting opportunity to utilize some form of detection device that can measure in the ultraviolet. This would of course increase sensitivity but would not be necessary for measurements where high sensitivity is unnecessary. The user would then have the option to either measure spectrophotometrically with an application for large concentrations of phosphate (eutrophic waters) or measure in the ultraviolet range when high sensitivity is required.

Bartlett and Lewis [49] modified Michelsen's [48] method even further by diluting the complex solution. This resulted in a more detailed ultraviolet spectrum with great sensitivity (low ppb when measuring for phosphate esters). The method has like Malachite Green, never been implemented onto a Lab-on-Paper

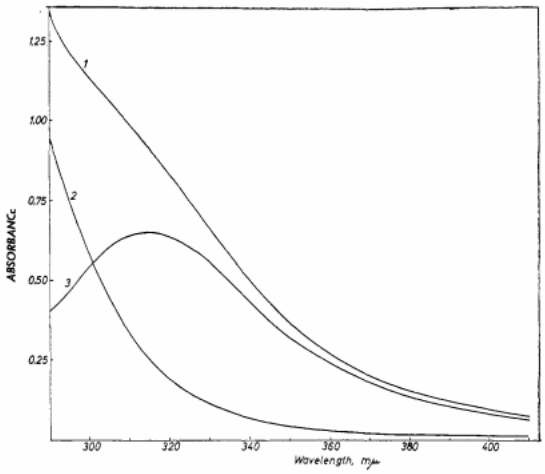

Figure 11. Absorbance Spectrum of the Molybdovanadate Method [48]

or Lab-on-Chip device. This provides an opportunity to attempt something novel by integrating the method with a paper-based system. The obstacle will be the suitability of the method with paper and if a ultraviolet detection device could be easily and economically constructed.

2.2 Electrochemical Detection Methods

Various electrochemical methods have been devised in order to detect orthophosphate in water. These methods vary greatly in principle as there are many possibilities. Electrochemical methods can increase sensitivity and lower the limit of detection, but come at the cost of adding complexity to the device architecture.

Jonca et al. [50] [51] took steps to develop an autonomous sensor for the electrochemical detection of phosphate in seawater. Their method involved the anodic oxidation of molybdenum, which forms molybdate ions and protons in order to create the molybdophosphate complex without the addition of liquid reagents. They then measured the molybdophosphate complex with amperometry and achieved a very low detection limit of 0.12 μM. Jonca et al. faced the same issues with silicate interference as the colorimetric methods but were able to find different approaches

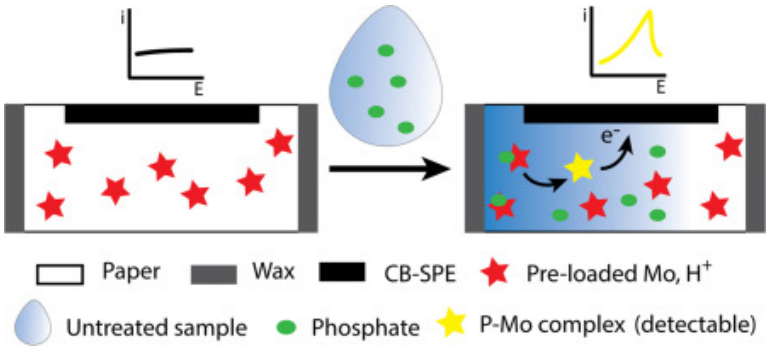

Figure 12. Reagentless Electrochemical Device [53]

to combat this problem. One of the approaches was first devised by Zhang et al. [52] and is also appropriate for the reduction of silicate interference in colorimetric detection methods. Zhang et al. learned that silicate interference can be avoided when working with a protons/molybdates ratio close to 70 at a pH level of 1.0.

Cinti et al. [53] invented a novel approach to phosphate detection with a device that is reagentless. Their method consisted of wax patterning on paper similar to lab on paper devices. The paper was then chemically modified with molybdate ions, potassium chloride, and sulfuric acid. Finally a three electrode configuration was screen printed and the device architecture was formed. Cyclic voltammetry was used to quantify the levels of phosphate present in the sample. This novel device achieved high sensitivity detecting phosphate at levels as low as 4 μM. The device also came with the advantage of long storage stability, having not lost signal after being stored for 30 days at room temperature. A graphical representation of their device is shown in Figure 12. Clearly, electrochemical methods show a lot of potential and promise and as such are great candidates for use in a commercial device.

2.3 Fluorescence Detection Methods

Fluorescence detection methods show great promise when sensitivity is concerned. They are also not too far different from colorimetric methods, in the sense

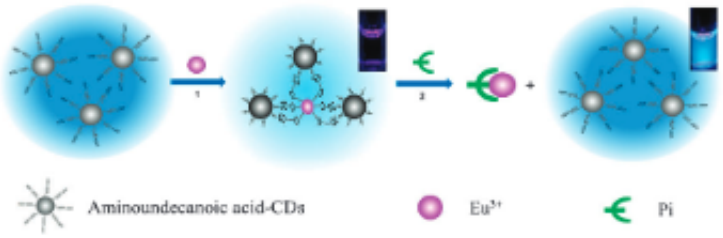

Figure 13. Off-on Fluorescence Probe of Carbon Dots Adjusted by Eu^{3+} [54]

that a response is induced that varies with intensity and can be measured with a detector. There are several different types of fluorescence sensors. Some sensors may exhibit an increase in fluorescence intensity when exposed to higher concentrations of the substance in question while others decrease [25]. This is an important distinction to make when utilizing such methods as the final device operation will highly depend on the type of sensor used.

Zhao et al. [54] developed a highly selective detection method using an off-on fluorescence probe of europium-adjusted carbon dots. Their method takes advantage of the affinity of europium to oxygen-donor atoms. This affinity is stronger when the oxygen-donor atoms originate from phosphate rather than from carboxylate groups. Their off-on fluorescence device then utilizes this competition between phosphate and the carboxylate modified carbon dots in order to quantify phosphate levels using europium ions. A schematic of the design is shown below in Figure 13. Zhao et al. achieved tremendous selectivity using this method. Monovalent and divalent anions along with substances including carboxylic acids were tested on the system and results showed that phosphate had an enhanced factor of 24-fold when compared with these other anions. The fluorescence probe was used in artificial wetlands and demonstrated comparable sensitivity to the molybdenum blue method. This method is very impressive as it is both sensitive and quite cost-effective.

Lee et al. [25] utilized an acridine-Zn complex to detect both inorganic phosphate and pyrophosphate in aqueous solutions. This chemosensor is quite unique in that it displays different signal responses for pyrophosphate and phosphate in water. A CHEF (chelation enhanced fluorescence) effect is induced with phosphate while a CHEQ (chelation enhanced fluorescence quenching) effect is induced with pyrophosphate. Essentially, phosphate increases the fluorescence intensity while pyrophosphate does the opposite. This method achieved great sensitivity where pyrophosphate could even be detected at nanomolar concentrations in water. While this thesis concerns itself only with the detection of inorganic phosphate in water, the results of Lee et al. are quite encouraging and warrant a closer look into fluorescence methods and the integration of such sensors in a Lab-on-Chip or Lab-on-Paper Device.

2.4 Lab-on-Chip and Lab-on-Paper Technology

Lab-on-Chip and Lab-on-Paper technologies have continued to increase in popularity in the past couple of years due to their very promising future. These technologies have a wide range of applications that can bring the scientific lab to the palm of a user's hands. Devices utilizing these technologies simplify scientific processes and have the advantage of being perfectly suited for field use. The convenience of portability is also accompanied by inexpensive costs and the possibility of autonomy. This section will take a look into the various developments that have been made and are currently taking place in both lab-on-chip and lab-on-paper technologies.

2.4.1 Reagent Storage

Reagent storage and placement are key factors affecting the operation of lab-on-chip and lab-on-paper devices. Reagents need to be integrated into the device

Figure 14. Glass Ampules for Reagent Storage [55]

prior to use and this can be achieved in many different ways. Sometimes a form of container is used in lab-on-chip devices that is activated upon device operation. Lab-on-paper devices on the other hand might simply dry the reagent in certain spots of the paper-based device. This problem is essential not only in contributing to the overall device operation and functionality but also to the safety of the user. The reagents used in these devices are sometimes quite harmful and proper design must be in place in order to prevent contact between chemicals and the user. Several solutions that have been devised for this obstacle are detailed below.

Hoffman et al. [55] developed a solution to this problem through the use of glass ampoules for reagent storage. They devised an efficient manner of fusing liquid reagents into glass ampules that are then sealed into a centrifugally operated cartridge. The reagents could then be easily released through the cartridge's flexible lid. The system is shown in Figure 14. This solution would of course add some complexity to the final fabrication process but the method exhibited quite impressive results. 98.7 μL of the original 100 μL was released upon centrifugation and no liquid loss was observed for both ethanol and water in a 300 day period at room temperature. This approach developed by Hoffman et al. can potentially be a robust solution for storing the reagents needed to detect phosphate colorimetrically.

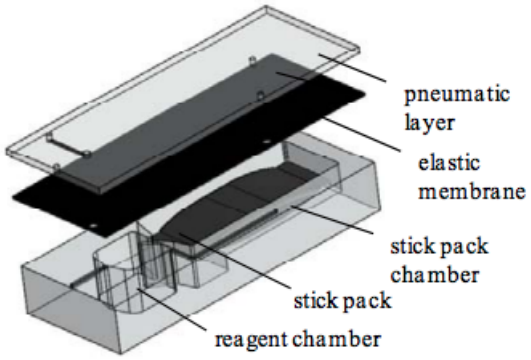

Figure 15. Pressure-Driven Multilayer Polymer Stack [56]

A pressure-driven multilayer polymer stack with integrated stick packs for reagent storage was designed by Czurattis et al. [56]. The stick packs used consisted of a 3 layer film formed by a PET layer, an aluminum layer, and a PE layer. The packs have a peel seam used to release the reagent and a seal seam to contain the reagent. Their system was composed of a pneumatic layer and elastic membrane which could be used to apply pressure on the peel seam for reagent activation. The system is shown in Figure 15. Czurattis et al. achieved great storage properties with this configuration as several reagents showed no significant losses in the packs after being exposed to high temperature and cumulative storage conditions. Extrapolation of their results revealed that reagent losses could be contained to under 5 percent when under high temperature storage conditions. Opening delays were observed after cumulative storage tests but the overall functionality of the device was never compromised. Their solution provides several advantages as it is both simple and robust to the environment.

Abi-Samra et al. [57] devised a novel reagent storage solution that consisted of infrared controlled waxes. Their system was composed of a microfluidic CD-platform which utilized paraffin wax plugs for both valving functions and reagent storage. The paraffin wax plugs were integrated into the platform and essentially

sealed the reagents in the system. An IR heating platform was also implemented into the system and used to actuate multiple wax valves. Abi-Samra et al. utilized an interplay of thermal energy and centrifugal forces for the release of reagents. This configuration facilitates the creation of more intricate systems with the possibility of complex fluid interactions. The fabrication process itself is quite simple but the addition of thermal energy adds another variable into the system. This is an interesting approach that is better suited for when complex fluid interactions are at play.

An exceptionally simple and economical method for reagent storage was developed by Bwambok et al. [58] at Harvard University. Their group repurposed the common packing material, bubble wrap, as containers for liquid storage. Reagents were injected into the bubbles by the use of a syringe and sealed with nail hardener. They found that the aqueous solutions stored in the bubbles evaporated slowly at a rate of 7 percent a week. This was most likely due to vapor evaporation across the membrane and signified that long term storage would have to be achieved through the use of closed or humidified containers. The bubbles provide significant advantages to the reagent storage problem as they are incredibly cheap and could be found everywhere. They are also conveniently sterile and gas permeable which helps to remove the possibility of cross-contamination. Bwambok et al. also demonstrated that the bubbles could be used as cells for electrochemical applications and as cuvettes for fluorescence or absorbance readings. Figure 16 below shows the bubbles being used in various applications. The bubbles are a very attractive and economical solution that could be easily implemented onto a device or used in rapid prototyping.

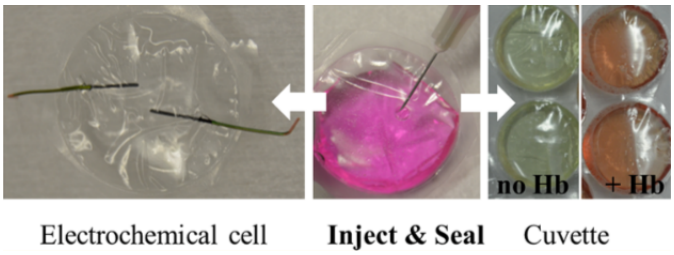

Figure 16. Applications of Bubble Wrap as a Reagent Container [58]

2.4.2 Fluid Control

Fluid control is paramount to the functionality of devices utilizing lab-on-chip and lab-on-paper technologies. The extent and precision to which fluid can be controlled in a device determines the applications that the device is suitable for. Different reactions and tests have different requirements in terms of when certain reagents meet and in what manner. A number of techniques have been developed to control fluids in these devices. These techniques range from simple mechanically actuated valves to more complex systems utilizing temperature for fluid manipulation. Some of the various techniques used in the field today are detailed below.

Li et al. [59] developed a paper-based system using hydrophobized paper in conjunction with plasma treatment. The plasma was used to form well defined hydrophilic channels on the paper. In addition, simple valving elements were created in order to control the fluidics of their device. Li et. al developed switches and filters that were incredibly simple and could be easily integrated into their system. A sliding separator was built that could bridge fluid flow by the pull of a strip. The separator is shown below in Figure 17. Flaps were also designed with similar functionality in mind where fluid could flow across channels by pressing action. The flaps are shown below in Figure 18. These valving systems come with many advantages as they are very simple to fabricate and operate and are also quite reliable. The major disadvantage of such valves is that they are non-autonomous.

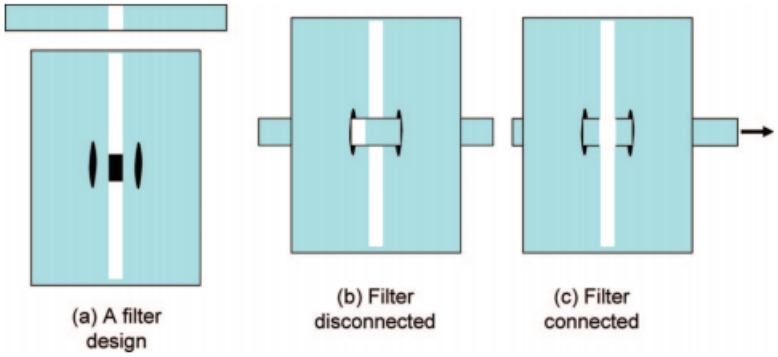

Figure 17. Sliding Separator [59]

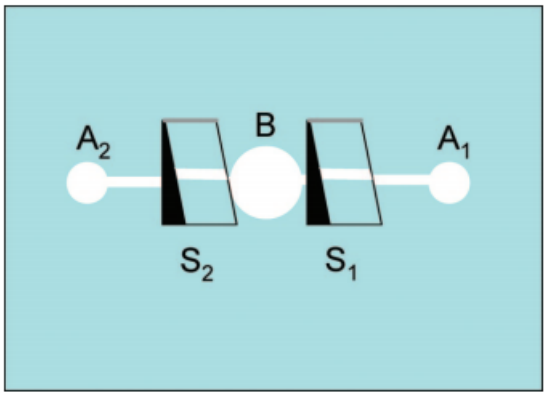

Figure 18. Flap Switches [59]

This presents an issue as human error would always be a factor during operation. Ideally, systems should be completely autonomous in nature.

A 3D paper-based analytical device (PAD) was built by Han et al. [60] to detect infectious human norovirus. Their device consisted of a 3D fluidic network containing layers of wax-patterned paper along with a slip valving design. The design is shown below in Figure 19. The assay could be carried out in a single-step and sequential delivery of multiple fluids was achieved without the need of auxiliary systems. The slip valve utilized in the device is very similar to the sliding separator, activation is performed by simply sliding the slip-top section. The valve is both reliable and quite simple. While this system is more robust and refined

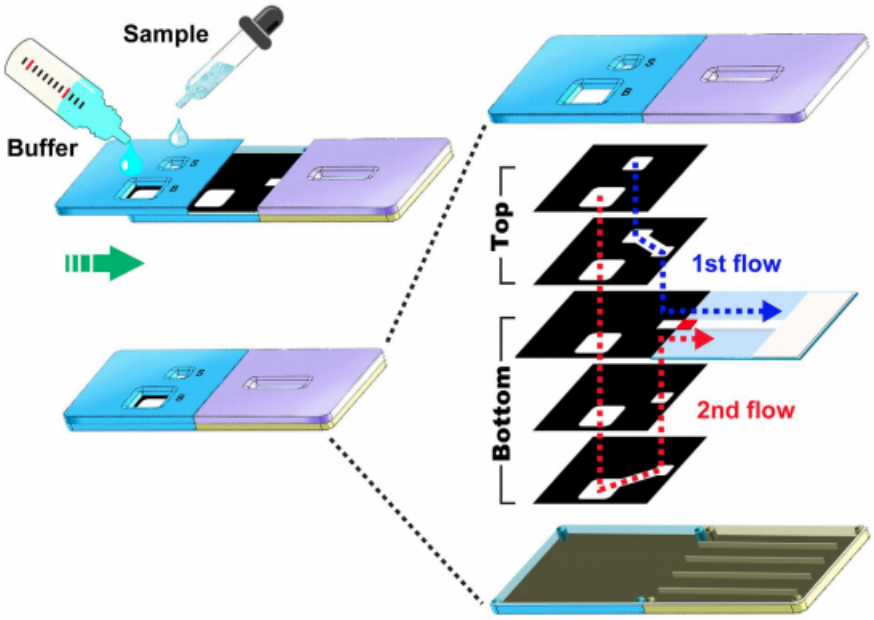

Figure 19. 3D Slip-PAD Device [60]

when compared to the sliding separator and flap switches, it is unfortunately still non-autonomous.

Noh and Phillips [61] developed methods to meter the capillary flow in paper-based devices using wax. These methods were used to control the timing and speed of flow in their systems. Flow control was achieved by the use of minute quantities of paraffin wax in hydrophilic channels. Noh and Phillips found relationships between the quantity of wax and density of wax cover to the flow rate in their devices. This knowledge allowed them to develop very precise time delays using their methods. The main advantage of using such methods is that flow timing could be controlled without the need to lengthen or widen microfluidic channels in a system. These methods are also conveniently very simple and easy to implement onto a system. Flow cannot be completely halted and later opened when required using this wax metering however. This approach is therefore only suitable for flow time delay applications. Figure 20 shows a 3D μPAD prototype with wax metering

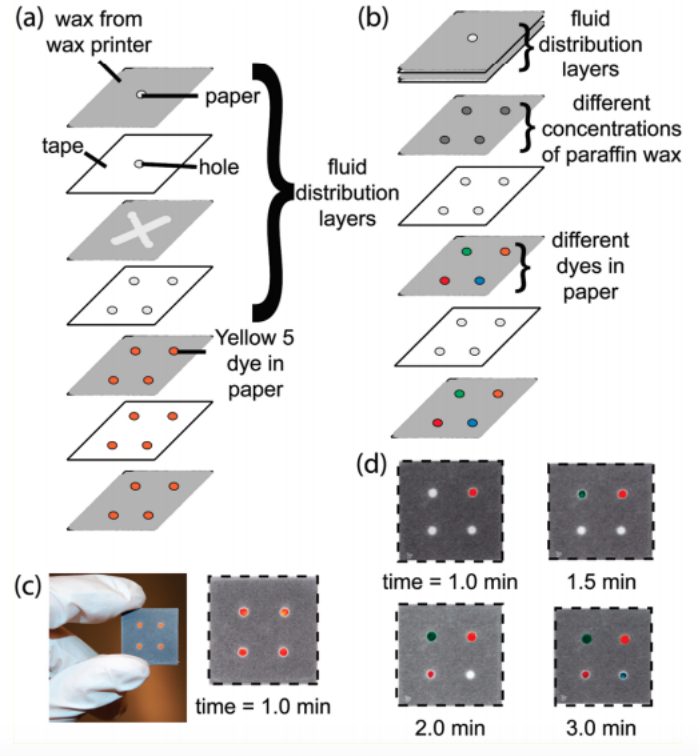

Figure 20. 3D μPAD Prototype With Wax Metering [61]

by Noh and Phillips. (a) and (b) showcase the features of the device while (c) is a photograph of a device that distributed 10 μL of water onto four hydrophilic regions. (d) contains time-lapsed photographs of a device, the wax concentrations starting from the top right circle and proceeding clockwise were 0, 15.7, 31.4, and 47.1 $\mu g\ \mu m^{-3}$ respectively.

A fluid metering technique utilizing sugar delays was developed by Lutz et al. [62]. This method was developed in order to facilitate diagnostic assays on paper that require multiple timed steps. The process consists of simply applying dissolvable sugar onto paper so that programmable flow delays can be created. Lutz et. al were able to achieve fluidic time delays spanning minutes to nearly an hour by varying the concentration of sucrose added. Similar to the wax metering method developed by Noh and Phillips [61], this technique is inexpensive, simple,

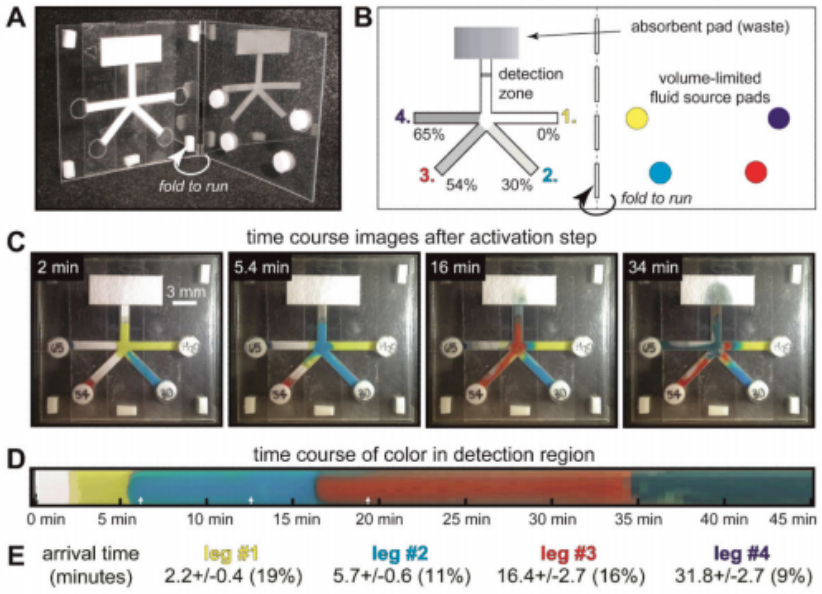

Figure 21. Multi-Step Fluidic System With Sugar Delays [61]

and could be used to sequentially deliver multiple fluids in a system. Sugar also comes with the advantage of being benign to typical assay chemistries. The only issue similar to the wax metering, is that fluid flow could only be impeded and delayed but not halted and later activated. Figure 21 shows a multi-step fluidic system with sugar delays in action.

Lai et al. [63] developed a timing-valve mechanism to perform competitive ELISA procedures on paper-based devices. The timing valves were used to regulate the flow of individual liquids in order to automate sequential steps. The timing-valve mechanism was achieved by using surfactants to dissolve hydrophobic wax barriers printed on a nitrocellulose membrane. Fabrication consists of simply printing the channels and barriers using a wax printer and spotting surfactant ahead of the barriers. The device schematic with running steps are shown in Figure 22. This valve is similar to the wax metering [61] and sugar metering [62] techniques as it is used to time and delay the delivery of fluids. The time it took for the valve to open was directly related to the concentration of the surfactant,

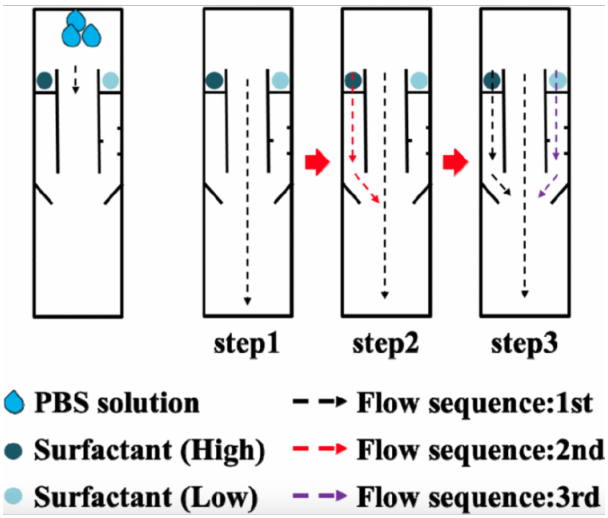

Figure 22. PBST Timing-Valve Mechanism [63]

tween 20 in phosphate-buffered saline (PBST), and the width of the wax barriers. This method is very simple and easy to fabricate but suffers from some limitations as shown by tests done by Amer Charbaji in the Microfluidics Laboratory at URI. Experiments demonstrated that the valving mechanism only works with certain fluids, the barriers were not able to hold or delay water properly for example.

An electrowetting valve for paper-based devices was created by Koo et al. [64]. The valving mechanism was achieved by electrowetting on dialectrics, a naturally hydrophobic material. The electrowetting polarizes the dialectrics which then become hydrophilic. Fabrication of the devices consisted of inkjet printing and spraying conductive hydrophobic electrodes in conjunction with conductive hydrophilic electrodes. Hydrophobic valves were opened by an applied electric potential which altered the fluorinated monolayer on the electrode. Koo et al. observed that the amount of time it took fluid to pass the valve decreased as the electric potential increased. The main advantage of such a valve is the ability to precisely and reliably control the timing of fluid delivery in the system. This mechanism could program complex fluid timing interactions very easily which may

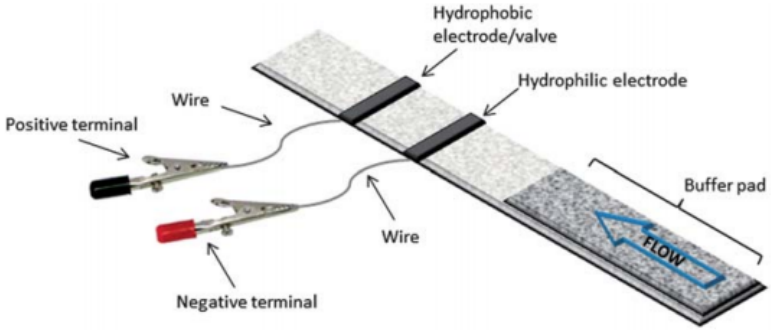

Figure 23. Electrowetting Valve [64]

be advantageous for multi-step assays. The disadvantage however is that the valve not only adds complexity to the fabrication step but also requires electric power. A schematic of the system is shown in Figure 23.

Li et al. [65] created a magnetic timing valve for paper-based devices. They built a system that consists of paper-based magnetic valves that could count time and turn fluidic flow on or off. An ionic resistor is used to trigger an electromagnet for opening and closing of a paper cantilever valve. These resistors are able to detect solutions flowing through them which allow for a precise valving function. The team built normally-closed and normally-open valves from this concept and were able to achieve timing periods up to 30.3 ± 2.1 minutes. Such a mechanism can be used for systems where complex fluid interactions and steps are required. A major disadvantage of the valve is of course the added complexity in fabrication and cost of the overall device. In addition, similar to the electrowetting valve [64], electric power is required for device functionality. Figure 24 shows a schematic of the system (a) and device fabrication steps (b).

Kong et al. [66] developed an actuator device composed entirely of chromatography paper. The team utilized the concept of foldable geometries in origami to create programmable switches for paper-based devices. Activation is achieved by the wetting of crests and throughs in the folds of the actuator. Flow across these

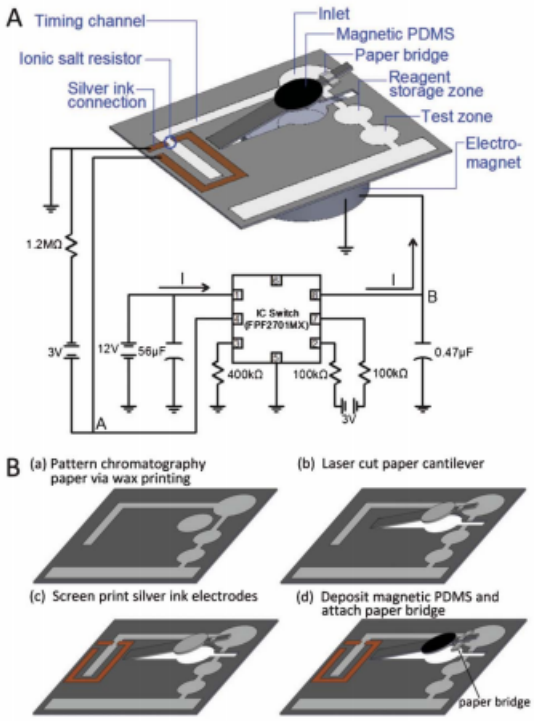

Figure 24. Magnetic Cantilever Valve [65]

areas causes uneven swelling of the paper leading to height changes that can be exploited for actuation of flow. A very fast actuation time (within 2 seconds from wetting) was achieved with minimal consumption of the actuation fluid (4 μL). Kong et al. implemented six switch configurations with this actuation concept. This valving mechanism is very simple, easy to fabricate, and remarkably effective. In addition, it is completely autonomous and could be implemented in multi-step assay tests. Figure 25 shows a device schematic (a) and several switch configurations using this approach (b, c, d).

An autonomous chemically actuated paper-based valve was developed at the URI Microfluidics Laboratory by Chen et al. [32]. The valving mechanism consisted of hydrophilic regions separated by a hydrophobic gap. One of the hydrophilic regions is spotted with surfactant, Tween 20, and once fluid comes in contact with that region, the valve opens as the surfactant mixes with the hy-

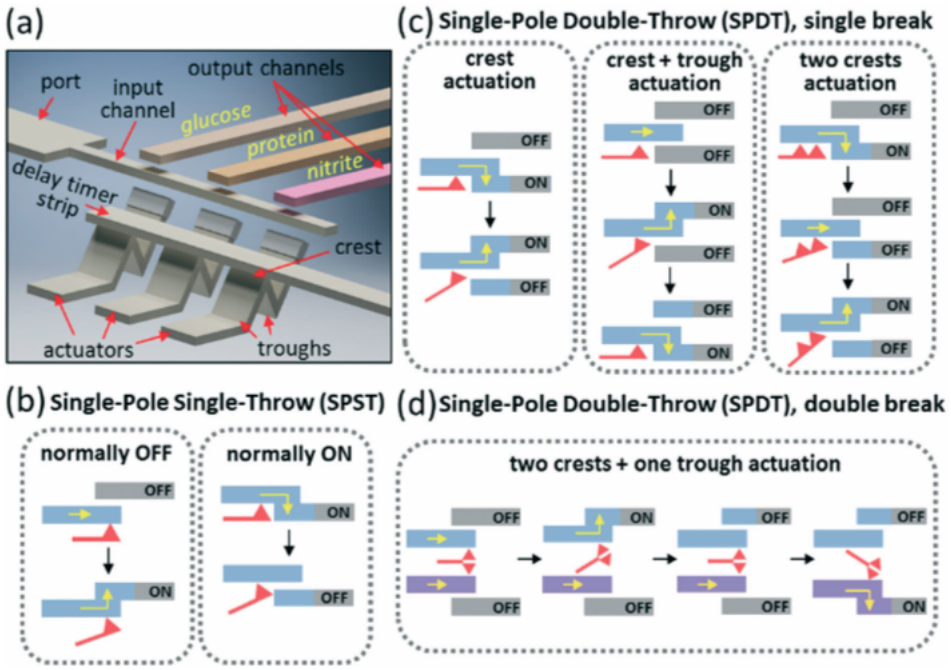

Figure 25. Folded Paper Actuation Device [66]

drophobic barriers. Fluidic diodes were essentially created using this concept and trigger and delay valves as well. Figure 26 shows a schematic of the fluidic diode (a), a microscopic schematic of the surface (b), and photographs of the diode in action (c, d). This is an extremely capable valving mechanism that is completely autonomous. It could be used for multi-step assays but does not come without its share of problems. Alyltrichlorosilane is used to create the hydrophobic regions which adds to the complexity of the fabrication step along with chemical contamination. This concept cannot be used in the case of the molybdenum blue reaction [23] for example as Alyltricholorosilane contains Silicon, one of the major interferents in the reaction. Additional tests at the URI Microfluidics Laboratory also demonstrated that this valving mechanism is susceptible to humidity effects, rendering the valve very unreliable in certain environmental conditions. While very capable, this valve has some limitations that warrant improvements to be made.

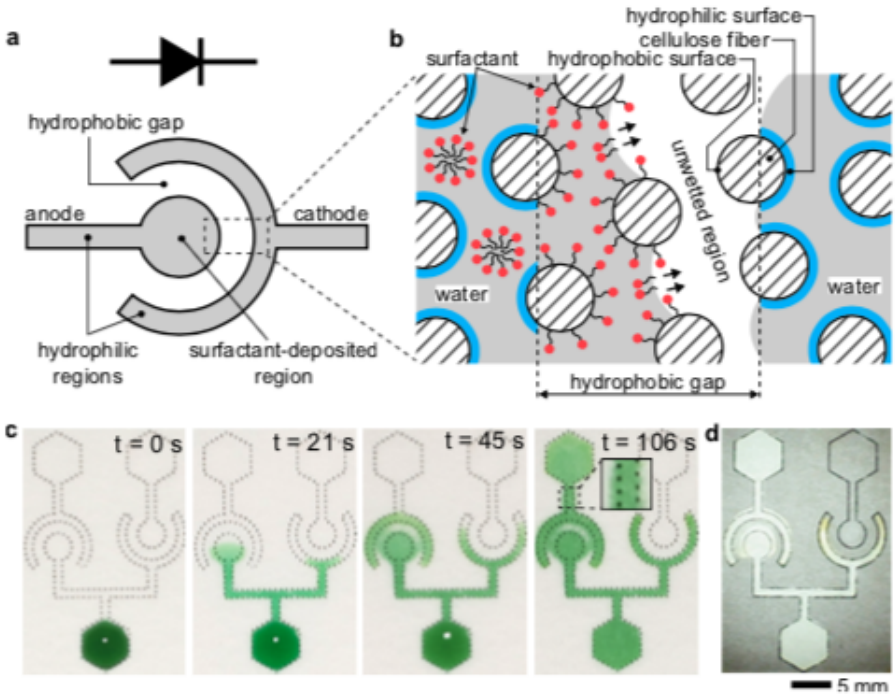

Figure 26. Fluidic Diode [32]

2.4.3 Fluid Mixing

Similar to fluid control, fluid mixing may play a significant role in device functionality depending on the requirements of the application. Mixing can have a direct effect on the sensitivity of the final device and has to be taken into account for some chemical reactions. Lab-on-chip devices normally achieve this task through the use of physical parts while lab-on-paper devices must rely on paper channels utilizing clever geometry. Some of the various methods used to achieve this task are detailed below.

Knight et al. [67] developed a microfluidic, continuous-flow mixer capable of very fast diffusive mixing times. The essence of their method is in reducing the length scale over which fluids must diffusively mix. This mixing is achieved without the generation of turbulence and in an open architecture. The side flow of their system squeezes the inlet flow into a thin stream that rapidly diffuses due to the small length scales. Knight et al. termed this type of mixing 'Hydrodynamic

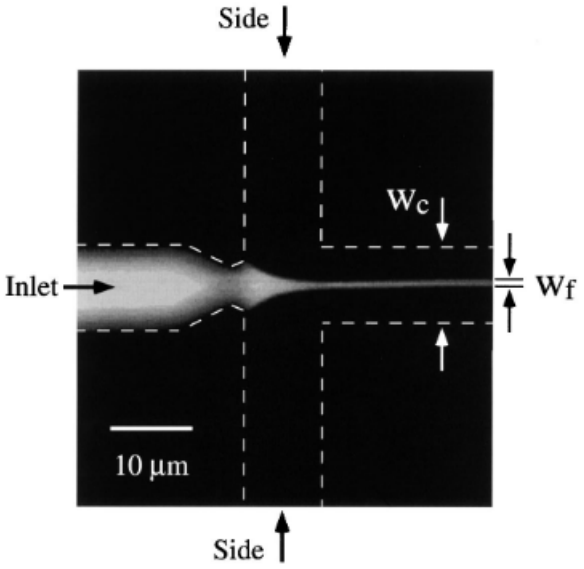

Figure 27. Hydrodynamic Focusing [67]

Focusing'. Such a system could be implemented into lab-on-chip devices but there is of course an added fabrication complexity. Special equipment is needed to produce channels and orifices in the μm scale. Auxiliary mechanisms might be needed as well in order to induce pressure in the system for fluid flow. Figure 27 below showcases the architecture used in hydrodynamic focusing.

Liu et al. [68] utilized chaotic advection to passively enhance fluid mixing. This was achieved by the use of a three-dimensional serpentine microchannel design with C-shaped repeating units. The device was created in a silicon wafer with wet-etching techniques. Experiments showed that the mixing capability of the device increased with a higher Reynolds number as expected. Tests were run against square-wave and straight channel designs. The C-shaped serpentine design had 16 times more mixing when compared to the straight channel and 1.6 times that of the square-wave channel. This design could be easily integrated into a lab-on-chip device but once again requires the use of specialized equipment. Figure 28 below shows the three different microchannels utilized by Liu et al. during their

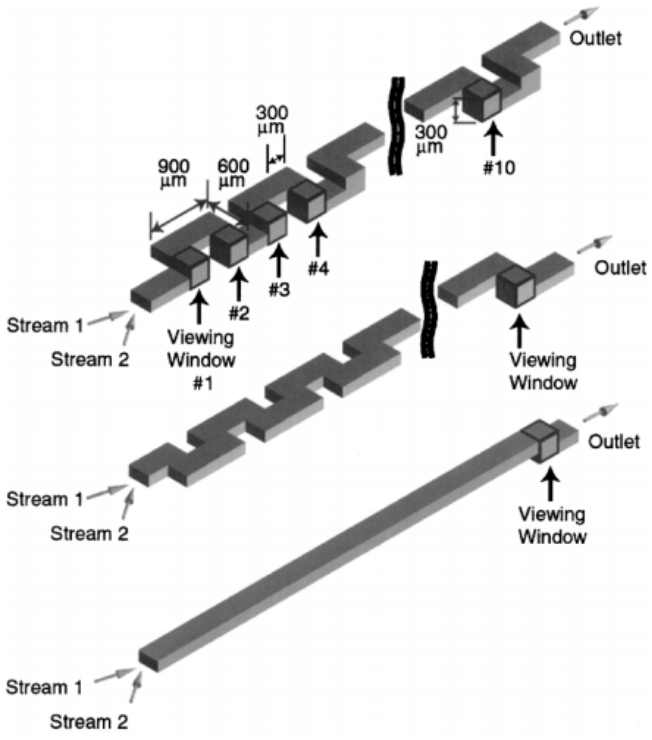

Figure 28. 3D Mixing Microchannels [68]

tests. From top to bottom, the three designs are the C-shaped serpentine, the square-wave, and the straight channel.

Piezoelectric disks were used for acoustic micromixing on a lab-on-chip device by Liu et al. [69]. This technique is based on the principle of cavitation microstreaming. Air bubbles were trapped inside a solution using air pockets and later set into vibration with the piezoelectric disks. Frictional forces are then generated at the bubble/liquid interface which induce bulk fluid circulation around the bubbles. Liu et al. found that the best mixing was achieved when the air bubbles had a size and resonant frequency selected in accordance to the insonation frequency induced by the piezoelectric disk. Experiments showed that this technique significantly reduced the time needed for complete mixing when compared to pure diffusion-based mixing. This method does come with its share of disadvantages however as there is some complexity added to the fabrication of the device and the

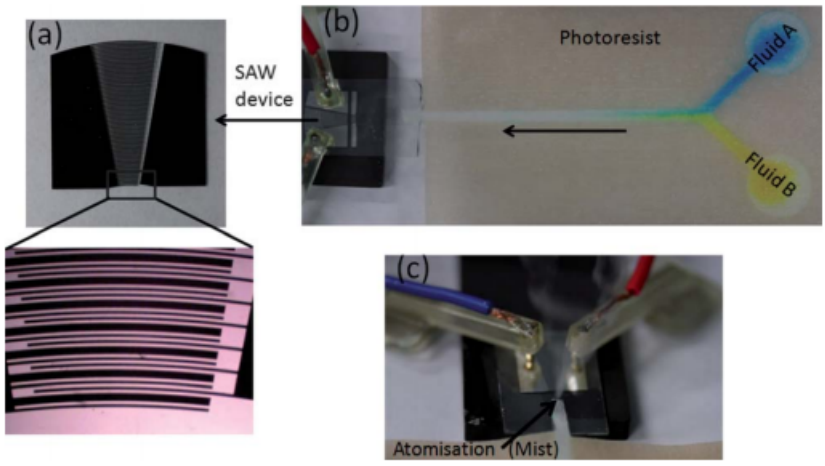

Figure 29. SAW Mixing [70]

need for an external power source to operate the piezoelectric disks.

Rezk et al. [70] developed a convective actuation mechanism in a paper-based microfluidic device that utilizes surface acoustic waves to drive mixing. The motivation behind this technique is the added control and uniformity of flow achieved when using surface acoustic wave (SAW) microfluidic transport when compared to capillary flow. Capillary-driven mixing comes with some limitations due to fibre-alignment and paper texture. The scale of the paper fibres are generally significant when compared to the length scales of features in a system which often results in difficulty mixing. Rezk et al. found that the mixing achieved in their system was both rapid and consistent when utilizing acoustic waves. The device was built by patterning chromium-aluminium SPUDT electrodes on a single crystal lithium niobate (LN) piezoelectric substrate. The gap and width of the interleaving electrode fingers controlled the frequency produced by the system. The acoustic waves could then be generated by applying a sinusoidal electrical signal on the substrate at the system frequency. This technique achieved improved control at the expense of fabrication complexity and the need for external power. Photos of the system with a Y-channel are shown in Figure 29.

2.5 Mechanics of Flow in Paper

There are various equations that govern the rate of fluid flow through paper. One can regulate flow by using these equations to manipulate channel geometries in paper-based devices. The equations are distinguished by the state of the medium through which they flow (dried or wet). They are explained in great detail throughout the next few sections. In addition, tests were performed on different filter paper types and geometries to measure their effect on flow rate. These supplementary tests are presented in Appendix A.

2.5.1 Flow Through a Dry Medium

The simplest case is fluid flow through a dry porous material. This type of flow is governed by Washburn's Equation [71], also known as the Lucas-Washburn Equation for Richard Lucas who had a similar discovery three years earlier [72]. The equation describes flow in cylindrical capillaries and can be used in a variety of applications including fluid flow through paper. The equation is shown below in Equation 1:

$$L = \frac{\gamma D t}{4\eta}$$

Equation 1

where D is the pore diameter, γ is the surface tension, η is the dynamic viscosity of the fluid, and t is the time it takes the fluid to flow a distance L in the paper. Water is the most commonly used fluid with an estimated surface tension of 0.0728 N/m with air and dynamic viscosity of 0.001 N s/m^2 at room temperature. Washburn's Equation makes three strong assumptions to be valid in paper flow. First the channel cross section should be constant, second there must be a non-limiting fluid source, and third the paper should be dry. This is not always the case in paper-based devices of course but the equation is still quite useful in the development of

channels and material selection.

2.5.2 Flow Through a Wetted Medium

Flow through a porous membrane that is already wetted is governed by Darcy's Law [73]. It is shown below in Equation 2:

$$Q = -\frac{\kappa W H}{\mu L}\Delta P$$

Equation 2

where Q is the volumetric flow rate, W is the width of the channel, H is the height of the channel, κ is the permeability of the medium, μ is the dynamic viscosity of the fluid, and Δ P is the pressure difference over the length L of the fluid flow. The flow rate of the fluid can be derived by assuming a constant channel cross-sectional area. This simplified version is shown below in Equation 3:

$$q = -\frac{\kappa}{\mu L}\Delta P$$

Equation 3

Because the volumetric flow rate is constant across a channel, one can derive the time it takes for a fluid to cross a pre-wetted channel. This equation is simply found by dividing the volume by the volumetric flow rate and substituting Darcy's Law. The equation is shown below in Equation 4:

$$t = \frac{V}{Q} = \frac{\mu L^2}{\kappa \Delta P}$$

Equation 4

These equations prove to be very useful in the initial design stages of paper-based microfluidic devices.

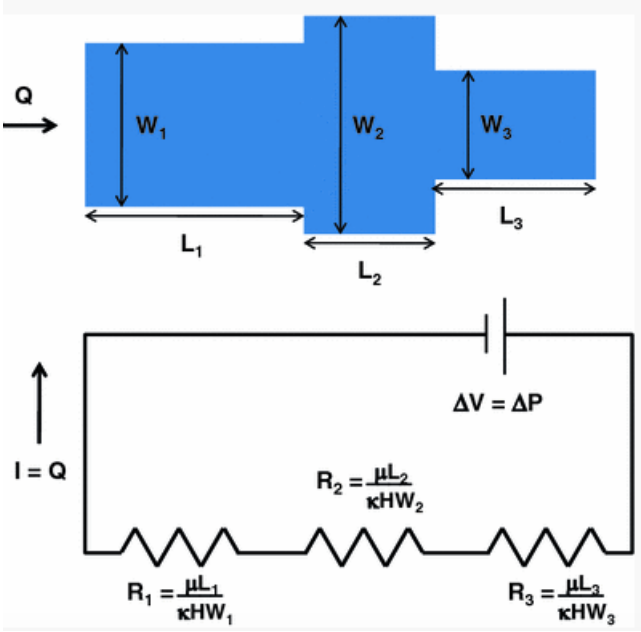

Figure 30. Electrical Analogy [74]

2.5.3 Electrical Circuit Analogy

Electrical analogies have been made for fluidic circuits in order to simplify design procedures and aid in circuit interpretability [74]. Resistance of flow through channels of varying widths has been modeled using Darcy's Law and Ohm's Law. Figure 30 below showcases a diagram of the electrical analogy for this particular resistance case.

The behavior of the circuits above for N segments i of varying widths are modeled using the following equation:

$$Q = \frac{\Delta P}{\frac{\mu}{\kappa} \sum_{i=1}^{N} \frac{L_i}{W_i H_i}} = \frac{\Delta P}{R_{eq}}$$

Equation 5

where Q is the volumetric flow rate, ΔP is the pressure change along the direction of the flow, μ is the dynamic viscosity of the fluid, κ is the permeability of the medium, $W_i H_i$ is the cross-sectional area of segment i perpendicular to the flow, L_i

is the length of segment i in the direction of flow, and R_{eq} is the fluidic equivalent of resistance. Q in this case is analogous to current while ΔP is analogous to voltage change.

2.6 Color Science

Colorimetric methods are a cost-effective and efficient solution in chemical detection. Color formation is of course the basis of the process and as such, a fundamental understanding of color science is essential for success. There are several laws that govern the relationship between color and light. Knowledge of these laws can be a great aid in designing an effective system for color quantification. An overview of the major concepts relating to light and color theory are detailed below.

2.6.1 Light and Color

The nature of visible light has always been a mystery to mankind. Light is essentially electromagnetic radiation at specific frequencies and wavelengths. It has been shown that light can behave both like a particle and a wave. This behavior has been coined the term duality and is a fascinating concept belonging to the realm of quantum mechanics. At a speed of 299,792 kilometers per second, light also happens to be the fastest thing in the universe. The relationship between the speed, wavelength, and frequency of light is shown in Equation 6.

$$c = \lambda\nu$$

Equation 6

where c is the speed of light, λ is the wavelength, and ν is the frequency. The formation of color is directly related to the wavelength of light and how it interacts with objects. Visible light is formed when the wavelength of light is within the visible spectrum (approximately 390 nm to 700 nm). The electromagnetic spectrum

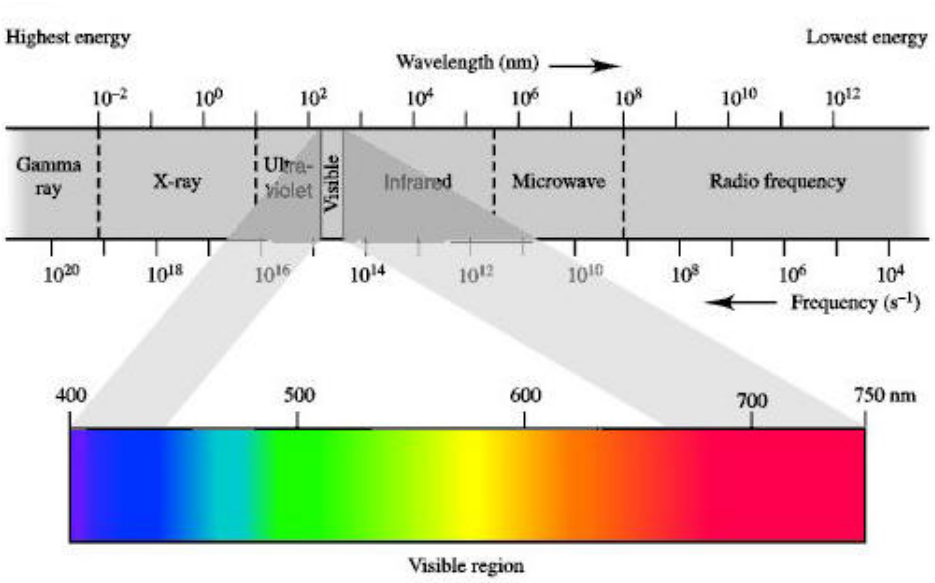

Figure 31. Electromagnetic Spectrum [75]

is shown in Figure 31 [75]. As shown, visible light occupies a very narrow band between the ultra-violet and infrared regions of the spectrum.

2.6.2 Light Absorption, Reflection, and Transmission

Objects can reflect, transmit, and absorb light. Light is absorbed by an object when the frequency of light matches the vibrational frequency of the electrons in a material. This vibrational energy is then converted into thermal energy which will never be released in the form of light again. Reflection and transmission of light happens when the frequency of light does not match the vibrational frequencies of objects. When light strikes such materials, the electrons vibrate very briefly and then light is reemitted from the object. As the name suggests, transmission occurs when an object is transparent and allows light to simply pass through. Reflection takes place on opaque objects that can reflect some light from their surface.

Absorption, reflection, and transmission are important concepts because they have an effect on the color of objects and in turn on chemical reactions. The relationship between absorption, reflection, and transmission is shown in Equation

7 [76].

$$\rho + \tau + \alpha = 1$$

Equation 7

where ρ is the flux reflected by an object, τ is the flux transmitted by an object, and α is the flux absorbed by an object. Absorption spectra are commonly used in analytical chemistry to identify wavelengths of maximum absorption for a chemical. These in turn can then be used to better quantify chemical concentrations by focusing on areas with maximal sensitivity. A colorimetric detection approach such as the molybdenum blue method has an absorption maximum in the infrared for example. One can achieve a better limit of detection with this method by simply taking measurements in the infrared region.

The concentration of a chemical and its absorbance are directly related. This relation is linear at low enough concentrations. The relationship between the two can be explained by Beer-Lambert's Law [77] shown in Equation 8.

$$A = \epsilon bc$$

Equation 8

where A is absorbance, ϵ is the molar absorptivity, b is the path length of the sample, and c is the concentration of the compound in the solution. One can easily determine the concentration of a chemical by forming a calibration curve based on the absorption of said chemical at a specific wavelength. Because absorption, reflection, and transmittance are related, this same concept applies to visual quantification based on color intensity. One can easily infer the color of a chemical reaction based on the absorption spectrum. The color formed is essentially based

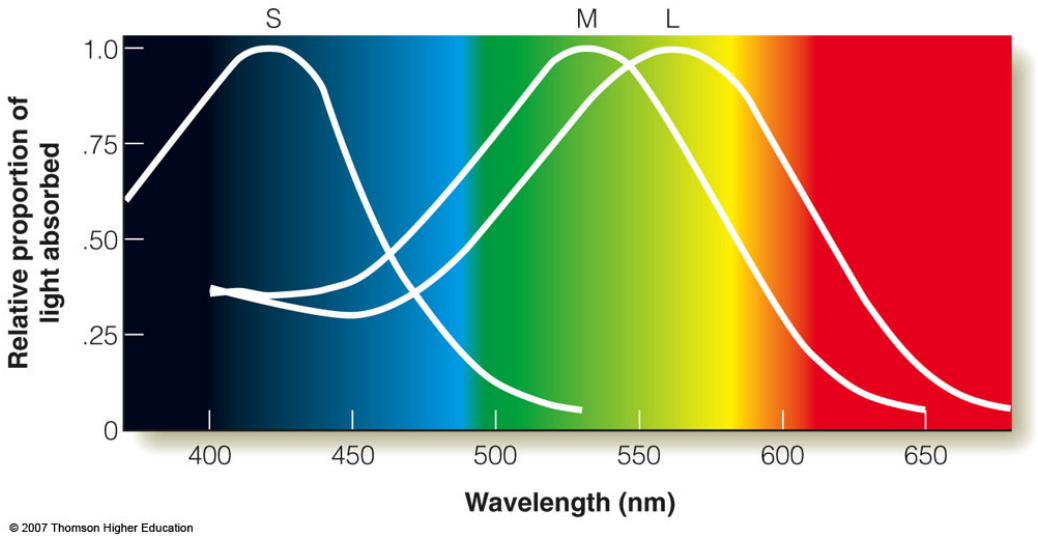

Figure 32. Spectral Sensitivity of Cone Cell Types [79]

on the wavelengths that didn't get absorbed. The molybdenum blue reaction produces a blue color for example because the red and green regions of the spectrum are absorbed while the blue is not.

2.6.3 Color Spaces

Color spaces [78] were created in order to identify colors numerically. These spaces are essential for performing scientific and quantifiable measurements. The RGB color space is the most commonly used space and is based on the additive RGB color model. This space is composed of three color channels: red, green, and blue. It was designed to correspond with the three cone cell types in the human eye. These cone cells are responsible for human trichromacy where each cell type responds to a different band of light. The response of each cone cell type is shown in Figure 32 [79]. As shown, the S type responds to short wavelengths in the blue region, the M type responds to wavelengths in the green region, and the L type responds to longer wavelengths close to the red region.

The RGB space is also used to output and display information in virtually every device with a screen. RGB values can be digitally constrained to 8 bits per

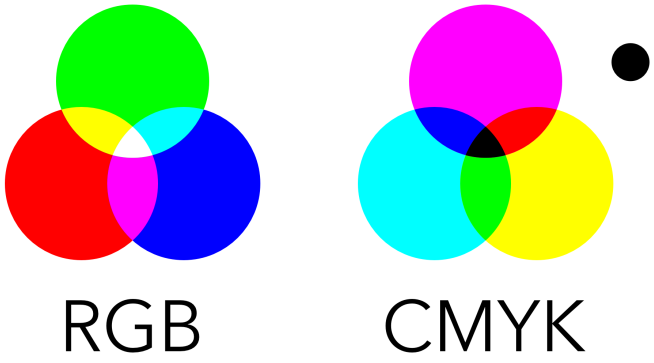

Figure 33. RGB and CMYK Color Spaces

color where each color takes a value from 0 to 255. Pixels then individually output values that form what we see on a screen. Almost every conceivable color can be created using different combinations of RGB values. Black is formed when all values are zero while a maximum of 255 for all values forms white. Colors formed from chemical reactions can then be digitally quantified in this space using camera and detection technologies detailed on the next section.

The CMYK color space is used in the printing process. This color space is based on subtractive colors instead of additive colors used in the RGB scale. Subtractive colors start with a white substrate and color is subtracted from the white in order to create images. This property makes them perfect for the printing process where inks are combined to created different colors on white paper. The four CMYK colors are cyan, magenta, yellow, and black. While this color space is not used in detection technology, it can be very helpful for control of ink deposition in the printing of paper-based devices. The RGB and CMYK color space models are shown in Figure 33.

2.7 Camera and Detection Technology

The performance of a colorimetric device is only as good as the quantification methods employed. Camera and detection technology is an important part to

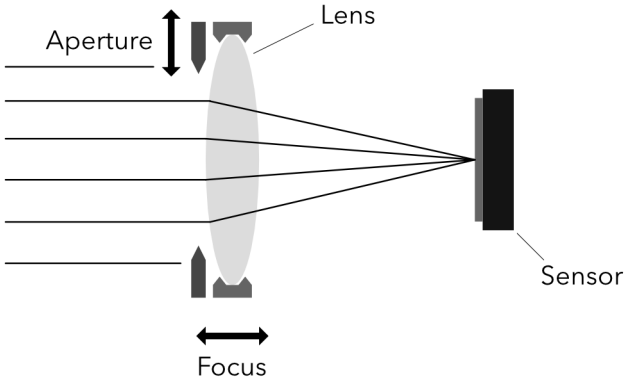

Figure 34. Camera Architecture

the final success of a system. Proper technologies must be in place to effectively measure phosphate levels in conjunction with a suitable chemistry. A significant part of the work in this paper involved the creation of detection technologies capable of enhancing performance and conveniently measuring phosphate levels in the field. Much of the design concepts and science involved in the creation of these technologies is detailed below.

2.7.1 Camera Architecture

Modern day cameras all share a similar general architecture. These cameras are fundamentally composed of two main components: a lens and a sensor. The lens is used to focus light onto the sensor which then converts light into electrons. Similar to the iris in the eye, cameras also have a component named the diaphragm which can regulate the amount of light reaching the sensor. The diaphragm changes the effective diameter of the lens, also known as the aperture. This function is extremely important as different light intensities are observed in the environment. Focusing can be controlled by moving the lens towards or away from the sensor. A diagram of the basic camera architecture is shown in Figure 34.

Sensor	CCD	CMOS
Pixel Signal	Electron Packet	Voltage
Chip Signal	Analog	Digital
Fill Factor	High	Moderate
Responsivity	Moderate	Moderate – High
Noise Level	Low	Moderate – High
Dynamic Range	High	Moderate
Uniformity	High	Low
Resolution	Low – High	Low – High
Speed	Moderate - High	High
Power Consumption	Moderate – High	Low
Complexity	Low	Moderate
Cost	Moderate	Moderate

Table 1. CCD vs. CMOS Sensors [80]

2.7.2 Sensors

The sensor is responsible for the output obtained when photos are taken. As such a review of sensors and their respective technology is of critical importance in the pursuit of converting digital image data into scientific measurements. There are many types of sensors in use today. The most common sensors are CCD (charged coupled device) and CMOS (complementary metal-oxide-semiconductor). CCD sensors use a very old technology that is generally used for video broadcasting. CMOS sensors are much cheaper and have lower power consumption than CCD sensors. This makes them perfect for integrating into small products such as mobile phones. CCD sensors were long considered superior due to their high image quality but modern CMOS sensors have been upgraded to match and even surpass this old technology. Table 1 shows a general comparison between CCD and CMOS sensors [80].

The RGB app (iPhone camera) and infrared detection unit (Raspberry Pi NoIR camera) detailed in the Methodology all utilized CMOS sensors. Both sensor

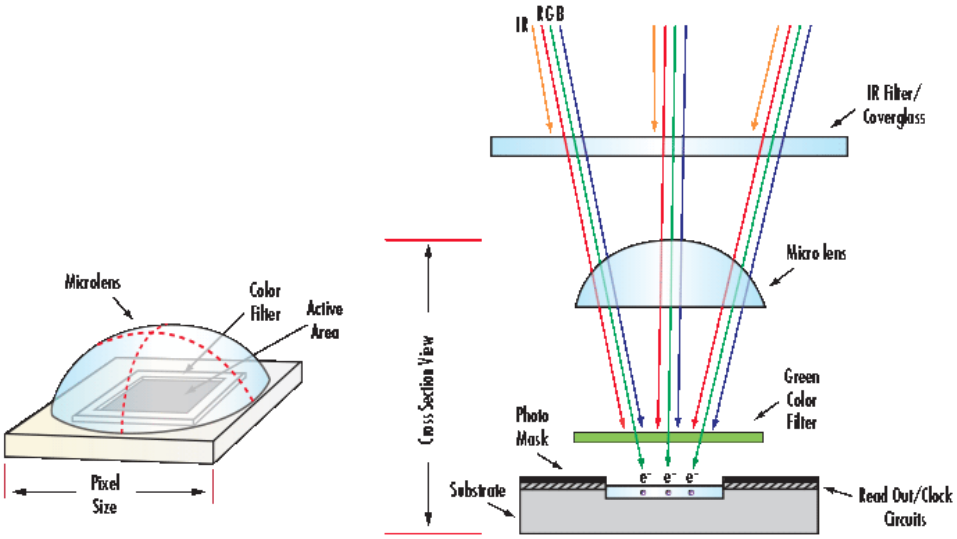

Figure 35. Camera Sensor Pixels [80]

technologies possess some of the same features. Every sensor has pixels which are responsible for collecting the light coming from the lens. The pixels can be either photodiodes or photocapacitors which generate a charge in accordance to the light intensity incident on them. Pixels are generally square and range in sizes from 3 to 10 μm. Every pixel consists of a microlens along with a color filter. Each color filter belongs to one of the three color channels: red, green, or blue in the RGB color space. The filters are necessary in order to produce color images. Figure 35 shows an upclose view of these pixels [80].

The sensor pixels are generally arranged in whats known as the bayer pattern [81]. This mosaic color filter array pattern is responsible for separating incoming light into red, green, and blue colors. The bayer pattern is shown in Figure 36 [80]. As shown, the array consists of 25% red filters, 50% green filters, and 25% blue filters. This distribution was chosen to mimic the physiology of the human eye. As explained in the color spaces section, humans exhibit trichromacy due to the three cone cell types in the human eye. Because the M and L cell types overlap substantially, the human eye is naturally more sensitive to the green region of the

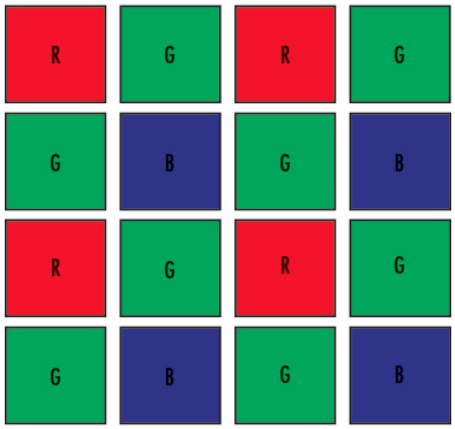

Figure 36. Bayer Pattern Mosaic [80]

spectrum.

Sensor size is also immensely important to the final image quality. The size of the sensor determines the system's field of view (FOV). A larger sensor with the same lens as a smaller counterpart will always yield a greater field of view. Sensor size is of course constrained by the product dimensions so sensors in mobile phones are typically much smaller than those in DSLR cameras for example. Modern day cameras have come a long way however and even small systems are capable of achieving great picture quality.

2.7.3 Aperture, Shutter Speed, and ISO

Exposure is the amount of light that reaches the sensor in a camera. This is a critical photography variable as it has a direct influence on the quality of the photo taken. Three elements are responsible for controlling the exposure on a shot: the aperture, shutter speed, and ISO. Regulating these three variables is extremely for scientific measurements as changing even one of them has an effect on the RGB pixel output.

The first element, the aperture [82], essentially controls the diameter of the lens as explained in the camera architecture section. This of course has a direct

effect on the amount of light reaching the sensor. The smaller the diameter, the less light that is able to pass through and vice versa. The aperture also has an effect in the depth of field of the image. Larger apertures result in a shallower depth of field when compared to smaller apertures. Aperture is normally specified as a f-number in photography. These numbers represent the ratio of focal length to the effective aperture diameter. The f-numbers therefore have an inverse relationship with the aperture size and larger numbers correspond to smaller aperture diameters. Cameras normally have f-stops that can be set on the lens that correspond to a change of 1.41 in the f-number per stop. This change results in a factor of 2 increase/decrease in light intensity.

The shutter speed is a variable belonging to the camera shutter [83]. The camera shutter is a component that blocks light from reaching the sensor until a photo is taken. Shutter speed is simply the length of time in seconds that the camera shutter is open. In other words, the length of time that light is exposed onto the sensor for a photo. Shutter speed has two main effects on a photo, motion blur and exposure. A longer shutter speed will blur moving objects in a photo creating a sense of motion. Short shutter speeds have essentially the opposite effect and will freeze motion in a photo. Intuitively, longer shutter speeds also result in brighter photos as the camera sensor is exposed to light for a longer period of time. Taking photos with long shutter speeds, also known as long exposure, is of great use in dark settings.

The last element and often the most misunderstood affecting the exposure of a photo is the ISO [84]. The ISO in digital photography is the applied gain. This gain is applied to the image after it is taken in order to increase the brightness. This setting is extremely useful as changing the ISO value allows for different shutter speed and aperture values to be used. The increased brightness level comes

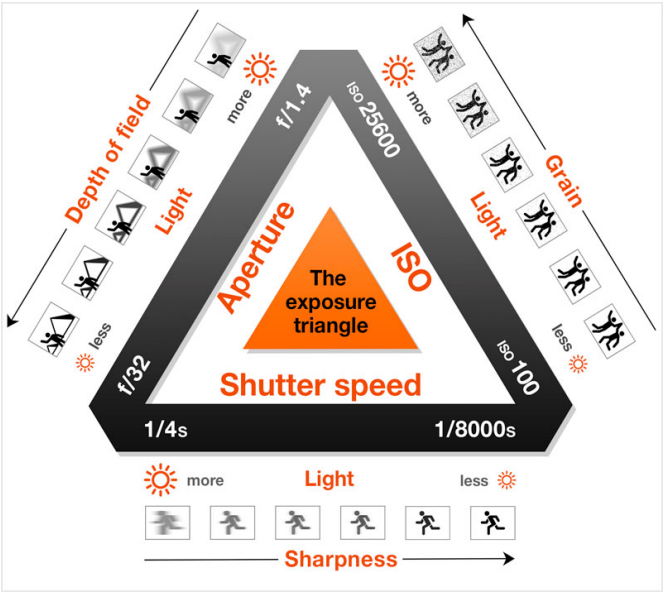

Figure 37. Exposure Triangle [85]

at a cost however as the image sharpness and dynamic range decrease. Every photo taken has noise due to heat and imperfections from the camera. Higher ISO values also has the added effect of increasing noise, sometimes referred to as grain, in the image. This is of course to be avoided as increasing the noise not only results in a less desirable photo but also decreases the available signal for scientific measurements. ISO values must therefore be set with caution.

The aperture, shutter speed, and ISO are known as the exposure triangle in photography. Creating quality images is then a balancing act between the three elements. A diagram of this triangle and how each of the elements relate to image quality is shown in Figure 37.

2.7.4 White Balance

One of the most important elements affecting the way an image looks is the white balance [86]. Our eyes and brain automatically adjust and compensate for different lighting conditions. This means that a white object will appear white regardless of the setting. Cameras on the other hand must rely on a setting called the

Figure 38. White Balance Presets [87]

white balance in order to compensate for different light environments. The white balance automatically adjusts itself programmatically but sometimes a manual adjustment is necessary in order to achieve a realistic representation of colors in a photo. This setting is of utmost importance as it will have a direct effect on the RGB values measured on a photo.

The white balance essentially rescales the RGB channels in order to change the color representation in a photo. Manually setting the white balance normally involves taking a photo of something white in the same lighting conditions that a photo will be taken. The camera can then programmatically adjust the RGB gains in order to match the white and in turn set the desired white balance. Similar to the exposure settings explained in the last section, the white balance must be controlled in any scientific environment so that consistent and reproducible results are obtained. Figure 38 shows the effect of a camera's different white balance presets on a photo.

The white balance along with all of the different camera variables discussed in this section were key parameters to much of the detection work in the next few chapters. The RGB App and Infrared Detection Unit sections will dive into detail of how such variables could be controlled in order to obtain reproducible results.

CHAPTER 3

Methodology

This chapter details the methodology used in the various building blocks of this work. The first section deals with the construction of a light box that could provide a stable light source for RGB measurements. Experiments performed on commercially available devices using the light box are then detailed in the next section. The RGB App section details the development of an iPhone app suitable for public use that is capable of accurately measuring RGB values. The next section elaborates on an online data center that was constructed in conjunction with the iPhone app in order to store measurements, GPS location, and environmental conditions of readings. The methodology of the Lab-on-Chip device constructed with the help of Mindy Levine's Chemistry Team at the University of Rhode Island is addressed in the Lab-on-Chip section. In order to improve device sensitivity, a box capable of taking measurements in the infrared was built and is detailed in the Infrared Detection Unit section. A Lab-on-Paper device utilizing carbon nano dots was developed in conjunction with Jack Breen at Providence College and is detailed in the Fluorescent Lab-on-Paper Device section. Finally the last section describes the construction of a box capable of measuring fluorescence for use with the fluorescent Lab-on-Paper device.

3.1 Light Box

In order to take colorimetric measurements of devices, a stable and consistent light environment is needed. This light environment ensures that the lighting in every measurement is consistent and therefore scientific conclusions could be drawn. A general light box was constructed in order to serve a variety of different tests and devices. The light box is partly modular so individual parts such as the

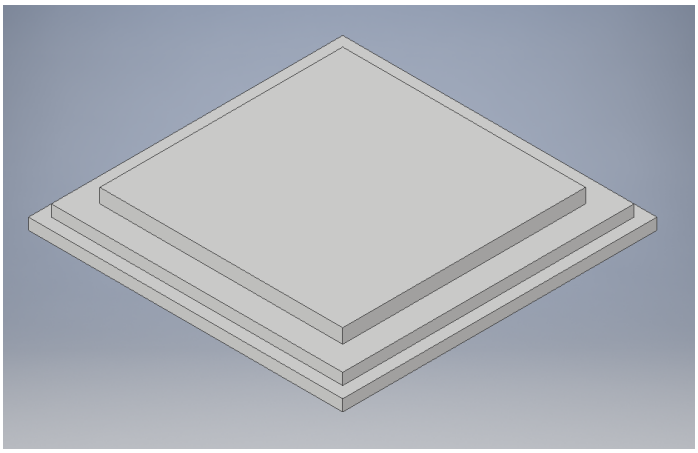

Figure 39. Light Box - Bottom Platform

platform and cover could be replaced with camera and device specific modified parts. This way the box could easily be modified later on for commercial use with a device. The schematics of all light box parts are shown in Appendix A. The methodology that went into creating the box is detailed below.

3.1.1 Box Design

The first step of the light box construction was the 3D CAD design of the parts. Parts were drawn on Autodesk Inventor [88]. The box consisted of three main parts: a bottom platform, a surrounding wall sleeve, and a top cover. These parts were designed with the intention of being modular so that any individual part could be modified for a specific device without a complete redesign being necessary.

The bottom platform was designed with three steps. The bottom step for mating with the wall sleeve, the middle step for any auxiliary additions, and the top step/platform for laying out devices. A handle was also integrated into the backside for easy detachment of the wall sleeve. The bottom platform is shown in Figure 39.

The wall sleeve is simply a 11 cm x 11 cm hollow wall that is 3 cm thick

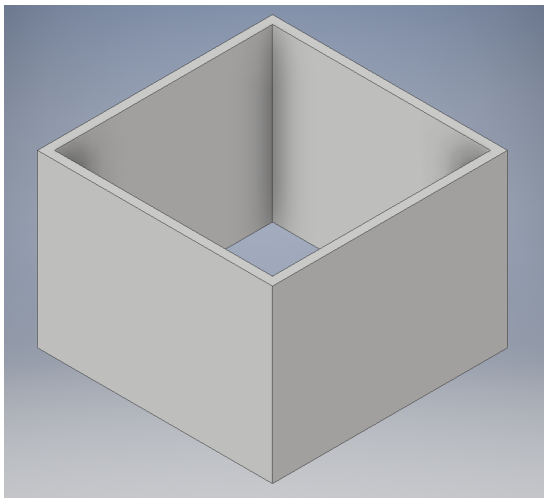

Figure 40. Light Box - Wall Sleeve

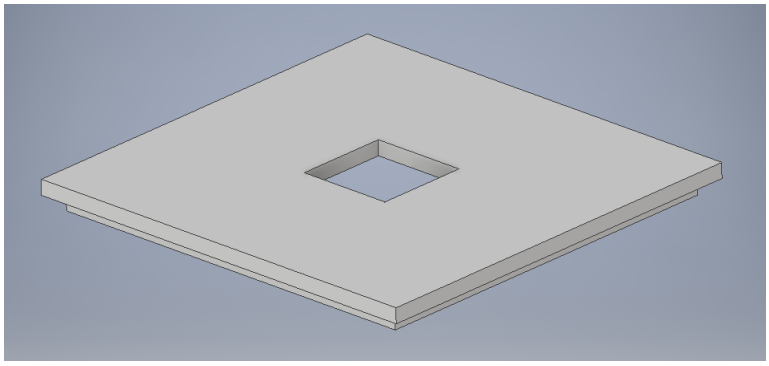

Figure 41. Light Box - Top Cover

all around. It houses the light sources and its electronics as will be shown in the Lighting and Electronics section later on. The wall sleeve is shown in Figure 40.

The top cover mates to the wall sleeve and has a 25 cm x 25 cm hole for cameras to peer into the box. A dark fabric is also attached to the cover in order to shield the camera and box from any outside light sources. The cover could be easily modified to accommodate different camera and phone sizes. The top cover is shown in Figure 41.

All three parts together make up the framework of the box as is shown in the wireframe drawing in Figure 42.

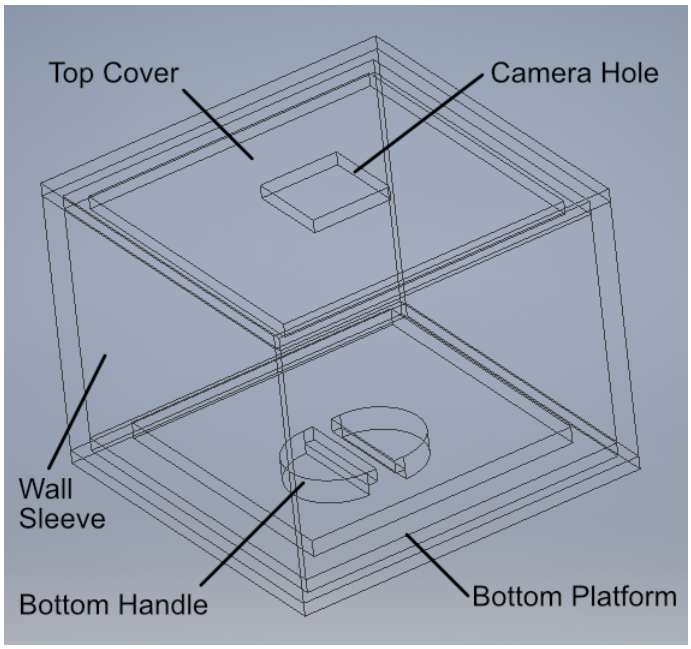

Figure 42. Light Box - Main Framework

3.1.2 Lighting and Electronics

A strong and reliable light source was the most important part of the light box as it is responsible for a consistent light environment. Many light sources were considered but LEDs were chosen as they are cheap, produce minimal heat, have a long lifetime, and come in a variety of different colors and intensities. The next important consideration was the color temperature. LEDs commonly come in a variety of color temperatures ranging from a warm yellow/white (2700 K) to a blueish daylight color (6500 K). A color temperature chart [89] is shown in Figure 43.

A pure white color without any blue or red traces is desired in order to take colorimetric measurements. As such, 4000 K was chosen as the final color temperature since it is regarded as a neutral or natural white. A 3ft IP65 LED Flex Strip was bought from LEDsupply.com as the light source [90]. The specifications of the strip are shown in Figure 44.

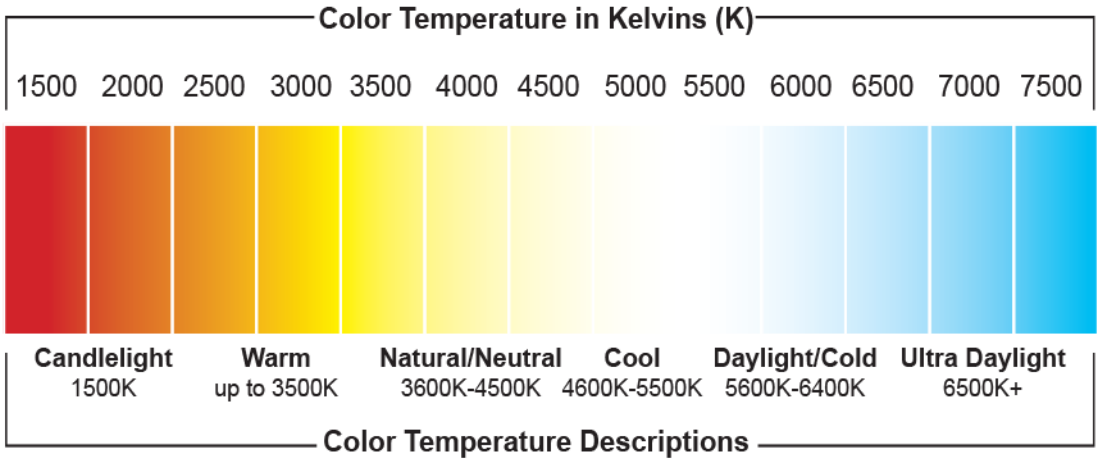

Figure 43. Color Temperature Chart [89]

P/N	Color	Kelvin (K)	Beam Angle °	Luminous Flux (lm/m>	CRI	Efficacy (lm/w)	Input Voltage (VDC)	Power (W/m)
R6030AA-NWT	Neutral-White	4000K	115	540	>75	75	12	7.2

Figure 44. LED Flex Strip Specifications [90]

As shown at a length of 3ft (1m), the strip outputs 540 lumens. The beam angle is also quite wide at 115 degrees. This LED strip needs an input voltage of 12v to operate. An electronic box had to be constructed in order to provide a power source for the LEDs and a toggle switch to turn the LEDs on and off. a23 batteries were perfect for this application as they are very compact and rated at 12v. An a23 battery holder and a simple FBApayipa 2 pin SPST toggle switch were bought off of amazon. The LED strip, a23 battery holder, and toggle switch are shown in Figures 45 a, b, and c respectively.

A simple circuit had to be wired up to produce the desired functionality of the box. The LED strip hot end connects to one tab of the toggle switch while the battery holder connects to the other tab. The grounds from the LED strip and battery holder simply connect to one another. The circuit diagram is shown in Figure 46.

A small compartment had to be designed in order to house the electronics of

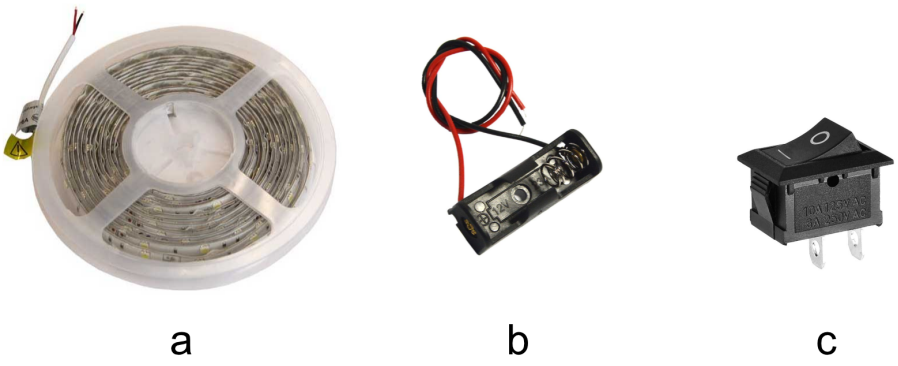

Figure 45. LED Flex Strip [90], a23 Battery Holder, and SPST Toggle Switch

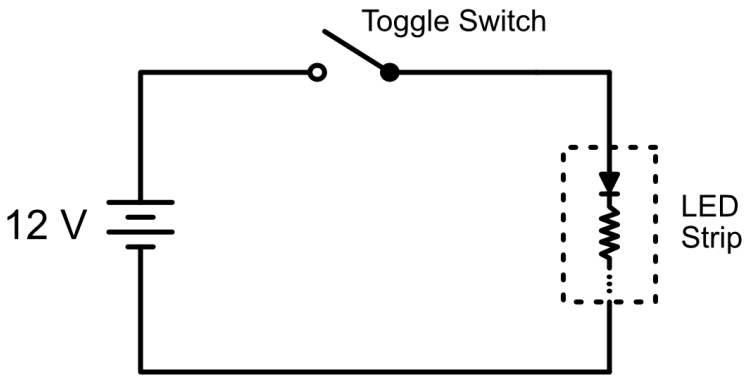

Figure 46. Light Box - Circuit Diagram

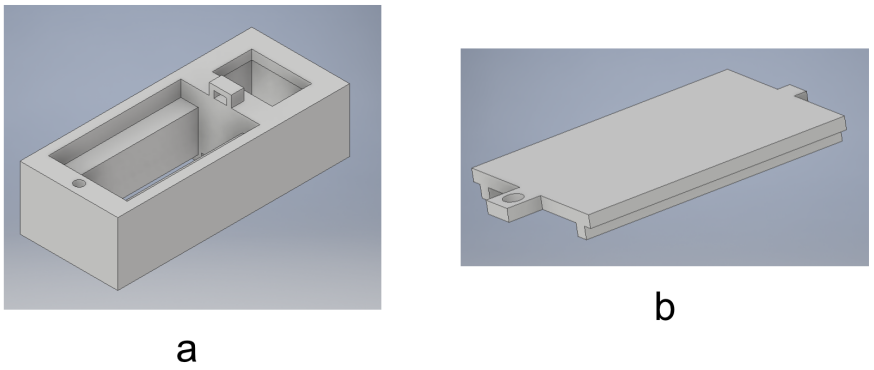

Figure 47. Light Box - Electronic Compartment

the light box. It was designed using Autodesk Inventor and featured an opening for the toggle switch to sit on and a cavity for the battery holder. In addition a cover was designed to contain the battery holder in place and shield any wirings from the user. A 3mm hole for use with a M3.5 screw was added to the side of the compartment and cover. The electronic compartment and its cover are shown in Figures 47 a and b respectively.

3.1.3 3D Printing

All of the light box parts were 3D printed using a Raise 3D N2 Plus [91] at the Undergraduate Laboratory of The University of Rhode Island. CAD parts designed on Inventor [88] were converted to .stl files and then uploaded onto the ideaMaker software [92] to prepare for printing. No significant structural, surface, etc... requirements were needed for the light box, therefore a fairly rapid print setting with decent quality was chosen. The Raise 3D N2 Plus is shown in Figure 48 and the settings used for all of the light box prints are shown in Table 2.

PLA material was used for all of the light box prints as it is a versatile bio-degradeable plastic that is very safe and easy to use. Due to limited quantities, three different spools of PLA were used in the printing of the light box. The grey was used to print the wall sleeve and electronic compartment along with its cover.

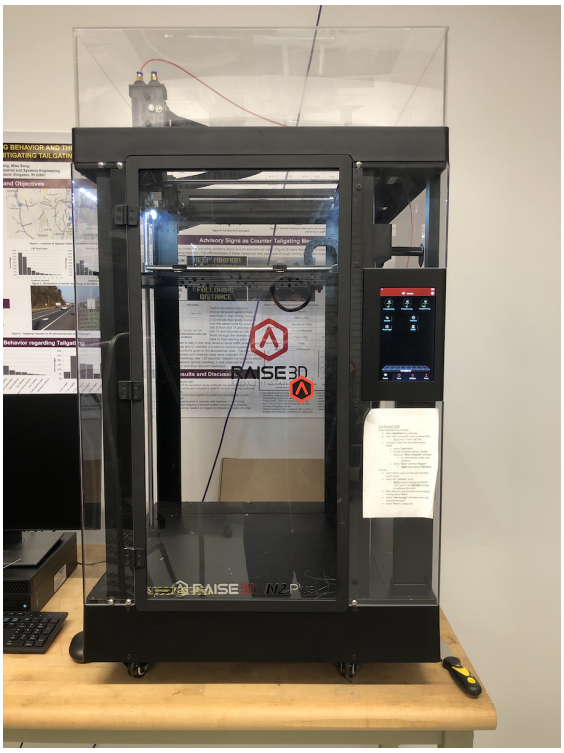

Figure 48. Raise 3D N2 Plus [91]

The gold was used to print the top cover and the bottom platform. The black was used for the diffusion filter explained in the Additional Considerations section. The specifications of the three PLA spools used are shown in Table 3.

3.1.4 Additional Considerations

Several additional considerations were taken into account to improve the quality of the light box. Diffusion panels are commonly used by photographers in lighting environments in order to avoid harsh direct lighting. These panels help create a more natural and overall pleasant light setting. A pyramid structure was created in order to incorporate the panels into the light box. The pyramid consisted of 2 sets of male and female pyramid panels. The male and female pyramid panels are shown in Figures 49 a and b respectively.

The pyramid panels were printed using the settings from Table 1 once again.

Table 2. Light Box - 3D Print Settings

Layer Height	0.1500 mm
Shells	3.0
Infill Density	30 %
Infill Speed	60.0 mm/s
Platform Additions	Raft Only
Primary Extruder Temp	205 °C
Heated Bed Temp	60 °C

Table 3. PLA Spool Specifications

Spool	Diameter	Extruder Temp. Range	Base Plate Temp. Range
Gold	1.75 mm	190 - 210 °C	30 - 50 °C
Grey	1.75 mm	180 - 210 °C	0 - 60 °C
Black	1.75 mm	195 - 230 °C	N/A

A wool fabric from Wal-mart was used for the light diffusion. The fabric was simply taped onto the pyramid panels using double-sided tape. Once all of the pyramid panels were fitted with the fabric, the pyramid was assembled by attaching the male panels to female panels in 90 degree sequence. The completed diffusion pyramid panel is shown in Figure 50.

The surface of the PLA printed parts is reflective in nature and could create lighting artifacts when taking measurements. A matte black poster was bought

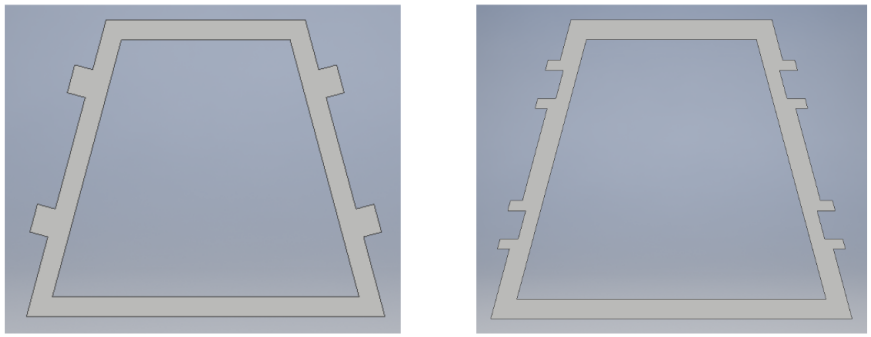

Figure 49. Male and Female Pyramid Panels

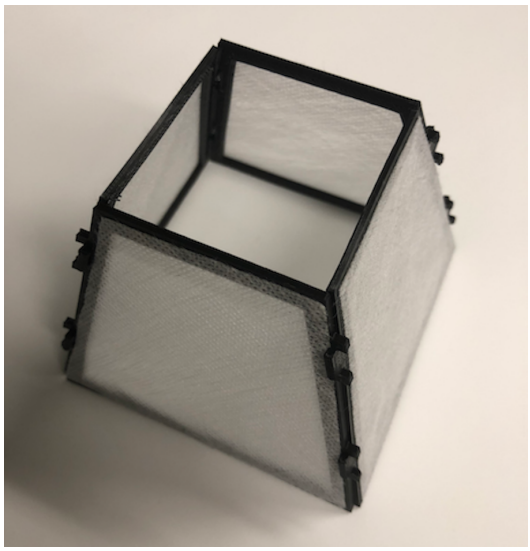

Figure 50. Diffusion Pyramid Panel

from Wal-mart to be used as a background for the inner light box components. The black poster material provides a strong contrast when taking specimen photos and impedes any reflections caused by the PLA surfaces. The bottom platform with the poster material is shown in Figure 51.

The top cover is a very general design made to allow a variety of different cameras and phones to be used. As such, outside light pollution may find its way into the box. A dark fabric was attached onto the top cover using loctite superglue so that the user could block any incoming light near the camera area. The top cover with the fabric is shown in Figure 52.

3.1.5 Assembly

The light box was assembled once all the parts were completed and ready. The LED strip was attached to the wall sleeve with the included backing tape on the back of the strip. A small hole had to be drilled on the side of the wall sleeve in order for the LED strip wiring to connect with the components in the electronic compartment. After being fitted with the toggle switch and battery holder, the electronic box was superglued onto the side of the wall sleeve. As mentioned in the

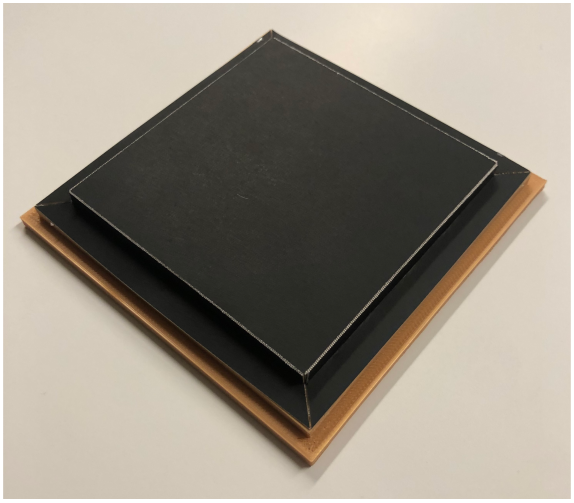

Figure 51. Bottom Platform with Poster Material

Figure 52. Top Cover with Dark Fabric

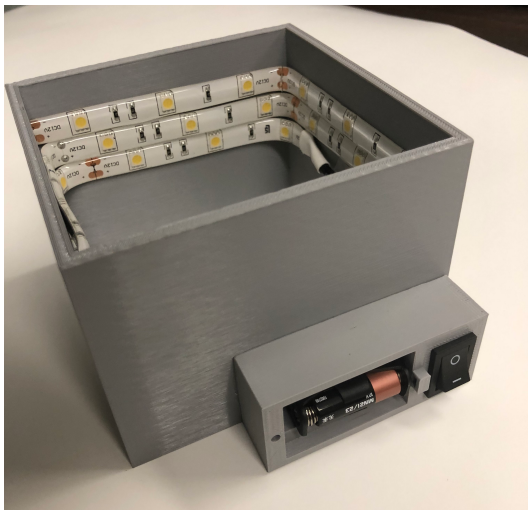

Figure 53. Light Box Electronics

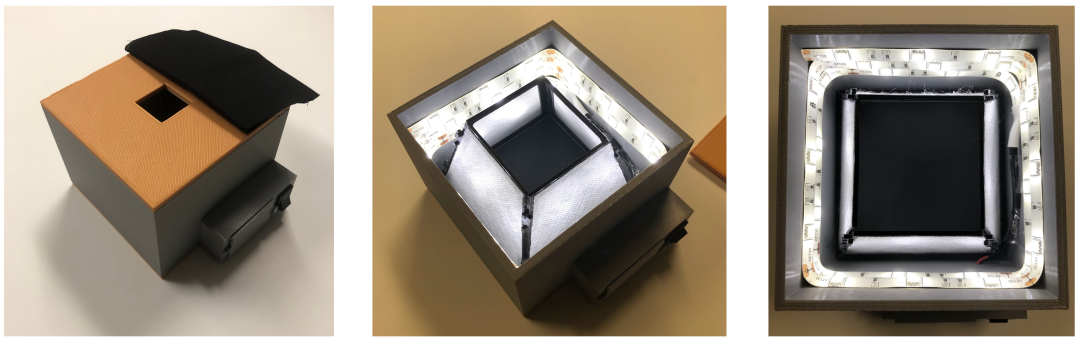

Figure 54. Completed Light Box

Lighting and Electronics Section, the hot end of the LED strip was soldered onto one of the toggle switch's terminals while the hot end of the battery holder was soldered on the other one. The grounds of the battery holder and LED strip were simply connected to one another. The wiring of the battery holder was left slightly longer than necessary to ease insertion and removal of the battery. A photo of this area of the light box is shown in Figure 53.

Once the wiring was taken care of, assembly of the box simply consisted of attaching the bottom platform, the pyramid diffusion panel, the wall sleeve, and the top cover together. The completed light box is shown in Figure 54.

3.2 Commercial Devices

There are many commercial devices available in the market today that are capable of detecting phosphate in water. These devices vary in effectiveness, usability, shelf life, and in many other factors. The currently available devices are simply not suited to detect phosphate levels in all bodies of water however. There is a need in the market for a sensitive device that is simple and applicable for field use. This section will investigate a few popular devices in order to gain a better understanding of the current market and the strengths and weaknesses of each device.

3.2.1 Indigo Instruments Phosphate Test Strip

The Phosphate Test Strips by Indigo Instruments [29] are very simple dip strip devices. These are colorimetric strips that induce a blue color on their sample pad upon contact with phosphate ions. No reagent addition or manipulation is required, which makes these strips a very convenient and attractive solution for simple phosphate measurements. The simplicity and convenience of these strips come at the cost of diminished sensitivity. The procedure for using these strips is quite simple. One must simply dip the strips in water for one second and after three minutes, compare the color on the sample pad to the supplied color chart. A dip strip is shown below in Figure 55 along with the color chart on the container.

These test strips were intended for naked eye color comparisons in order to quantify phosphate concentration levels. Tests were performed however, to see whether the image processing software ImageJ [93] could help form a calibration curve and attain an even lower limit of detection. Tests were run in triplicates format with three tests for each level of phosphate concentration: 0, 1, 2, 5, 10, 20, 50, 100, 200, and 500 ppm. Samples were made by diluting stock phosphate solution with ultra pure water. Tests were performed in accordance to the manufacturer

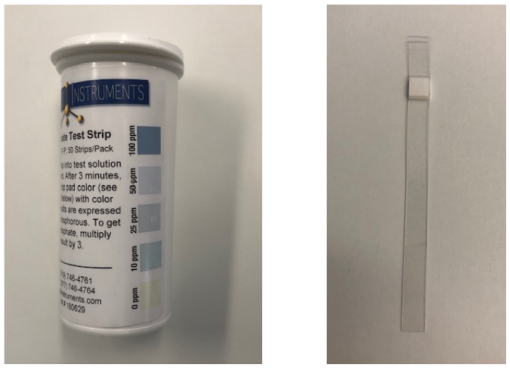

Figure 55. Indigo Phosphate Test Strips

instructions. The strips were dipped for one second and the color was analyzed after three minutes. Photos were taken using the light box with an iPhone 8. These photos were then analyzed using ImageJ for the average RGB and intensity values.

Concentration curves were made using the data obtained with ImageJ. The results are shown in the Commercial Devices Results section of the Findings chapter.

3.2.2 Quantofix Phosphate Test Kit

The Quantofix Phosphate Test Kit by Macherey-Nagel [30] utilizes dip strips along with liquid reagents. The procedure is more involved than the Indigo strips and requires the handling of dangerous chemicals by the user. This increased complexity comes with the benefit of an improved limit of detection when compared with the Indigo strips. Each kit comes with a measuring vessel, a test tube, dip strips, a bottle of nitric acid, and a bottle of PO_4^{3-} [label: -2]. The contents of the test kit are shown in Figure 56.

The official manufacturer procedure is as follows:

1. Rinse the measuring vessel with the test solution and fill it to the 5 mL mark.

2. Add 5 drops PO_4^{3-} [label: -1] (nitric acid) to the sample.

Figure 56. Quantofix Phosphate Test Kit

3. Shake carefully.

4. Place the measuring vessel on the benchtop and remove the test tube from the package.

5. Place the test tube into the cavity of the thermoformed mould.

6. Add 6 drops PO_4^{3-} [label: -2] to the test tube.

7. Insert the test strip into the sample.

8. Wait 15 seconds.

9. Shake off excess liquid.

10. Place test strip into the filled test tube.

11. Wait 15 seconds.

12. Shake off excess liquid.

13. Wait 60 seconds.

14. Compare with the color scale.

Similar to the Indigo strips, the Quantofix kit is intended to be used for naked eye color comparisons with a color scale. Tests utilizing ImageJ were once again performed in order to truly measure the device's potential performance. Tests were run in triplicates format with three tests for each level of phosphate concentration: 0, 0.1, 0.2, 0.5, 1, 2, 5, 10, 20, 50, and 100 ppm. Samples were once again made by diluting stock phosphate solution. Photos were taken in the same manner as the Indigo tests, employing the light box with an iPhone 8. Concentration curves were made from the data and are shown in the Commercial Devices Results section of the Findings chapter.

3.3 RGB App

An iPhone app was developed in order to conveniently and reliably quantify RGB measurements. The industry standard software to perform RGB measurements using a computer is ImageJ [93]. There is no ImageJ equivalent that is able to take average measurements, build histograms, and perform other imaging functions for the mobile platform however. As such the app was developed to be used in the field and in the lab as an auxiliary to test a variety of devices. In addition to general measurements, calibration curve equations can be implemented into the app to be used with specific devices. The equations can then directly measure the levels of the chemical/substance in question based on the RGB measurements. The app also features a data log that records time, temperature, humidity, etc... every time a measurement is taken. This data log can work in conjunction with the online data center detailed in the next section which provides a great way to store data from various users and locations. The app is a standalone work in its own right and may be used in various applications beyond the scope of phosphate detection. The methodology used in the construction of this app is detailed below.

3.3.1 App Structure

The app was built using Swift [94] and Xcode 10 [95]. Xcode 10 is an integrated development environment (IDE) for macOS while Swift is a general-purpose programming language developed by Apple. The app could only be built for Apple's iOS and macOS ecosystem using these tools. An android version could easily be built however by coding in Java using the same principles detailed in this section. CocoaPods [96] was also used as a dependency manager for the project. External libraries that helped ease some app functionalities were easily integrated into the app using CocoaPods. This section will detail the overall structure of the app and its components.

The Model-View-Controller (MVC) architecture was used during development of the app. MVC is a very popular and easy to use software architecture recommended by Apple. MVC is made up of three layers: the Model, the View, and the Controller. The Model is where the data reside and are managed. The logic of the application is also handled in the Model layer. The View handles the visual aspects of the app and outputs information. What the user actually sees is developed in the View layer. The Controller mediates between the Model and the View. The Controller accepts input and converts it to commands that may be passed to the Model and/or the View. A diagram of the MVC architecture is shown in Figure 57.

There are many advantages to using the MVC architecture. It allows simultaneous development for the different components or layers of the app. Modifications are easily implemented due to the separated nature of tasks. Lastly, because components are independent of one another, developers are able to reuse code for similar purposes in other applications. The MVC architecture does comes with its share of disadvantages however as it brings increased complexity to an application.

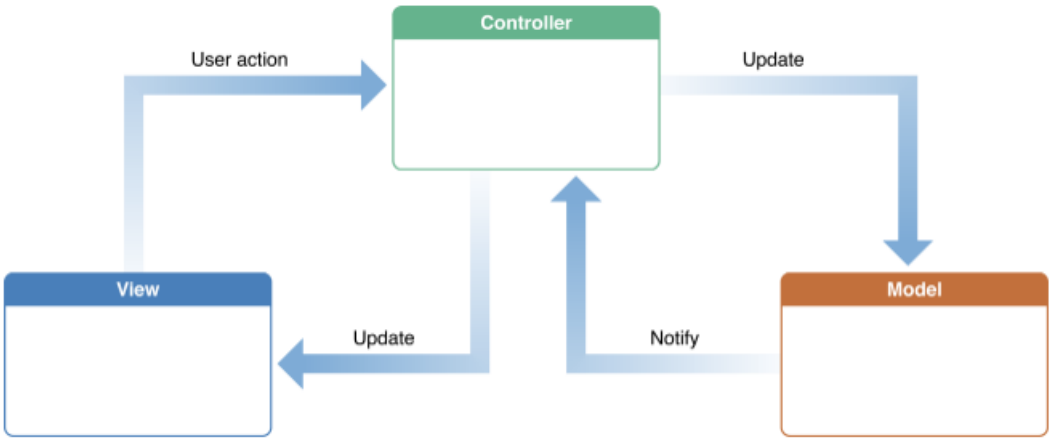

Figure 57. Model-View-Controller (MVC) Architecture

The application was split into six main groups. Three of those groups are the MVC layers. The other three are Services, Chemistry, and Extensions. Data and network services such as retrieving weather data through an API are handled in the Services group. The Chemistry group contains files related to calibration curve equations explained in the Chemical Modes section. The Extensions group is responsible for the imaging functions used to obtain RGB measurements. External libraries were imported using CocoaPods and are present in the Pods group of the project. Three external libraries were used to help app functionality. Alamofire [97] aided in HTTP networking and API requests. SwiftyJSON [98] was used to easily handle JSON (JavaScript Object Notation) formatted files. Histograms explained in the Advanced Statistics section were created using the Charts library by Daniel Gindi [99].

The project navigator in Xcode showcasing the various groups and overall structure of the application is shown in Figure 58.

3.3.2 Camera and View Setup

The main app view consists of a camera view being fed from the back camera of the phone along with a measurements section in the bottom of the view. Photos

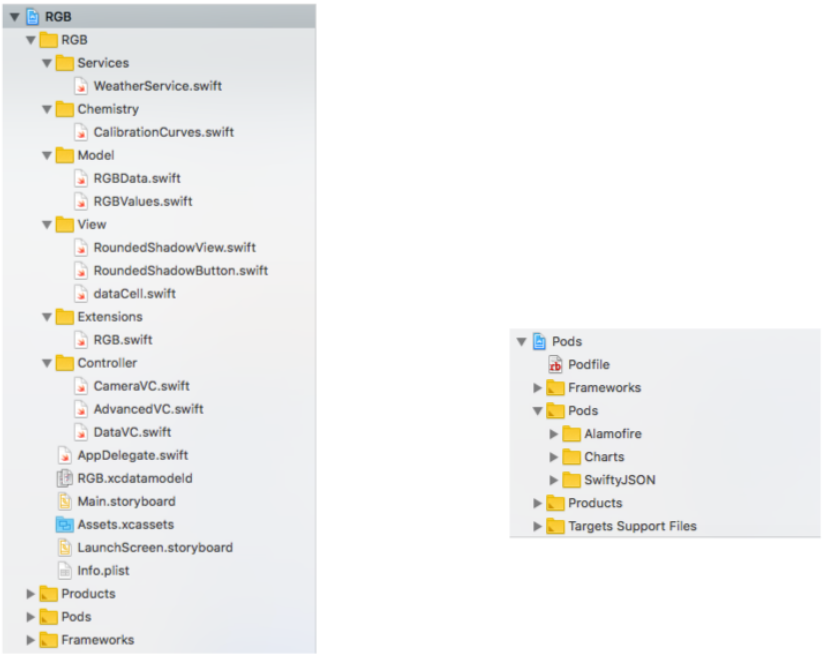

Figure 58. RGB App - Project Navigator

and subsequently measurements are taken by simply touching the view. A still image is taken from the view and passed onto a hidden image layer where imaging functions can be applied to take RGB measurements. Once an image is taken, the bottom measurements section expands upwards with recorded values and a view of the analysis region used. The functions used to perform analyses are explained in the RGB functions section. Figure 59 shows a screenshot of the main app view with its various components.

As shown in Figure 59, there are various buttons present in the app's main view. There is a mode selector in the top left of the screen used to switch chemistries that is explained in the Chemical Modes section. The three buttons on the top right include a shape selector explained in the RGB Functions section, a flash button to turn on/off the camera flash, and a data log button that will be explained in the Data Log section. The bottom section includes the various measurements made, a view of the analysis region, and an advanced stats button

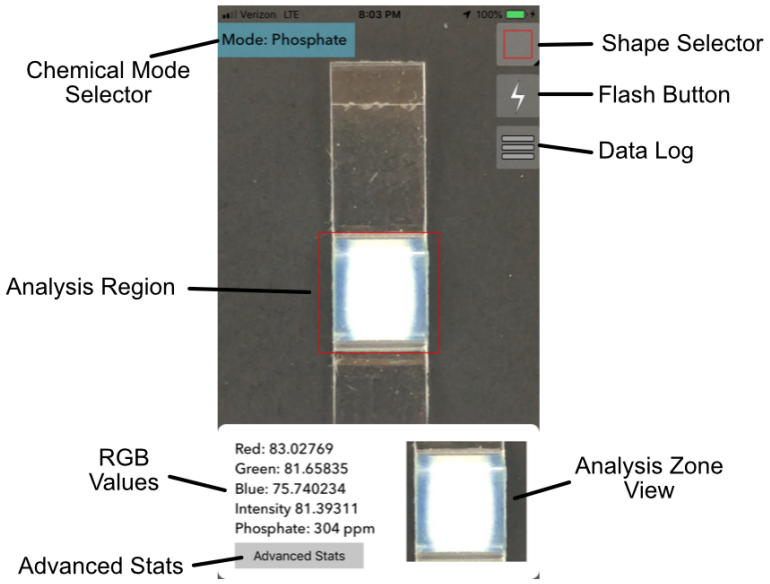

Figure 59. RGB App - Main View

explained the Advanced Statistics section.

Users can zoom in and out by pinching the main view. Camera focus is set on continuous auto focus mode to simplify user operation. As explained a still image is taken once the view is touched. A data file representation of the photo is then created and passed onto the image view. The image view recreates the photo so that imaging functions can be applied. In addition the photo is cropped around the analysis region and sent to the measurements section for a better view. This sequence of events occur every time the view is touched.

3.3.3 Exposure Control and White Balance

As explained in the Camera and Detection Technology section of the Literature Review, controlling the exposure and white balance is of utmost importance for scientific measurements. The iPhone camera's aperture, shutter speed, ISO, and white balance are all available for adjustment in Xcode. The four settings were all set manually, locked, and configured to work in conjunction with the light box. The focus was left in the continuous auto focus mode however, in order to

accommodate different types of tests in the light box with different lens-to-device distances.

The first setting configured was the white balance. The white balance was adjusted to a neutral setting using the lighting environment of the light box. This was done using the RGB gains on the setWhiteBalanceModeLocked function of the camera. The gains were set to: Red - 2.0, Green - 1.0, and Blue - 2.0. This gains setting was adjusted specifically to be used with the light box. As such, the app as it stands is meant to be used in conjunction with the box for readings. The setting was set to locked post adjustment and will not change regardless of the lighting environment.

Exposure was controlled with the setExposureModeCustom function of the camera. This function takes in two values: one for duration (shutter speed) and another for the ISO. These were also set to fixed values. The exposure duration was set to the default camera setting of 1/30th of a second. The ISO was set to a value of 80. Once again these settings were adjusted to correspond to a neutral light setting in the light box. The settings were locked post adjustment so that the phone camera could not alter exposure settings even when used with different lighting.

Configuring these settings allows the app to take objective and quantifiable scientific measurements. While the app performs quite well in different lighting environments with these settings, the built-in calibration curves, explained in the Chemical Modes section, will not work properly unless used with the light box. This of course poses a problem for commercial viability. The simple answer is integrating a calibration procedure for the camera into the app. This is explained in greater detail in the Conclusion chapter as it is beyond the scope of the thesis and should be considered as future work.

Figure 60. RGB App - Shape Selector

3.3.4 RGB Functions

The RGB functions are the core of the application as they are used to perform the measurements needed to colorimetrically quantify chemical levels. A red analysis region is present in the main view of the app with two available shapes. A square and a circle were chosen as the two shape options as they are the most common and useful shapes for analysis. Both shapes have fixed dimensions of 140 px x 140 px and 140 px dia. respectively. The shape used can be easily changed by pressing the shape selector and choosing the desired shape. A close up view of the shape selector is shown in Figure 60.

Each shape has its own respective function to perform RGB measurements. The functions are stored in the RGB file of the extensions group. These functions are an extension of the Swift object UIImage. UIImages are how images are represented in a Swift application and also the objects used in the image view of the app. Because the RGB functions are an extension of UIImage, the functions can simply be called on UIImage objects. Both functions take a UILabel as an argument and essentially perform the same commands initially. First the entire image is taken as data. Then R, G, and B Float variables are initialized. Finally

the origin, width, and height of the analysis region is calculated from the UILabel passed into the function. From here the functions differ due to their respective shapes.

The square shape function iterates from left to right and downward through every pixel inside the analysis region. The pixel info of every pixel is taken one at a time and the RGB values are added to the respective R, G, and B variables. After iterating through every pixel, the average R, G, and B values are found by dividing the total number of pixels from each respective measurement. An RGBValues struct was created to easily store and manage these values in the application. The struct consists of 7 values: the R, G, and B values along with histograms for the RGB values and Intensity. These histograms are explained further in the Advanced Statistics section.

The circle shape function performs in an analogous manner to the square shape function except for the iteration method. The first iterator in the circle function is for the vertical position of the circe. The second iterator is a function of the first iterator that determines how many pixels should be evaluated left and right from the center of the view. The circle function then measures and stores each pixel value using the same approach that the square function used. Once the functions are executed and the RGB values stored, the values are passed onto a UILabel in the measurements section for the user to view. The label includes the RGB values along with the intensity and chemical levels. The intensity is found using the standard grayscale equation shown in Equation 6. The chemistry level is calculated using the calibration curve equations explained in the next section.

$$I = 0.299R + 0.587G + 0.114B$$

Equation 6

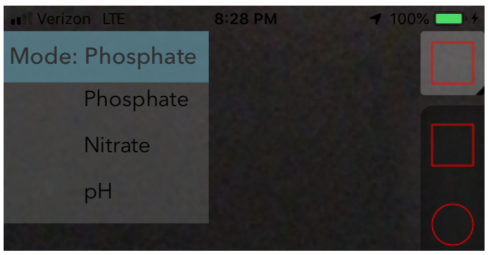

Figure 61. RGB App - Chemical Mode Selector

3.3.5 Chemical Modes

Chemical modes were added to the application for direct measurement of chemical levels. Three chemical modes were added to the app to illustrate the concept. Modes can be selected by pressing the mode selection button on the top left of the main view. A close up of the mode selection button is shown below in Figure 61. As shown the three modes added were Phosphate, Nitrate, and pH. Phosphate was added as it is the focus of this thesis of course. Nitrate is a similar nutrient that plays a similar role in water and is currently being investigated in the URI Microfluidics Laboratory. pH was added as a placeholder example for future chemicals.

An enumeration was used to handle the chemical modes. This enumeration included the three modes as cases and was used as a global object. Each time the mode is changed using the mode selection button, the enumeration state changes and the respective calibration curve equations to be used also change. The calibration curve equations are functions in the CalibrationCurves file in the Chemistry group. These functions take in RGB values as parameters and output chemical levels based on calibration curve equations specific to devices. Once a device curve is known it can be very easily integrated into the app for quick and easy measurement. Dummy equations were entered into the functions in order to test the concept. The functions are called every time an analysis is performed and the outputs are passed onto the bottom measurements section of the view. A close up

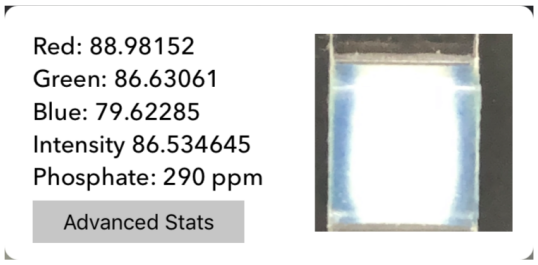

Figure 62. RGB App - Measurements Section

view of the measurements section showcasing the RGB and chemical level values is shown in Figure 62.

Using calibration curves directly in an application can simplify user operation significantly. In addition, better sensitivity and precision can be achieved with this method. While many commercial devices employ color charts that give approximate measurements at best, this app provides a more scientific approach to quantification. Field work can be greatly enhanced with the chemical modes of this application.

3.3.6 Advanced Statistics

An advanced statistics section was also created in the app. This section contains histograms of the RGB combined values, RGB individual values, and Intensity values. In addition, statistics for each histogram is given. The statistics includes the mean, median, standard deviation, count, minimum, and maximum. Values for the histograms are calculated in the RGB functions. Float lists are initiated when the RGB functions are called and populated with pixel values during iteration. These lists containing RGB and intensity values are then stored in the RGBValues struct passed onto the measurements section.

The histograms are created using the values in the lists of the RGBValues struct. These values are passed onto a chart function in the AdvancedVC file of the controller group. This chart transforms the values into a data format suitable to

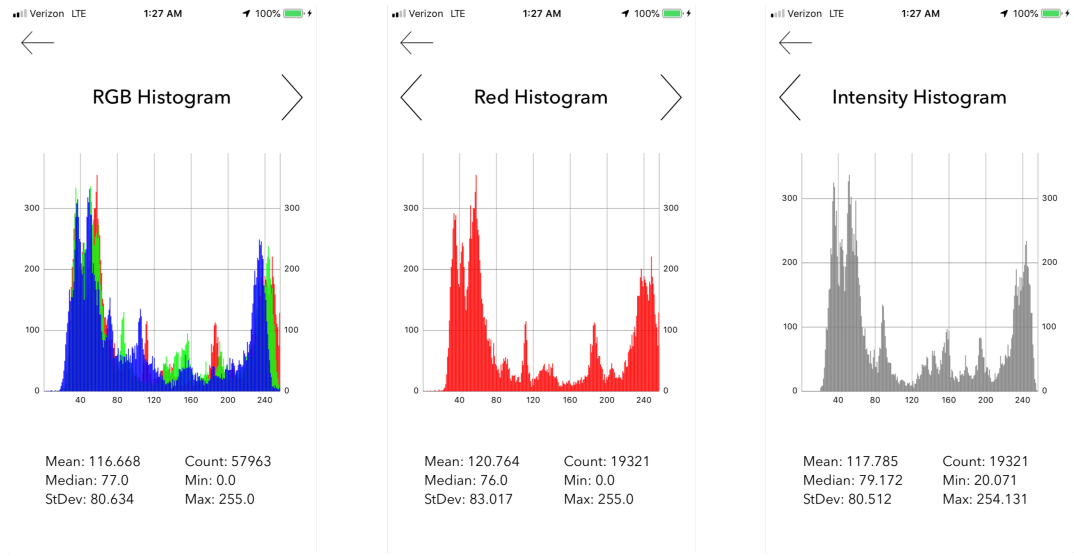

Figure 63. RGB App - Histograms

be used with the imported Charts library by Daniel Gindi [99]. The barChartView function of the Charts library is then used to create the various histograms. The statistics are simply calculated from the original value populated lists. The user could easily access the histograms by pressing the Advanced Stats button in the measurements section of the view. Once in the new view, left and right arrows are used to navigate between the various histograms. Figure 63 showcases the RGB combined, Red, and Intensity histograms created during analysis of a test run.

3.3.7 Data Log

A data log was integrated into the app in order to track measurements along with environmental data. The data log could be accessed from the main view by pressing the data log button on the top right of the screen shown in Figure 53. A table is present in the data log view with information on all of the measurements recently taken. Five fields are present for each measurement: time and date, GPS location, chemical level, temperature, and humidity. The data log view is shown in Figure 64 and the various components in a measurement data cell are detailed

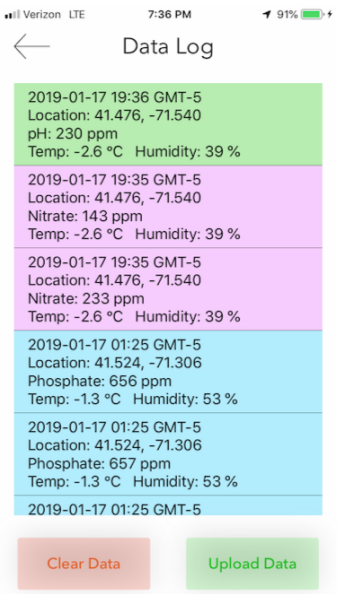

Figure 64. RGB App - Data Log View

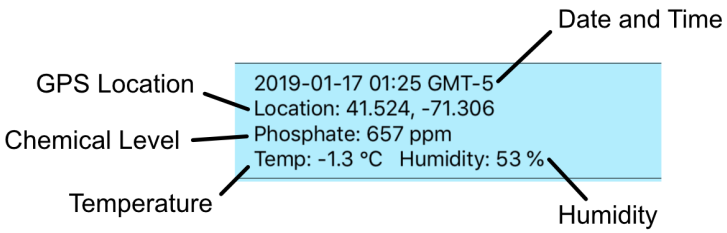

Figure 65. Measurement Data Cell

in Figure 65.

The data log was created using Apple's Core Data framework. Core Data is used to easily manage data objects and persistence. Using Core Data can drastically decrease the amount of code being written in the model layer of the MVC structure. The Core Data model in the app featured 6 attributes: chemical, concentration, date, humidity, location, and temperature. All attributes are of datatype String except for the concentration and date which are Integer 32 and Date types respectively. Every time a measurement is taken, values are passed onto the Core Data model. The values are then appended to lists in the DataVC file of the Controller group. Lastly, the table in the data log view is populated with measurement

values from these lists.

The date field displays the current date and time along with the timezone difference with respect to Greenwich Mean Time (GMT). The date has a year-month-day format and the time shows the hour and minutes. The date and time is retrieved from the phone with built-in functions in Swift. The location field displays the latitude and longitude of where a measurement was taken. Swift's location manager was used to retrieve GPS locations. In order to use the location manager, the user must enable location services for the app upon first use. A user could enable or disable location services on the phone settings at a later time as well. Once location services is enabled, the app retrieves the GPS location of the phone to the nearest ten meters. The location is constantly updating during operation off the app but is only retrieved when measurements are taken.

The chemical level field shows the level of the measurement taken along with the respective chemical. This is simply passed onto the Core Data model when populating the measurements section of the main view. The measurement cells are also color coded based on which chemical modes were used for the measurements. The temperature and humidity fields show the temperature in degrees Celsius and humidity as a percentage. These values are retrieved using the OpenWeatherMap API [100]. Communication with the API is handled using AlamoFire in the WeatherService file of the Services group. Requests are sent to the API using a url with the latitude and longitude coordinates of the phone. Therefore weather data could only be retrieved when location services is enabled for the application. The API returns a response with weather information in JSON format. The JSON response is parsed for temperature and humidity data using the SwiftyJSON library. API requests are sent every 2 minutes in the background as changes in weather take time to unfold. Global variables for temperature and humidity are updated with

every request and retrieved each time a measurement is taken.

The data log also interfaces with the online data center detailed in the next section. There are two buttons at the bottom of the data log view, one to clear data and one to upload data. The clear data button simply clears the measurements data currently populated in the data log table. The upload data button is used to upload data to the online data center where further insights can be drawn.

3.4 Online Data Center

An online data center was created to interface with the data log of the RGB app. The data center features uploaded measurements from users with time, location, weather, and chemical concentration data. A map page is also present with pin locations of all measurements. This system can be used to better monitor nutrient levels in water where all the data collected can be easily accessed from one server. The sections below detail the construction of the data center along with its various pages.

3.4.1 Construction

The data center was developed using Flask [101] for the back-end (server-side) and standard HTML/CSS with Bootstrap [102] for the front-end (client-side). Flask is a microframework for python based on Werkzeug and Jinja 2 while Bootstrap is a popular HTML, CSS, and Javascript framework. The actual database used to store user uploaded data was created using Firebase. Firebase is a back-end service from Google that significantly simplifies the data storage process. Essentially, data stored in the RGB app using Core Data is uploaded and stored in an online Firebase database. The data center simply retrieves the stored data from Firebase and displays it in the web.

The project file structure is shown in Figure 66. As shown, the project consists

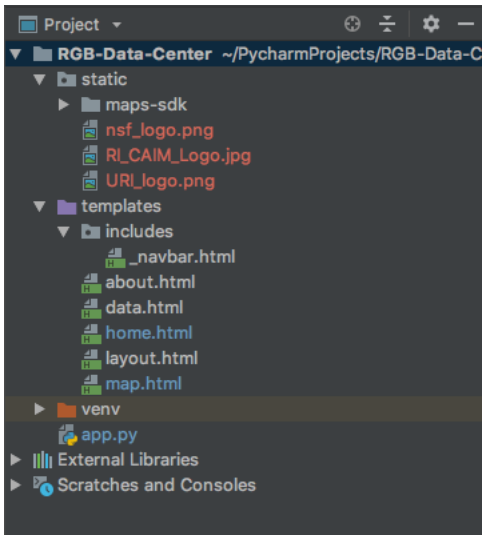

Figure 66. Online Data Center - Project File Structure

of a main back end python script (app.py) along with templates and static assets. The templates contain html files that are rendered in the user's browser. Images and API files are stored in the static assets group. The main script, app.py, is called when the website is first loaded. The data stored in the Firebase database is retrieved and stored in a local list as soon as app.py is executed. The list can then be easily manipulated to be presented in varying formats.

The data center features four pages: home, data, map, and about. These can be easily accessed from the navigation bar at the top of the site. Home includes a short intro to welcome the user to the site. The data is presented in table format in the data page. The map page features measurements with pin locations on a map. A brief description of the data center along with the overarching work is given in the about page. The home and about pages are shown in Figures 67 and 68.

3.4.2 Data

The data page is the heart of the data center. It essentially features a table with all of the uploaded measurements data. This table was created with Boot-

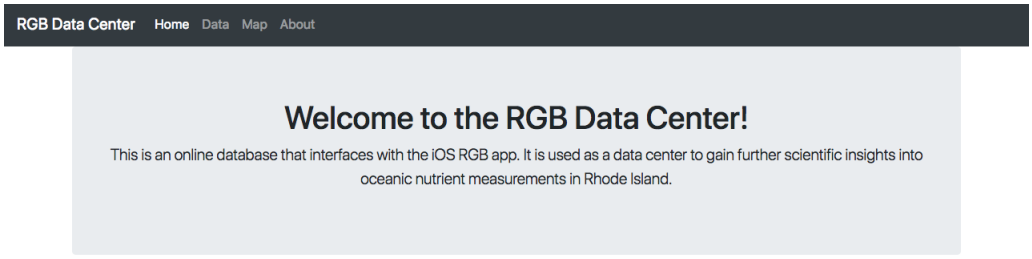

Figure 67. Online Data Center - Home Page

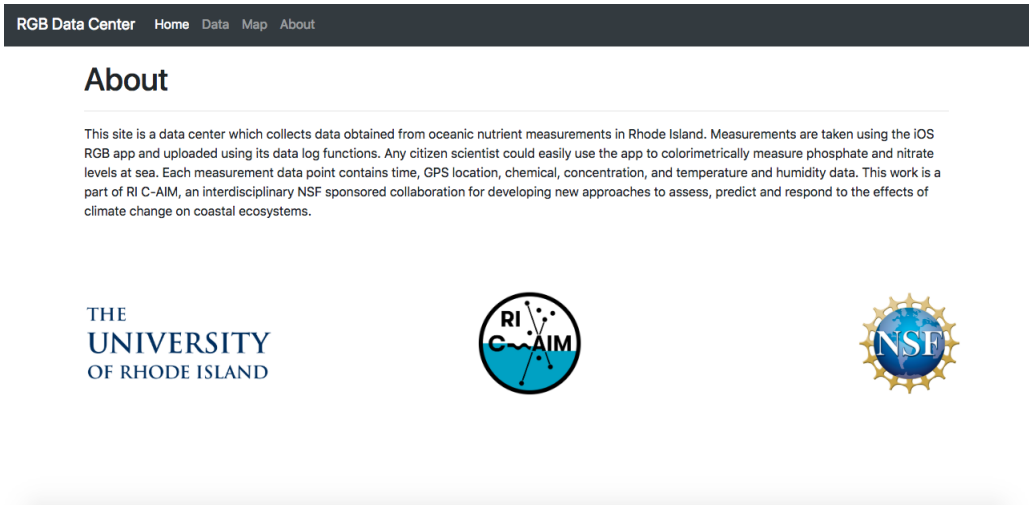

Figure 68. Online Data Center - About Page

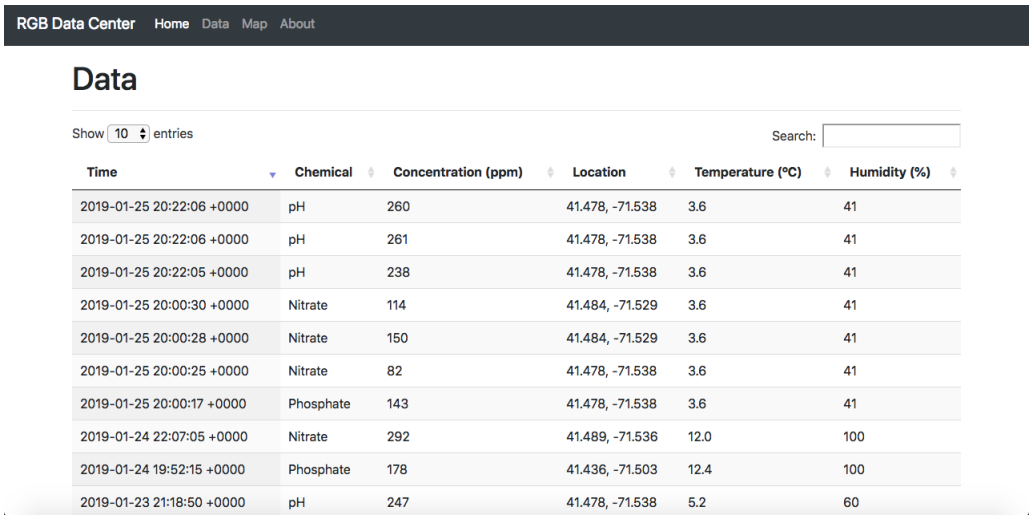

Figure 69. Online Data Center - Data Page

strap's responsive table class. Like the RGB app data log, the table has time, chemical, concentration, location, temperature, and humidity data. The table is fully responsive so users can sort by different features (e.g. time or temperature) and choose how many entries to view per page. Searching for and/or filtering results is also possible by utilizing the search bar on the top right corner. Users can easily constrain the table to only display results from a certain date or certain location for example. The data page is shown in Figure 69.

3.4.3 Map

The map page can be very useful to gain insights on the state of nutrient levels by geographic location. The map was produced with the help of the TomTom Maps API. The Maps API was used to render the map on the page and add pins with data based on GPS coordinates. Narragansett Bay, RI is the default map area upon loading of the page but users can move, zoom, and interact with the map area. Data taken from the Firebase Database is parsed for GPS coordinates and used to create markers on the map with measurement info. The map page is shown in Figure 70.

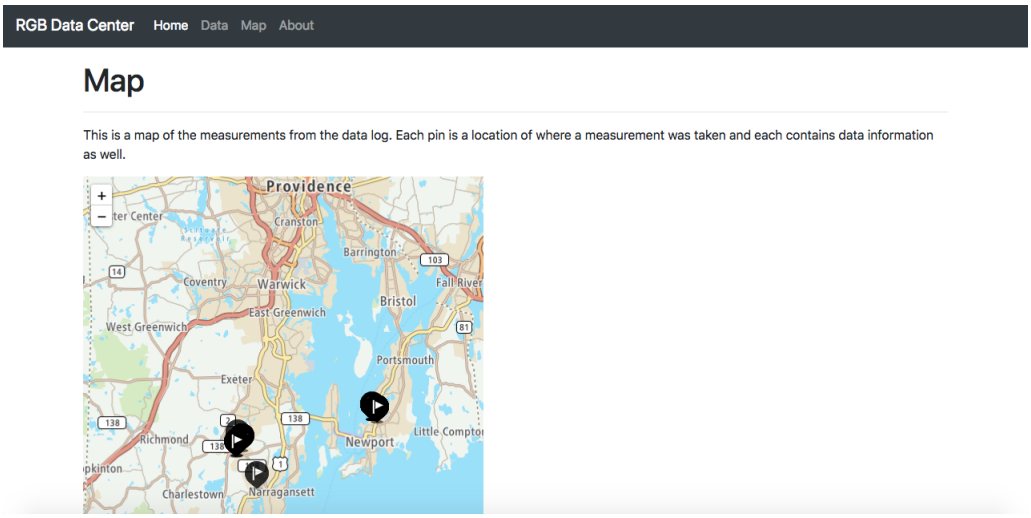

Figure 70. Online Data Center - Map Page

The current map concept can be even further extended once a sizable amount of data is amassed. The bay can be discretized into smaller regions and data gathered at sea could be used to produce heat maps of average nutrient concentration levels. A visualization of this kind would be of great value to both scientists and citizens alike.

3.5 Lab-on-Paper Devices

The design cycle for a phosphate detection device began with paper-based microfluidic devices. Several iterations were developed before the final product detailed in the next section was achieved. Every device was built in conjunction with Mindy Levine's chemistry team at the University of Rhode Island. The molybdenum blue method [23] explained in the colorimetric methods section of the Literature Review was chosen for the chemistry. This method has the potential to achieve high sensitivity and is the standard chemistry used in the lab. All devices were built to incorporate this chemistry. Many techniques and insights on the phosphate detection problem were gained with every design iteration and are discussed in this section.

3.5.1 General Fabrication Methodology

A general methodology was followed for the fabrication of every paper-based device. Whatman Grade 41 filter paper was used for every device as it has been used extensively in the Microfluidics Laboratory at the University of Rhode Island. Device layers were designed using the vector graphic design programs Corel Draw [103] and Affinity Designer [104]. A Xerox ColorQube 8570 with Xerox Genuine Solid Ink Black was used to wax print designs onto the filter paper. Non-printed areas become hydrophilic channels, ports, and features while printed wax areas create hydrophobic barriers. Papers then had to be heated in an oven for the wax to melt and distribute to the backside of the paper. All papers were heated for 60 seconds at 120 °C using an Isotemp Model 280A vacuum oven from Fisher Scientific. This step is absolutely essential so that proper and effective hydrophobic barriers are created with the wax on the paper.

Layers were then cut using an Epilog Engraver mini laser cutter. The laser cutter is able to make very precise cuts from designs built using vector graphic software. Devices can finally be assembled once all layers are printed, heated, and cut. Layers are attached to each other using double sided tape. Designs have to be cut onto the double sided tape using the laser cutter in order to allow contact between layers at certain channel locations. An outer tape layer is also attached to the front and/or back of some devices in order to ensure that fluid flows through the paper instead of over the paper. The Xerox ColorQube 8570, Isotemp vacuum oven, and Epilog Engraver mini used in the fabrication of all paper-based devices are shown in Figures 71 a, b, and c respectively.

3.5.2 Alyltrichlorosilane Device

The first design iteration incorporated alyltrichlorosilane valves developed by Chen et al. [32]. The molybdenum blue chemistry employed two reagents in its

a b c

Figure 71. Xerox ColorQube, Vacuum Oven, and Epilog Engraver

method: a molybdate complex and ascorbic acid. These two reagents must simply mix with the water sample in order to produce a colorimetric response. The alyltrichlorosilane valves were used to hold the two reagents until sample flowed underneath them. Areas directly underneath the valves are spotted with Tween 20 surfactant. This surfactant effectively opens the valves once fluid comes into contact with it. These are one-way valves essentially that could only be opened from the bottom.

Creating the alyltrichlorosilane valves is a fairly involved process. A vapor chamber made from a Tupperware box with entry holes on top was used. The vapor chamber is shown below in Figure 72. This box contained a tin foil base to place layers on. There are eight holes on top that are covered with tape. Directly underneath the holes is a cloth used to absorb some of the alyltrichlorosilane chemical. Device layers adopting the valves are placed inside the Tupperware box. The box is sealed and the tapes covering the holes are taken off. Alyltrichlorosilane is pipetted into the box through the holes one by one and each hole is covered with the tapes once again. The chemical quickly turns into vapor inside the box and is deposited onto the exposed areas of the device layers. The process takes around 12 hours to complete. Only then can the layers be retrieved and used to assemble

Figure 72. Alyltrichlorosilane Vapor Chamber

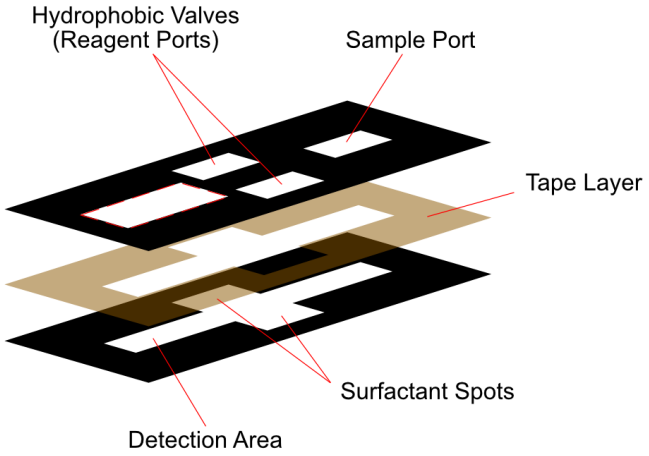

Figure 73. Alyltrichlorosilane Device - Iteration 1

a complete device.

This first design iteration is shown below in Figure 73. As shown, this is a two layer design with ports on top and channels underneath. The top layer features a sample port and two alyltrichlorosilane valves that serve as reagent ports. The bottom layer is a cross-shaped channel that is spotted with surfactant directly underneath the valves. The lower part of this channel also serves as the detection zone where the colorimetric response is observed. Device operation is quite simple as the water sample is simply pipetted onto the sample port once the reagent ports are filled. The water sample travels down to the channel layer, opens the two valves from underneath and then all the fluids meet and mix at the detection zone.

This device was tested using 15 μg for each reagent and 20 μg of 1000 ppm

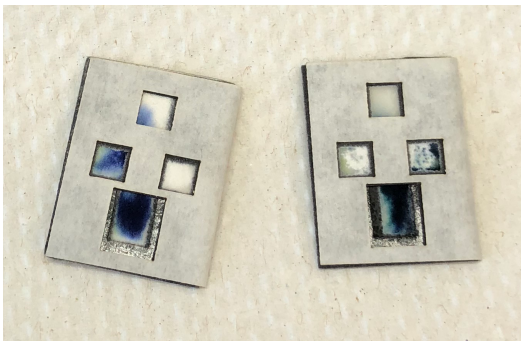

Figure 74. Alyltrichlorosilane Device - Iteration 1 Results

phosphate diluted in water. The results are shown below in Figure 74. The device did not perform very well as shown. A colorimetric response was observed in many areas outside the detection zone. The detection zone itself did not have very uniform color formation as well.

A second iteration utilizing the Alyltrichlorosilane valve was made. This iteration was also a two layer paper-based device. The change in this iteration was that only one reagent port was present as the ascorbic acid was pre-spotted in the detection zone. This was done to simplify device operation and potentially promote better mixing of the fluids. The device is shown in Figure 75. Device operation is similar to the first iteration except that only the molybdate complex needs to pipetted onto a reagent port.

Results were once again unsatisfactory. False positives were achieved when testing with water samples containing no phosphate. This was of course a major issue. It was found that this occurred due to the chemistry of the alyltrichlorosilane valves. These valves contain silicon in the chemistry which as mentioned by Drummond and Maher [41], can cause some interference in the molybdenum blue reaction. The valves were therefore deemed inadequate and new approaches had to be explored.

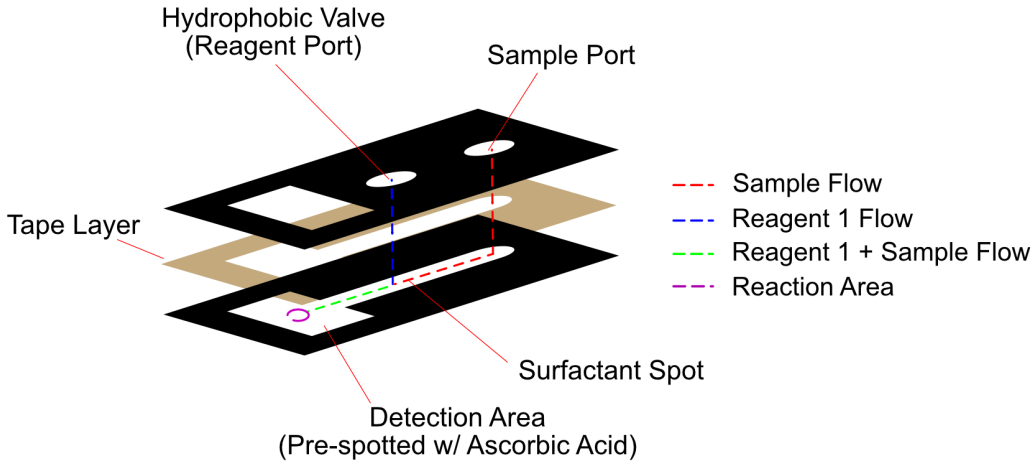

Figure 75. Alyltrichlorosilane Device - Iteration 2

3.5.3 Wax Device

The next stage of the design cycle involved utilizing wax valves on a paper-based device. The design was very similar to the second alyltrichlorosilane device iteration. The detection zone was pre-spotted with ascorbic acid while one reagent port incorporated the wax valve for the molybdate complex. A schematic of this device is shown in Figure 76. As shown, the valve is now placed behind the sample port. This is done due to the mechanics the wax valve. These valves are a novel fluid control technique developed in the Microfluidics Laboratory at the University of Rhode Island by Wayne Smith.

Creation of the wax valves required a very precise methodology. Special thin wax layers are printed onto the valve areas. These thin layers utilize low CMYK (Cyan, Magenta, Yellow, and Black) settings that result in less ink being deposited onto the paper. The layers with valves then need to be heated in a precise fashion to ensure a uniform wax distribution. A tray is used to support the edges of the papers in the oven so that only convection is responsible for melting the wax. This ensures that no uneven regions are formed from conduction. The layers are first

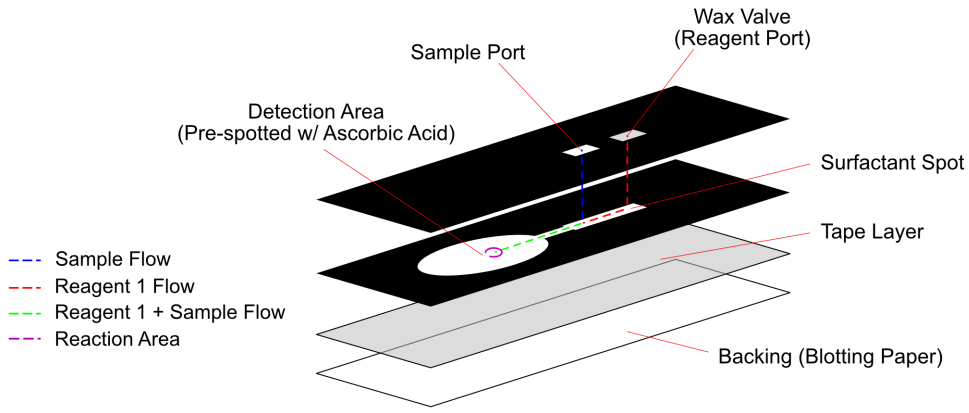

Figure 76. Wax Device

heated top side up for 20 seconds, then bottom side up for 30 seconds, and then top side up for 40 seconds. These three heating steps are all done at 120 °C. The oven setup used is shown in Figure 77 and the heating process is shown in Figure 78.

The valve works on the principle that its barrier is fairly weak and can be disrupted by fluidics in the channel layer underneath. Similar to the alyltrichlorosilane valves, the wax valves open when fluid reaches the area beneath them. The fluid below creates hydrostatic pressure underneath the valve and the saturated underside of the valve becomes weak. A minuscule fluid bridge is eventually formed which essentially opens the valve and releases the reagent on top.

Assembly of the layers is slightly different than the alyltrichlorosilane device. There are two filter paper layers, one tape layer, and one blotting paper layer. The two filter paper layers are stacked on top of each other while the bottom layer is attached to the blotting paper backing with the tape layer. The blotting paper is used as a backing card to add some rigidity and robustness to the device. All layers are then fully attached by the use of staples. These staples are placed at the edges of the device and near the wax valve. The staples ensure good contact

Figure 77. Wax Device - Oven Setup

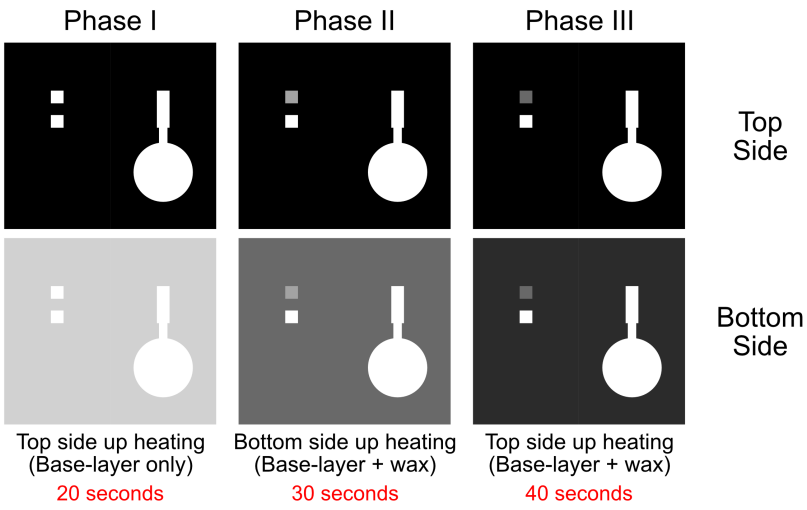

Figure 78. Wax Device - Heating Process

Figure 79. Wax Device - Fluidic Results

between layers which is absolutely crucial for the functionality of the wax valve.

The wax device showed good fluidic results when tested with colored water. The results are shown in Figure 79. Red fluid was used for the water sample and green for the 'reagent' sample on the valve. As shown the valve functions properly as the green fluid makes its way to the detection zone. This concept was not without issues however as the opening of the valves took a significant amount of time. The opening time was around 4 to 5 minutes from the time the sample reached the area beneath the valve. This is due to the fact that only part of the valve needs to open for fluid to pass which results in a fairly slow flow rate. The chemistry team also discovered that trace amounts of phosphate are inherently present in the Whatman Grade 41 filter paper which can significantly impact the desired colorimetric response. New approaches had to be developed which resulted in a hybrid LOC/LOP device detailed in the next section.

3.6 Lab-on-Chip Device

The lab-on-chip device was built in conjunction with Mindy Levine's chemistry team at the University of Rhode Island. The device is a hybrid as it also employs filter paper as the flow medium. The main emphasis of the device was to build a system that is both commercially viable and able to perform better than current commercial devices. Performance in this case is measured by the device sensitivity where a lower limit of detection is superior. The methodology that went into

creating the lab-on-chip device is detailed below.

3.6.1 Prototype Design

The initial prototype design of the lab-on-chip device consisted of a simple reagent activation system with a paper based section for the reaction to take place. This design was built to better understand the problem at hand and to develop any alterations if necessary. The first modification when compared to the lab-on-paper devices was of course the storage of reagents in the device. Storage was achieved by the use of small bubble wrap containers, a method developed by the Whitesides group at Harvard [58]. Two bubble wrap containers were used for each device, one for the molybdenum complex and another for the ascorbic acid. The reagents were simply injected into the bubbles using a syringe. Clear nail polish was then used to seal the bubbles.

A prototype housing was built to store the bubble wrap containers and employ a reagent activation system that could deliver the reagents onto the paper-based section. This was achieved by the use of a button mechanism. The reagent containers sit on top of chambers in the housing below a button mechanism. Metal thumb tacks were placed onto the bottom of each chamber so that both bubbles are pierced as the button is pressed. The main housing body and button mechanism are shown in Figure 80.

The role of the paper-based section is to simply mix the two reagents into a detection zone. Water is then pipetted onto the detection zone and a colorimetric response is induced. Several mixer designs were tested with colored water and a simple serpentine design was shown to be more than satisfactory. Glass fiber conjugate pads from Millipore were used. Designs were made on CorelDraw and cut using the Epilog Engraver laser cutter. The design overlaid onto a device is shown in Figure 81. As shown, there is a 12 x 12 mm detection zone on top,

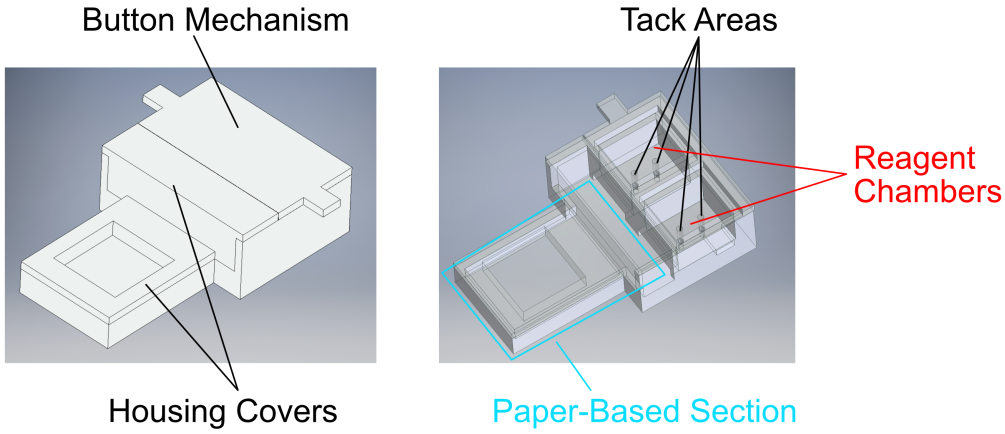

Figure 80. Initial Prototype - Body

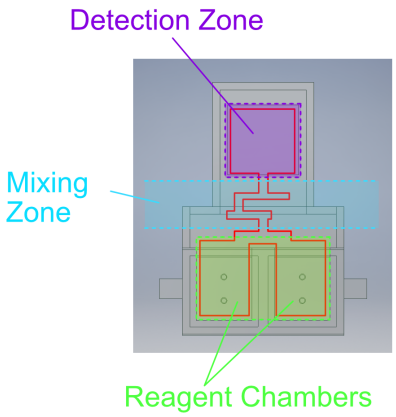

Figure 81. Initial Prototype - Paper-Based Section

a mixing zone in the middle, and two bottom sections for wicking the reagents. The bottom sections are placed inside each reagent chamber and pierced with the thumb tacks.

The main housing body, button mechanism, thumb tacks, and paper-based section make up the overall architecture of the prototype device. A photo of this assembled device is shown in Figure 82.

Figure 82. Initial Prototype - Assembled Device

3.6.2 Issues

A number of issues with the prototype design were revealed during testing. A major problem was the use of thumb tacks. It was shown in testing that the thumb tacks react immediately with the molybdenum complex due to the interaction of the reagent with metal. The thumb tacks were subsequently replaced with the tips of plastic floss picks. Small sections on the picks were cut and superglued onto the reagent chambers. While not as rigid as the metal thumb tacks, the picks were shown to be both sharp and stable enough for reagent activation.

The glass fiber material of the paper-based section was also shown to be problematic. The quasi-transparent surface properties of the material negatively impacted color formation in the detection zone resulting in the addition of noise during quantification. This of course could also add unwanted variance to measurements thereby significantly reducing the sensitivity of a device. Several glass fiber detection zones using varying concentrations of phosphate are shown in Figure 83.

The glass fiber coloration issue was resolved through the use of modified Whatman Grade 41 filter paper. Designs were printed onto the paper and heated in much the same way as detailed in the paper-based devices section with the addition of

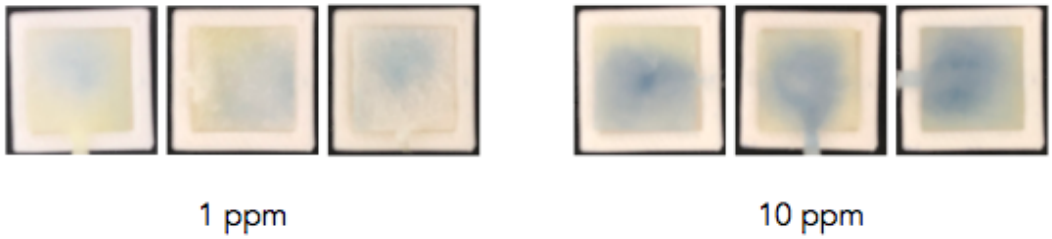

Figure 83. Issues - Glass Pad Surface

one extra step. Papers were washed with hydrochloric acid after the regular procedure in order to remove any trace of phosphate ingrained in the filter paper. This step was shown to work very well and help diminish reaction interference.

The last major issue found with the prototype device was the stability of the molybdenum complex reagent. The reagent was shown to be highly unstable and would begin to turn blue when left in solution for extended periods of time. In addition, contact with air and the paper-based section also resulted in some level of reaction within the reagent. This all added unwanted noise to measurements and even produced false positives.

3.6.3 Molybdenum Complex Stability

Joanie Racicot of Mindy Levine's chemistry team at URI devised a method for stabilizing the molybdenum complex through the use of ethylene glycol. The molybdenum complex was mixed with ethylene glycol at a ratio of 1 part molybdenum to 75 parts ethylene glycol. Results were extremely positive as the molybdenum complex was shown to be very stable in both solution, in air, and even upon contact with ascorbic acid. The mixed reagent added another dynamic to the device however as its viscosity increased significantly with the addition of ethylene glycol.

Tests were performed in order to measure the flow rate of the molybdenum reagent alone (consistency similar to water) compared to the mixed molybde-

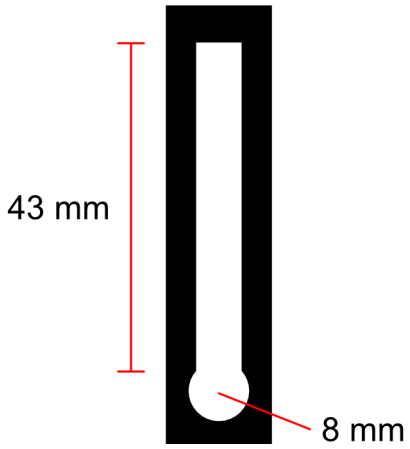

Figure 84. Molybdenum/Ethylene Glycol Flow Test Design

num/ethylene glycol reagent. A design of experiment was created where each fluid had to wick a distance of 6 cm up a 8 mm wide wax channel. Laminate was used to cover the channel so that the fluid front could not easily travel on top of the paper and was forced instead to actually wick through the paper. This design is shown in Figure 84. Water and fluid with a 1:75 water to ethylene glycol mix were used for the tests. The design of experiment was completely randomized in run order and also in channel. This way any effects caused by variability in paper properties and time were minimized.

Twenty tests were run in total, ten for water and ten for the mix. The results are shown in Table 4. As shown, the ethylene glycol mix was significantly slower than the water alone. The average water wicking time was 116.2 seconds while the average mix wicking time was 531.2 seconds. The mix was close to five times slower than the water alone. The wicking speed of the mix also slowed down significantly as the fluid traveled farther across the channel. This signifies that the original hydrostatic pressure was responsible for the initial speed of the mix.

It was clear from the tests that the molybdenum complex with ethylene glycol should not travel long distances on paper. A redesign had to be made in order to

Table 4. Ethylene Glycol Flow Tests

Channel	Fluid	Time(s)
8	Ethylene Glycol Mix	489
6	Ethylene Glycol Mix	423
11	Ethylene Glycol Mix	406
16	Water	96
18	Water	92
4	Ethylene Glycol Mix	425
12	Water	106
7	Ethylene Glycol Mix	549
21	Water	100
17	Water	124
13	Ethylene Glycol Mix	573
22	Water	128
14	Water	121
5	Water	129
3	Water	146
15	Water	120
10	Ethylene Glycol Mix	548
9	Ethylene Glycol Mix	606
1	Ethylene Glycol Mix	645
2	Ethylene Glycol Mix	648

accommodate this new flow dynamic.

3.6.4 Redesign and Prototype Chip

A redesign was created in order to incorporate the solutions to the issues explained in the issues section. The paper-based section of the device was completely redesigned to work with the molybdenum/ethylene glycol mix. A smaller and simpler design was created with one 9 mm x 9 mm reagent chamber zone, one small 6 mm channel, and a 7 mm x 7 mm detection zone. The paper-based design is shown in Figure 85. This variant was designed to incorporate ascorbic acid pre-spotted and dried in the detection zone. This was done so that no mixing channels had to be integrated. While the molybdenum reagent was shown to be very unstable when dried on paper, ascorbic acid is very stable as long as the paper

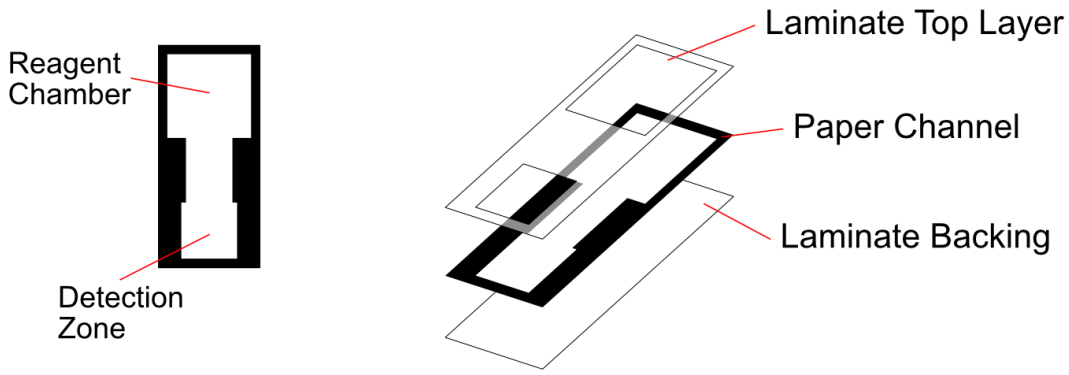

Figure 85. Redesign - Paper-Based Section

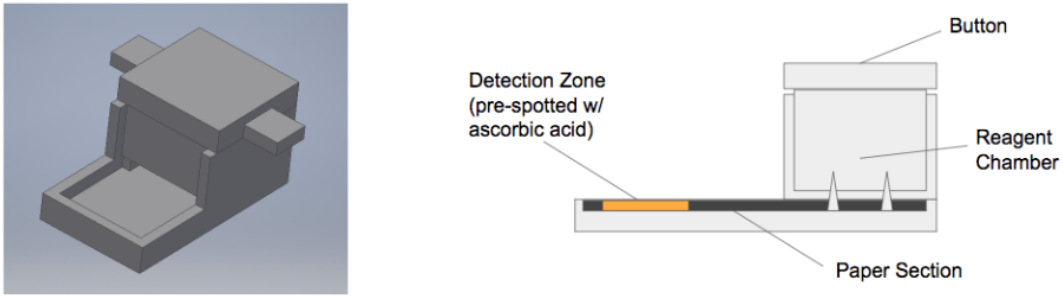

Figure 86. Redesign - Housing

is not exposed to light during storage.

The lab-on-chip housing was also redesigned to accommodate the new paper-based section. The new housing featured one reagent chamber with one button and a short ledge for the detection zone. The molybdenum/ethylene glycol mix was stored in a bubble on the reagent chamber. This design is shown below in Figure 86. It was printed using the settings detailed in Table 2 with the Grey PLA of table 3.

Device operation is fairly simple. The user must activate the reagent by pressing the button and once the reagent reaches and covers the detection zone, 20 μL of sample fluid is added to the detection zone. The colorimetric reaction is then induced within a couple of minutes. Optimization tests were performed for

the various device parameters and are detailed in the Lab on Chip section of the Findings chapter.

3.7 Infrared Detection Unit

An infrared box was built in the pursuit of attaining greater sensitivity from the molybdenum blue reaction. As mentioned in the Molybdenum Blue Method section of the Literature Review, the peak absorbance of the reaction is actually in the near infrared. This is shown in Figure 9 where the peak absorbance was found to be around 850nm. The box was designed to be a low cost alternative to spectrometry. The concept is simple, as the absorption of an object is related to its reflectance, one should theoretically be able to obtain greater sensitivity by imaging the colorimetric reaction in the infrared. The design, construction, and testing behind the infrared box is detailed below.

3.7.1 Raspberry Pi Setup

The vast majority of cameras in the market come equipped with infrared filters in order to remove unwanted noise and artifacts when capturing photos. A camera capable of imaging in the infrared was then necessary in order to take advantage of the absorption peak of the molybdenum blue reaction. A Raspberry Pi 3 Model B+ [105] along with a Pi NoIR Camera v2 [106] were chosen for the task. The Raspberry Pi is a small inexpensive computer board capable of controlling the NoIR Camera, a camera especially made for the Raspberry Pi with no infrared filter.

The Raspberry Pi is powered by a 2.5 A power supply and becomes a full-fledged computer once connected to a monitor, keyboard, and mouse. The Raspbian OS [107] was setup on the Pi as it is the primary operating system used on the boards. The Raspbian OS comes equipped with Thonny [108], a simple

Figure 87. Raspberry Pi

Python IDE. The NoIR camera can be easily controlled using the camera API with Python. Many functions are readily available that allow the user to control exposure settings, resolution, and capture format.

A custom casing for the Raspberry Pi was 3D printed in order to protect the board's electronics. The stl files were downloaded on Thingiverse [109] and then printed with the Raise 3D N2 Plus. The settings used for the light box shown in Table 1 of the Light Box section were used along with the gray PLA spool detailed in Table 2. The Raspberry Pi, NoIR Camera, and casing are shown in Figure 87.

3.7.2 Box Design

Similar to the light box, parts for the infrared box were drawn using Autodesk Inventor CAD software. The box once again consisted of three main parts: a bottom platform, a surrounding wall sleeve, and a top cover. The main difference to the light box is that the infrared box is completely sealed. The only light present inside the box is the light coming from the infrared LEDs detailed in the next section. All parts were 3D printed using the Raise 3D N2 Plus with the settings listed in Table 1 of the Light Box section with the gray PLA spool detailed in

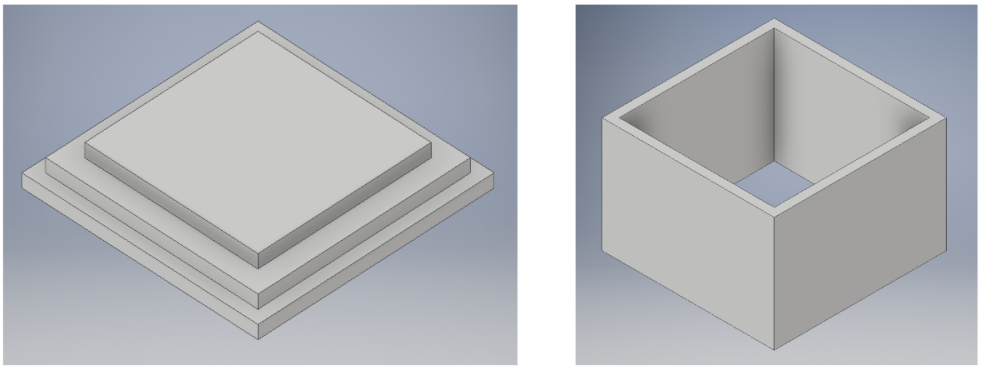

Figure 88. Infrared Box - Bottom Platform and Wall Sleeve

Table 2. Schematics and drawings for all the box parts are shown in Appendix E.

The bottom platform was once again designed with three steps. The bottom step for mating with the wall sleeve, the middle step for any auxiliary additions, and the top step/platform for laying out test strips. A handle is present in the underside of the platform to aid in detachment from the wall sleeve. The platform dimensions are much smaller than the light box as the box itself was designed to be significantly more confined. A matte black poster material was also added to the top of the platform so that light can't reflect on the PLA surface.

The wall sleeve is a 6 cm x 6 cm hollow wall that is 3 cm thick all around. The sleeve has a height of 4 cm in order to achieve a close focus with test specimens. The bottom platform and wall sleeve are shown in Figure 88.

The top cover has two major functions in the design: seal the box with no light entry and house the NoIR Camera. It was designed with four protruding pillars to fit the four mounting holes on the camera. A section of the sealing lip was also cut off in order to allow the camera's ribbon cable to freely pass through. The camera was fitted onto the pillars and the pillars were then melted using a soldering iron and flattened with a small spatula. The top cover schematic and a photo of the cover with the NoIR camera mounted are shown below in Figure 89.

The framework of the box is shown in a wireframe schematic in Figure 90.

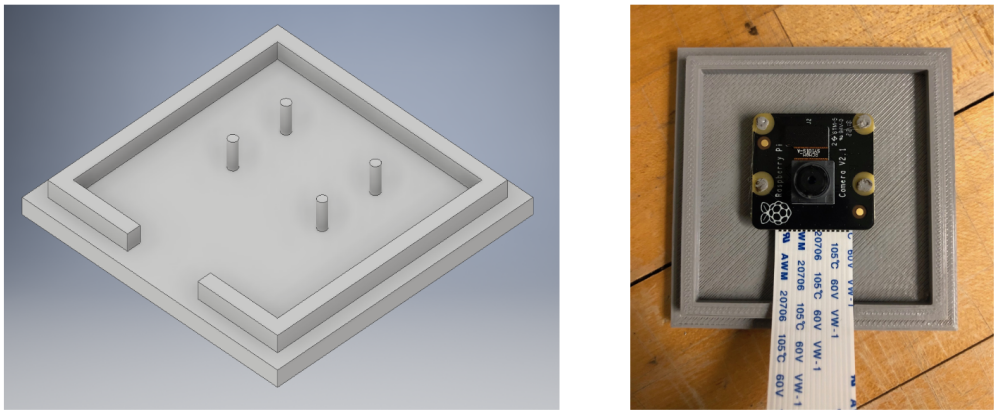

Figure 89. Infrared Box - Top Cover

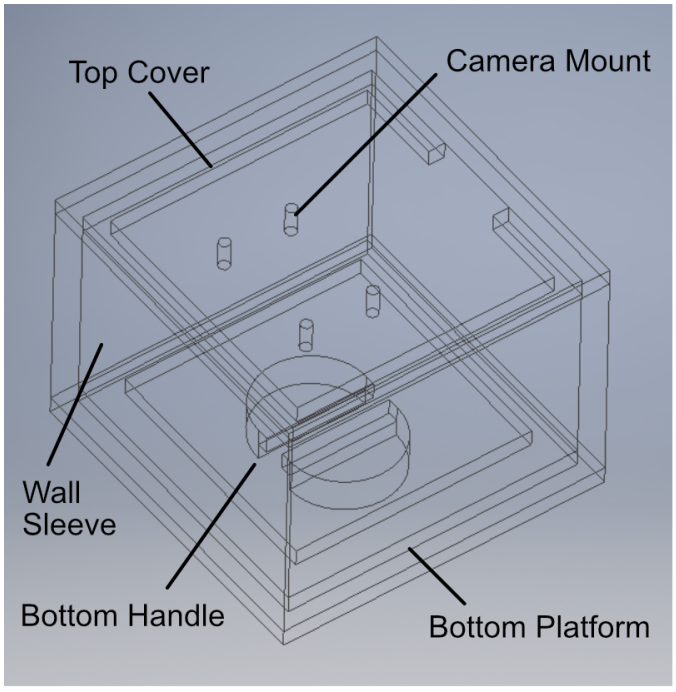

Figure 90. Infrared Box - Main Framework

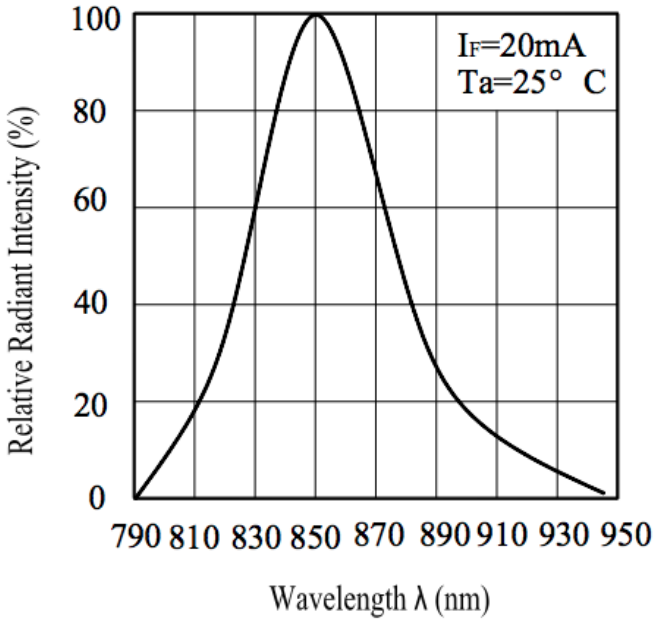

Figure 91. Infrared LED Spectral Distribution

3.7.3 Lighting and Electronics

The lighting is of course the most important element of the infrared box. Only infrared LEDs were used in order to take the advantage of the absorption peak of the molybdenum blue reaction around 850nm. Four Everlight model HIR7393C LEDs emitting infrared light at 850nm where chosen for the lighting. The spectral distribution of the LEDs are shown in Figure 91 [110]. As shown, while the peak intensity is at 850nm, the LED's spectral distribution ranges from around 800nm to 900 nm. The LED specs are listed in Table 5.

Table 5. Infrared LED Specs

Current - DC Forward (If) (Max)	100mA
Radiant Intensity (Ie) Min @ If	7.8mW/sr @ 20mA
Wavelength	850nm
Voltage - Forward (Vf) (Typ)	1.45V
Viewing Angle	50°
Operating Temperature	-40°C 85°C (TA)

A similar circuit to the light box was utilized for the infrared box. A 12V A23

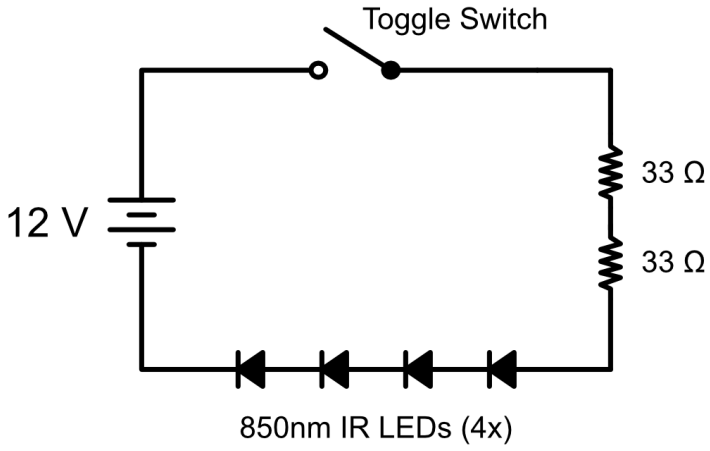

Figure 92. Infrared Box - Circuit Diagram

battery was once again used as the power source and a toggle switch was wired onto the circuit in order to manually power the LEDs on and off. The electronic compartment shown in Figure 47 was used to house the battery holder and toggle switch. The circuit of the electronics in the infrared box are shown in Figure 92.

LED brackets and wall pillars had to be designed to mount the LEDs in the box. The pillars are simply corner pieces with a flat wall front. The LED brackets were designed for the LED's top trajectory to be directly incident to the middle of the box's bottom platform. Calculations were performed accounting for a 30 mm platform to LED height and it was found that a 52° mounting was necessary. The brackets were then designed with flat hollow frames to attach to the wall pillars and a 52° mounting offset for the LEDs. The brackets were each glued to a wall pillar using loctite superglue and the pillars were subsequently glued onto the inside corners of the wall sleeve. Schematics for the LED bracket and wall pillar are shown in Figure 93.

A hole had to be drilled into the wall sleeve in order to allow wiring from the electronic compartment to reach the LEDs. The various electronic parts were then connected according to the circuit diagram shown in Figure 92. The infrared box

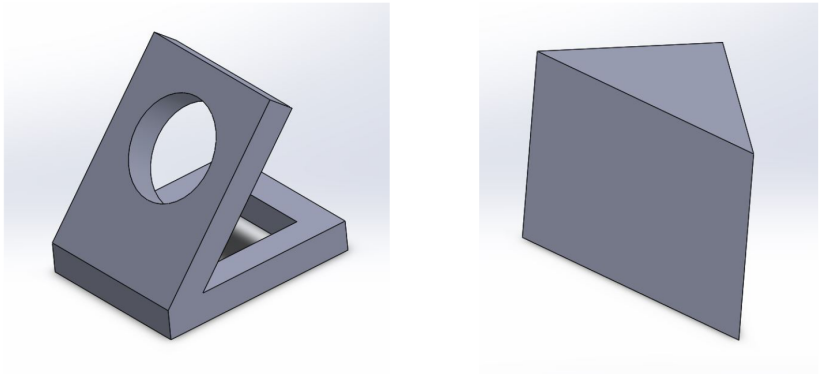

Figure 93. Infrared Box - LED Bracket and Wall Pillar

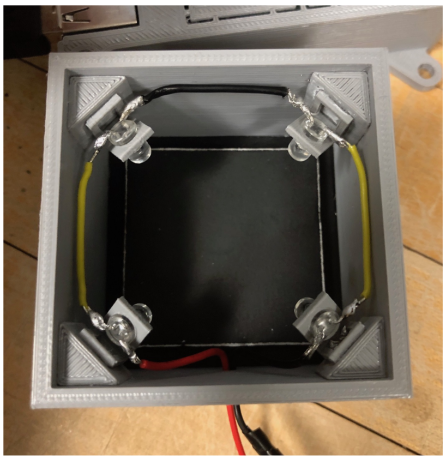

Figure 94. Infrared Box - Lighting Architecture

with the lighting architecture is shown in Figure 94 and the complete arrangement is shown in Figure 95.

3.7.4 Imaging

Imaging was performed using Python with the Raspberry Pi's Camera API. A camera.py file was created in the Thonny IDE to perform all imaging functions. Controlling the camera is quite simple. A preview function outputs what the camera sees onto the screen and a capture function is used to output images. The capture function can handle a variety of different formats including outputting RGB data directly. The camera preview output is shown in Figure 96.

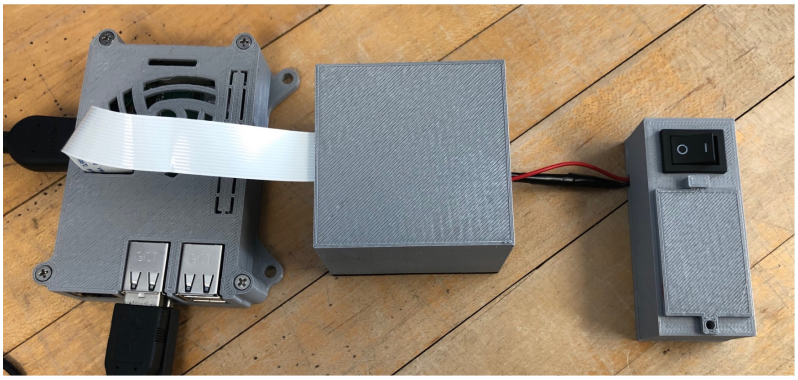

Figure 95. Infrared Box - Complete Arrangement

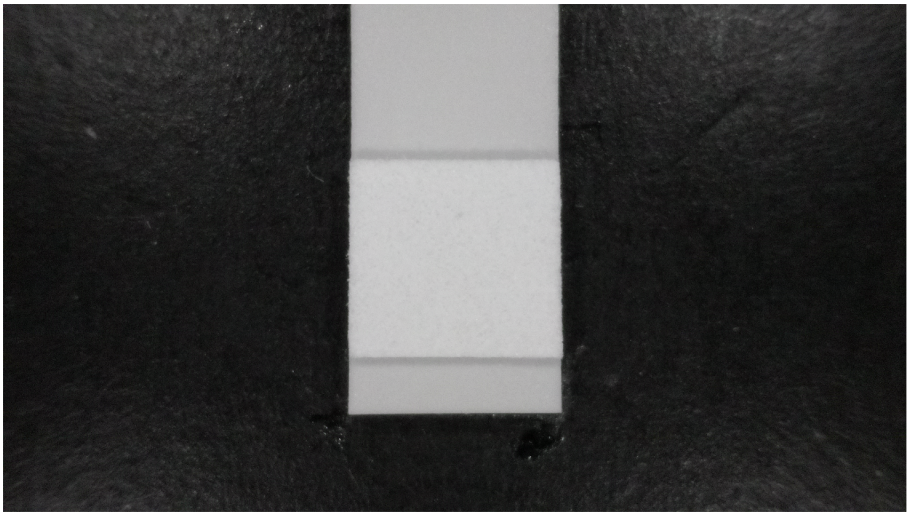

Figure 96. Infrared Box - Camera Preview

As mentioned in the Camera and Detection Technology Section of the Literature Review, controlling the exposure settings of the camera are absolutely critical when measuring RGB values. The NoIR Camera comes equipped with a fixed aperture of f/2.8. This leaves the ISO, shutter speed, and white balance to adjust. The ISO in the NoIR camera is made up of two variables, digital gain and analog gain. These variables are not directly accessible so the ISO itself cannot be truly fixed. The RAW Bayer data can be retrieved from a capture however. RAW data is the data that the sensor sees without any GPU processing steps. This renders the ISO, white balance, and other processing settings irrelevant. Only the shutter speed must then be fixed when capturing in a RAW format. The shutter speed was set to a value of 100 in order to correspond with good lighting conditions in the box.

The RAW Bayer data uses the full resolution of the sensor, 3280 x 2464. The preview resolution was set to 1640 x 1232 to have a proportionally equivalent view to what the sensor actually sees. The detection zone of a test strip is only a fraction of the view window. As such, the only relevant image data is that which is within the detection zone area. An overlay analysis area was created to visually see what the data will capture. The detection zone was measured on the screen and found to be 23 % of the view width. This proportion was lowered to allow for tolerances in the pad and when converted to pixels amounted to a value of 300px. A 1640px x 1232px transparent png image with a 300px center square analysis region was created for the preview overlay. This overlay is shown in Figure 97.

Since the full sensor resolution is twice that of the preview resolution, the 300px analysis region corresponds to a 600px center region in the RAW data. The Bayer RAW data capture, array conversion, and RGB analysis are all detailed in the next section.

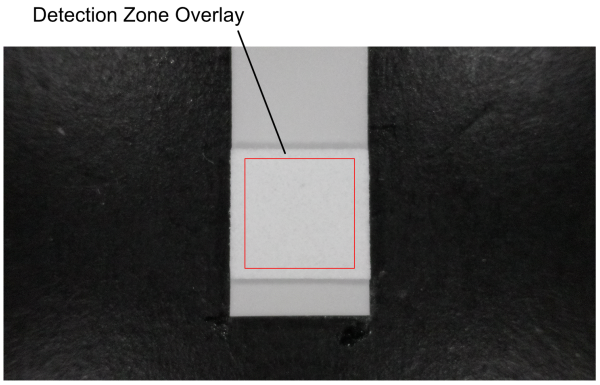

Figure 97. Infrared Box - Detection Zone Overlay

	Bits							
	MSB 8	7	6	5	4	3	2	LSB 1
Bytes 1	10	9	8	7	6	5	4	3
2	10	9	8	7	6	5	4	3
3	10	9	8	7	6	5	4	3
4	10	9	8	7	6	5	4	3
5	2	1	2	1	2	1	2	1

Figure 98. Bayer Data Packaging

3.7.5 Bayer and RGB Data

The RAW Bayer data capture on the Raspberry Pi consists of 32,768 bytes of header data and 10,270,208 bytes of actual Bayer data. As mentioned in the Camera and Detection Technology Section of the Literature Review, bayer data is organized in a BGGR pattern where there are twice as many green pixels as there are red and blue pixels. These data are stored in 10-bit values in packages of five bytes. The first four bytes consist of 8-bit values for each pixel and the last byte has the low-order 2-bits for each of the four pixels. The arrangement is shown in Figure 98 [111].

The Pi Camera API has a very convenient function that performs a simple de-mosaicing step on the Bayer data. This de-mosaicing function outputs a full

resolution 3280 x 2464 3-channel RGB array. This array can then be used to find average RGB and intensity values. As mentioned in the last section, the analysis region corresponds to a 600 x 600px center square in the RAW data. The data was simply sliced from row 932 to 1532 and column 1340 to 1940. The resulting output is a 600 x 600 array corresponding to the detection zone in the Quantofix test strip.

Averaging functions were then used on the array to get the mean values for the red, green, and blue pixels. Unweighted intensity values were calculated by taking the average between the three RGB mean values. Weighted intensity values were calculated as well using Equation 6. The run order of the camera.py program is then as follows:

1. Set camera shutter speed to 200
2. Set preview resolution to 1640 x 1232
3. Add analysis region overlay to preview
4. Sleep the script for five seconds to allow camera to settle
5. Capture RAW Bayer data
6. Perform basic demosaicing to convert RAW data to RGB format
7. Slice the data to retrieve the center 600 x 600 px region
8. Calculate and print average RGB and intensity values

Matplotlib, a Python 2D plotting library, was used to recreate the array data into an image. This was done to ensure that the program was running as intended. The recreated image from a test strip capture is shown in Figure 99. As shown the image coloring is quite strange due to no preprocessing steps being performed.

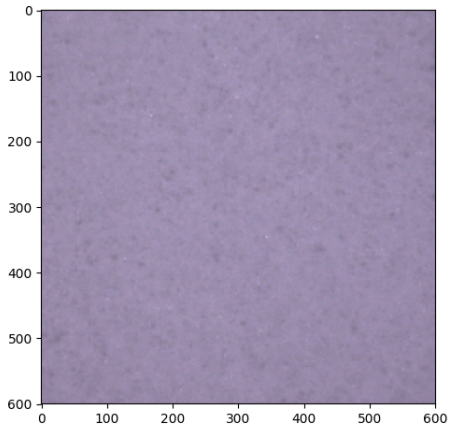

Figure 99. Recreated Image from Bayer Data

The region captured was undeniably the detection zone however as there is no evidence of the backing poster anywhere on the image.

3.7.6 Efficacy Evaluation on Quantofix Phosphate Kit

The Quantofix test strips were tested and analyzed using the infrared box in much the same way as they were with the light box in the Commercial Devices section. The manufacturer procedure was used to induce colorimetric reactions on the strips and then the average RGB and intensity values were measured using the infrared box. Tests were once again run in triplicates format with three tests for each level of phosphate concentration: 0, 0.1, 0.2, 0.5, 1, 2, 5, 10, 20, 50, and 100 ppm. Concentration curves were made from the data and used to directly compare with the results found using the light box. These results are shown and discussed in the Infrared Detection Unit section of the Findings chapter.

CHAPTER 4

Findings

This chapter presents the various results obtained in this study. The first section discusses the performance of two popular commercial devices, the Indigo Phosphate Test Strips and the Quantofix Phosphate Test Kit. The RGB App section then details the feasibility of using such an app for instantaneous chemical quantification. The Lab on Chip device, it's performance, and commercial viability is detailed in the Lab on Chip Device section. Finally, results obtained by measuring the Molybdenum Blue reaction using the infrared box is elaborated in the Infrared Detection Unit section.

4.1 Commercial Devices

As mentioned in the Methodology, the Indigo Phosphate Test Strips and the Quantofix Phosphate Test Kit were tested in order to acquire an understanding of the current market. The sensitivity of these devices were tested using the light box in conjunction with the imaging software ImageJ. The results obtained along with some of the advantages and disadvantages of each device are detailed below.

4.1.1 Indigo Instruments Phosphate Test Strip

The Indigo Instruments Phosphate Test Strips were the first commercial devices tested. These are very simple dip strips that only require the user to dip the strips in the water sample being tested. These test strips are incredibly convenient because of their simplicity but come with a couple shortcomings. Visual tests showed that the induced color on some strips did not entirely fill the test pads. In addition, the reflective surface of the strips' plastic material creates light artifacts on the surface of the strip. These properties can skew and alter results

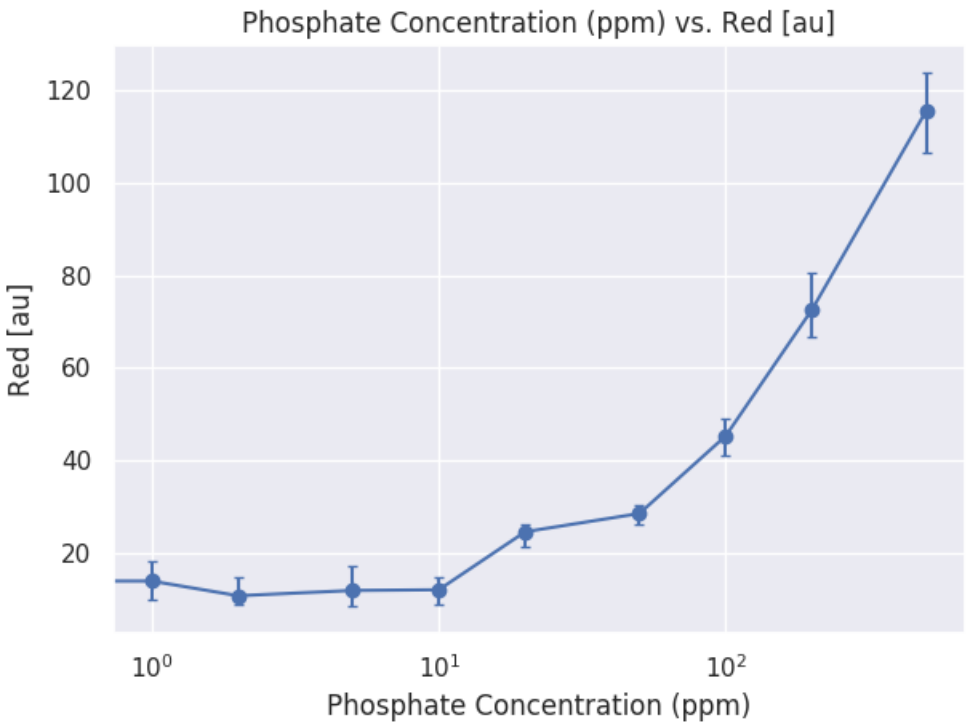

Figure 100. Indigo Phosphate Test Strips - Phosphate Concentration vs. Red

obtained from colorimetric imaging on ImageJ which leads to issues in quantifying phosphate levels.

A calibration curve was created from testing the test strips' color (RGB) vs. phosphate concentration. Three measurements with different strips were taken for 0, 1, 2, 5, 10, 20, 50, 100, 200, and 500 ppm phosphate solution in water. The curve formed from Phosphate Concentration [ppm] vs. Red [au] is shown in Figure 100.

As shown above, the limit of detection (LOD) is observed around 20 ppm. This is of course quite insensitive and will not be adequate for most applications. The main advantages of the Indigo strips are that they are convenient, inexpensive, and easy to use. These advantages are not sufficient to overcome the lack of sensitivity however as there is a need for ppb detection in the market.

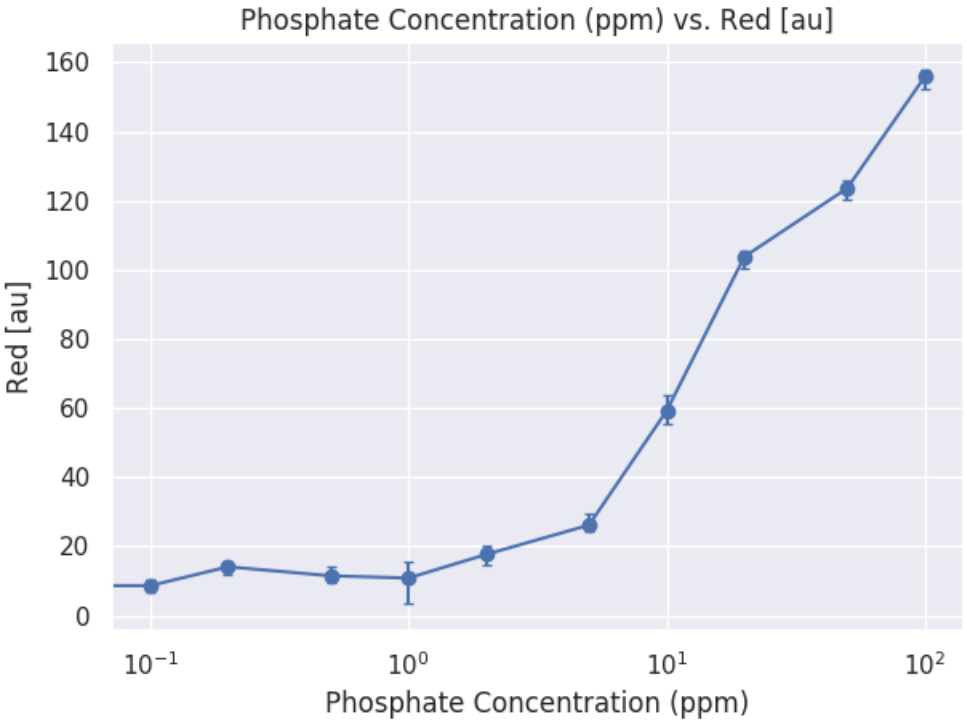

Figure 101. Quantofix Phosphate Test Kit - Phosphate Concentration vs. Red

4.1.2 Quantofix Phosphate Test Kit

The Quantofix Phosphate Test Kit was tested under the same conditions as the Indigo Phosphate Test Strips. The Quantofix kit has a more involved procedure as explained in the Methodology. The user must handle two reagents, a molybdenum mix and nitric acid. This is of course a major disadvantage as it introduces both the possibility of user error and a safety concern. The kit does come with the added promise of higher sensitivity when compared to the Indigo strips however.

A calibration curve was created from testing the strips much like one was for the Indigo strips. Three measurements with different strips were taken for 0, 0.1, 0.2, 0.5, 1, 2, 5, 10, 20, 50, and 100 ppm phosphate solution in water. The curve formed from Phosphate Concentration [ppm] vs. Red [au] is shown in Figure 101.

As shown in Figure 101, the limit of detection (LOD) is observed around 5 ppm. While this is much better than the Indigo test strips, it is still not adequate.

As mentioned, ppb detection is required in order to quantify phosphate levels in many bodies of water. In addition, the complicated procedure and handling of reagents is a serious concern for the citizen scientist.

4.1.3 Optimization of Colorimetric Detection Methods

An interesting phenomenon was observed when creating the calibration curves for both the Indigo test strips and the Quantofix Test Kit. As shown in the previous figures, the average red pixel intensity values were used for quantification. Average red, green, blue, RGB (total average), unweighted intensity, and weighted intensity values were measured for each test. The red was chosen as it had the most specificity and least variance among the choices. This was a very peculiar result as one would most likely assume that blue would be the best choice since the colorimetric reaction is in fact blue. As a matter of fact, blue actually performed the worst out of all the measurement choices which is completely counter-intuitive to what one would expect.

The blue measurements for the Indigo test strips and Quantofix test kit are shown in Figures 102 and 103 respectively.

As shown in the figures, the blue curves are extremely erratic with very large error bars. The indigo strips can't be quantified reliably at all using the blue curve while the limit of detection of the Quantofix test kit rises to around 10 ppm. More measurements were taken and the same behavior was once again present. Why did the blue intensity give such a terrible calibration curve for a blue reaction while the red did not. The answer was found in the absorption spectrum of the Molybdenum Blue reaction shown in Figure 104.

The Molybdenum Blue reaction induces a blue color because the longer wavelength side of the spectrum is absorbed while the blue 400 - 500 nm region is not. The highest absorbance values are observed between 700 - 900 nm with the high-

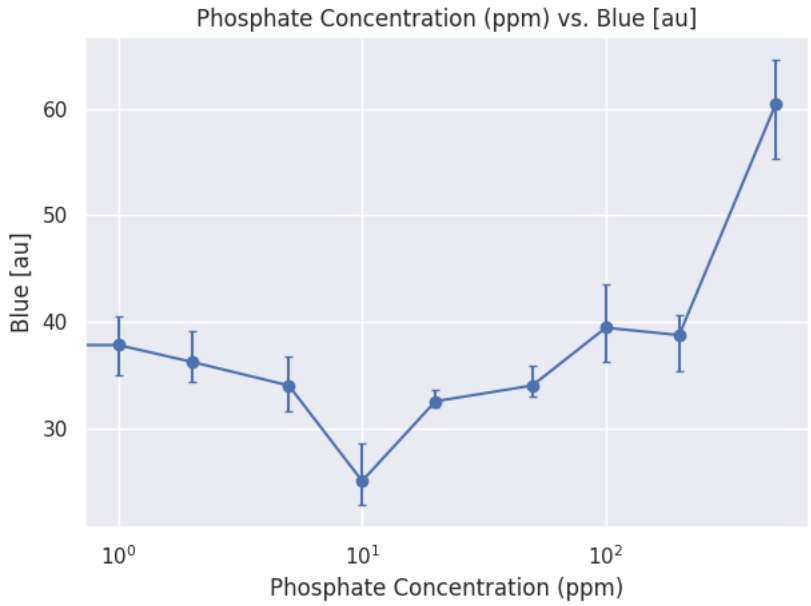

Figure 102. Indigo Phosphate Test Strips - Phosphate Concentration vs. Blue

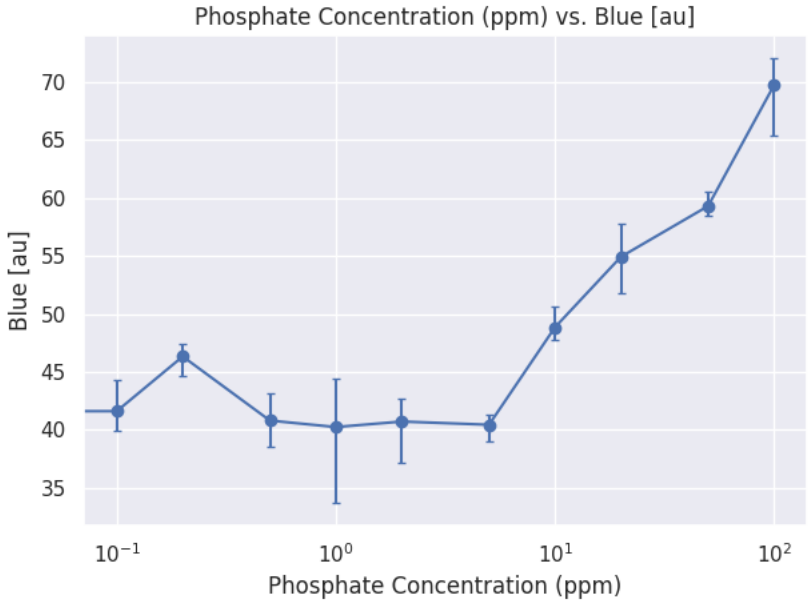

Figure 103. Quantofix Phosphate Test Kit - Phosphate Concentration vs. Blue

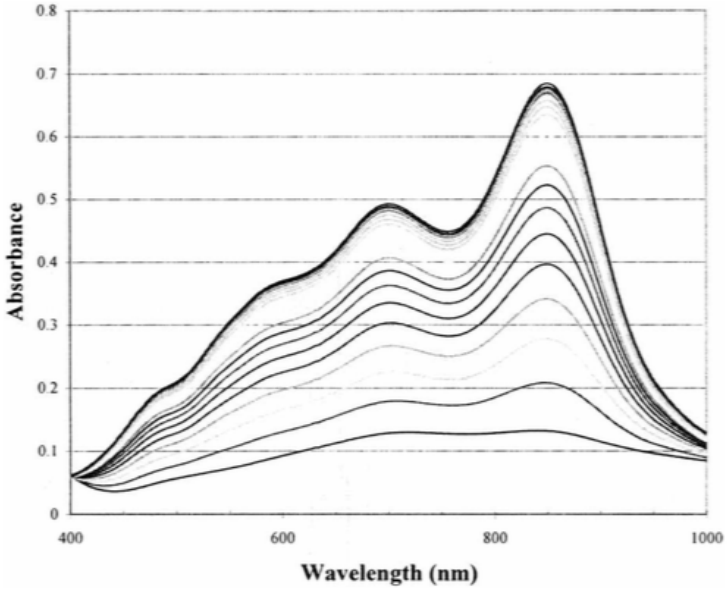

Figure 104. Molybdenum Blue Reaction Absorption Spectrum [Figure 9 Reproduced]

est peak at 850 nm. As shown in Equation 7 of the Color Theory section in the Literature Review chapter, the absorbance, reflectance, and transmittance are all related to each other. What this means is that as absorbance changes so will the reflectance or what we actually see. The red curve performed the best as red is in an area of the spectrum with high absorption and more importantly, large jumps in absorption between different concentrations. These large jumps result in large changes in absorption as well as reflectance. In other words, the reflectance of the red intensity undergoes significant change as phosphate concentration is varied.

The blue side of the absorption spectrum on the other hand exhibits low absorption values and minuscule jumps between concentrations. The reflectance of the blue intensity does not vary significantly with differing phosphate concentrations therefore. The small jumps are then responsible for the erratic and high variance behavior of the blue curve as there isn't much change in absorption and reflectance to be observed. In short, the best RGB color channel to perform quan-

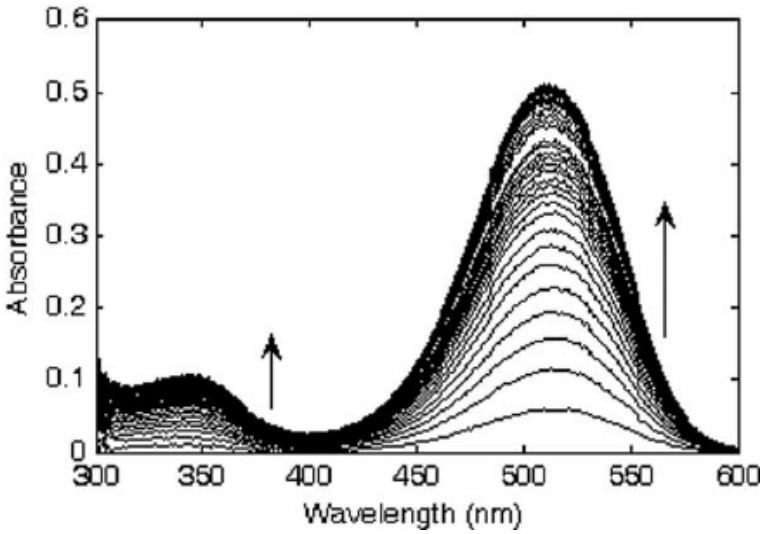

Figure 105. Griess Reaction Absorption Spectrum [112]

tification measurements is the one with the highest changes in absorption between concentration levels.

This theory was put to the test using the Griess reaction present in Nitrite and Nitrate detection. The Quantofix Nitrate Test Strips were used for this task. The absorption spectrum of the reaction is shown in Figure 105 [112]. A shown, the absorption peak and area of highest change is around 520nm. This wavelength in the spectrum corresponds to green visible light. Green intensity pixel values should then perform the best when quantifying Nitrite/Nitrate levels. A red/pink color is induced on the test strips as the red side of the spectrum is not absorbed during the reaction. If the theory is correct, the red intensity pixel values should perform the worst in quantification.

As suspected, the green curve performed the best out of all the measurements with the best specificity and lowest variance. Similar to the blue curve in the Molybdenum Blue reaction, the red curve performed the worst with erratic behavior and high variance. The curves are shown in Figures 106 and 107 respectively.

Further testing should be performed with other reactions to see if the theory

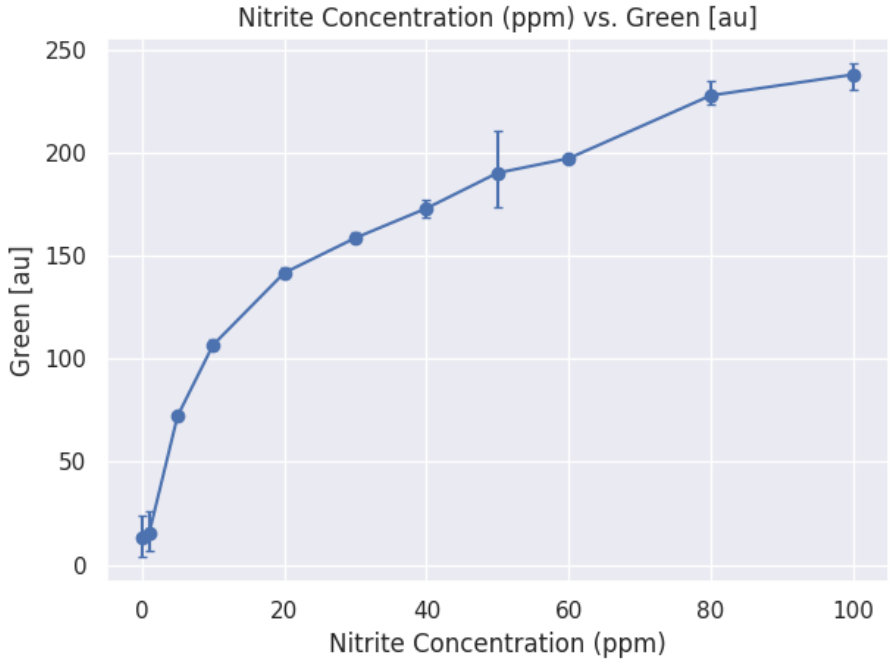

Figure 106. Quantofix Nitrite Strips - Concentration (ppm) vs. Green Intensity [au]

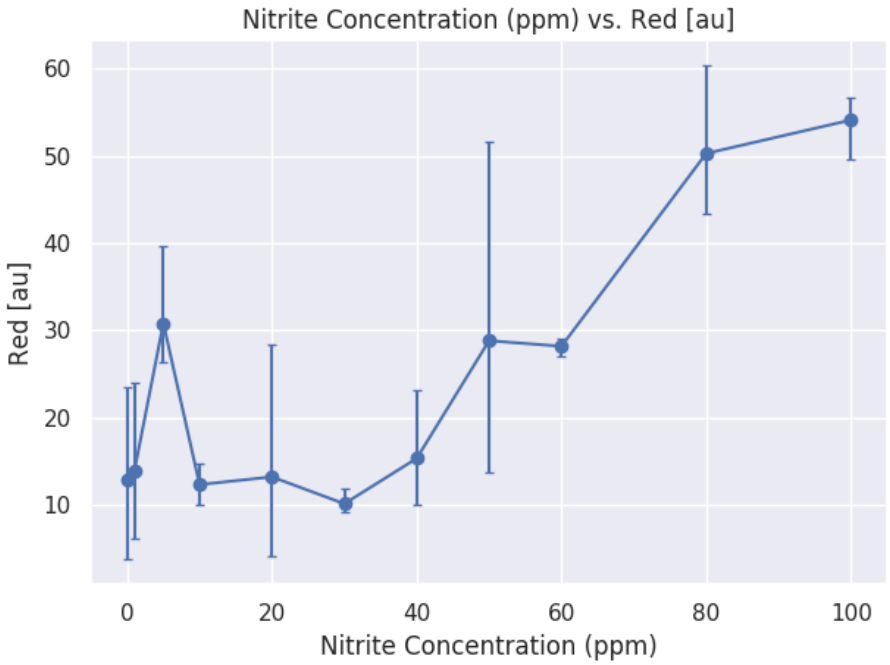

Figure 107. Quantofix Nitrite Strips - Concentration (ppm) vs. Red Intensity [au]

still holds up. In addition, it may be possible to significantly improve a reaction's quantification by the use of 'Artificial Color Channels' (ACC). A reaction with a strong absorption peak in the yellow region of the light spectrum may benefit significantly from a yellow color channel. This color channel can be artificially produced by averaging the green and red RGB channels. This concept could be further extended by calculating the area of largest absorption jumps mathematically and producing an Artificial Color Channel based on RGB coefficients that correspond to said area.

4.2 RGB App

A calibration curve was made on the Indigo phosphate test strips using the RGB app. This was done in order to gauge the feasibility of using such an app for instant quantification in the field. The curve was created by using the app to take snapshots of the color induced on the strips using 0, 10, 25, 50, 75, and 100 ppm of phosphate sample. The light box was used to provide a consistent lighting environment for the measurements. The curve is shown in Figure 108. As shown, the results are very disappointing as there is a lot of variance between measurements of the same concentrations. In addition the color intensity starts to diminish around 100 ppm.

The reasoning behind these results is due to the iOS camera API used to lock the exposure settings. After careful observation and debugging, it was shown that the customLocked feature of the API does not work as intended. The function should lock the exposure settings of the phone camera at the specified values mentioned in the Methodology chapter. The settings do indeed lock but only for a short period of time. Debugging revealed that exposing the camera lens to different light intensities altered the exposure settings rendering measurements inaccurate and unstable. Unfortunately there is no way to fix the issue as the problem is

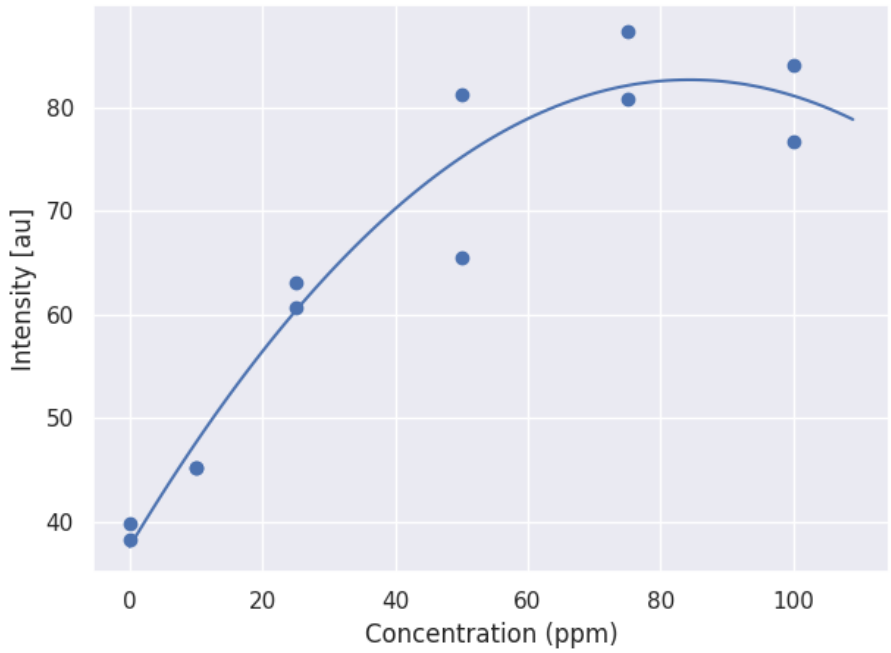

Figure 108. RGB App Fit on Indigo Test Strips

within the API itself. There are workarounds detailed in the Future Work section that may be able to remedy the problem.

4.3 Lab on Chip Device

The lab-on-chip device was created in conjunction with Joanie Racicot of Mindy Levine's chemistry team at the University of Rhode Island. She performed multiple chemistry optimization tasks and stability tests. In addition, different volumes and ratios were tested collaboratively in order to improve the device. The tests performed and results obtained are detailed below.

4.3.1 Chemical Concentrations

Joanie performed several tests in solution in order to optimize the chemistry and have initial concentrations for each reagent. The reagents in question were ascorbic acid and the molybdate complex of course. The final molybdate complex consisted of a mixture of 0.126 M ammonium molybdate tetrahydrate with 5 mM

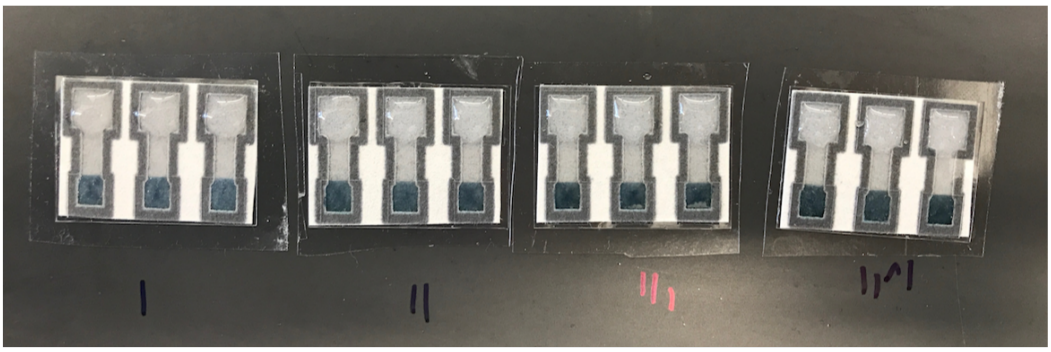

Figure 109. Ascorbic Acid Aliquots Tests

of potassium antimony dissolved in 6.6 M sulfuric acid. 1 mL of this mixture was diluted with 1.425 mL of various ethylene glycol ratios detailed in the Molybdenum to Ethylene Glycol Ratio section. Lastly, 0.5 M ascorbic was chosen as the reducing reagent. These concentrations were used in all of the subsequent tests.

4.3.2 Ascorbic Acid Volume

Several chemical tests were performed in order to select the best volumes, concentrations, and ratios for each of the reagents. The first test performed involved the amount of ascorbic acid deposited in the detection zone. Four different aliquots (1, 2, 3, and 4) of 3 μL of ascorbic acid were dried onto the paper in order to see which produced the most intense color. The molybdenum/ethylene glycol ratio and 25 ppm phosphate sample volume were held constant for this test at 50 μL of 1:75 and 20 μL respectively. The detection zone was quantified using ImageJ after 5 minutes. A photo of the tests and the results are shown in Figures 109 and 110 respectively.

As shown on Figure 110, more aliquots of ascorbic acid performed much better than lower ones. It is clear from the tests that four aliquots had the best results.

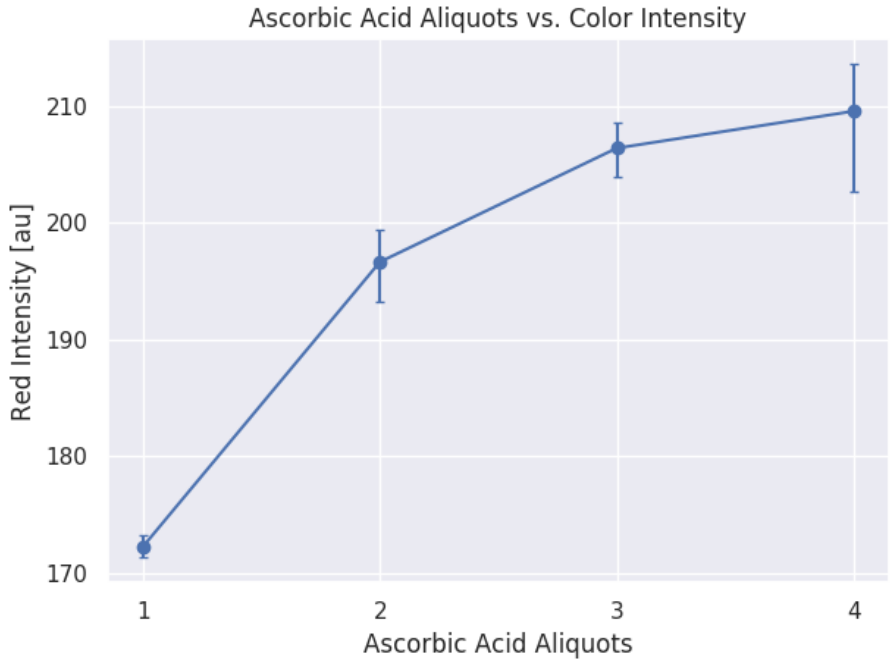

Figure 110. Ascorbic Acid Aliquots vs. Red Intensity [au]

4.3.3 Molybdenum to Ethylene Glycol Ratio

Different molybdenum/ethylene glycol ratios were tested in order to find the best compromise between stability, color intensity, and flow rate. 50 μL of no ethylene glycol, 1:25, 1:50, 1:75 were chosen for testing. Four aliquots of 3 μL of ascorbic acid and 20 μL of 25 ppm phosphate diluted in water sample volume were used for each test. The detection zone was once again quantified using ImageJ after 5 minutes. A photo of the tests are shown in Figure 111.

As shown in Figure 111, no ethylene glycol and the 1:25 ratio developed a very deep and intense blue color throughout the entire paper-based section. These color reactions occurred before the addition of any sample. These two options were immediately eliminated as they could not possibly be used for measurement. The 1:50 and 1:75 ratios showed very promising results however as color was only developed upon sample addition and was confined to the detection zone. These two ratios were tested using ImageJ, the results are shown in Figure 112.

Figure 111. Molybdenum to Ethylene Glycol Ratio Tests

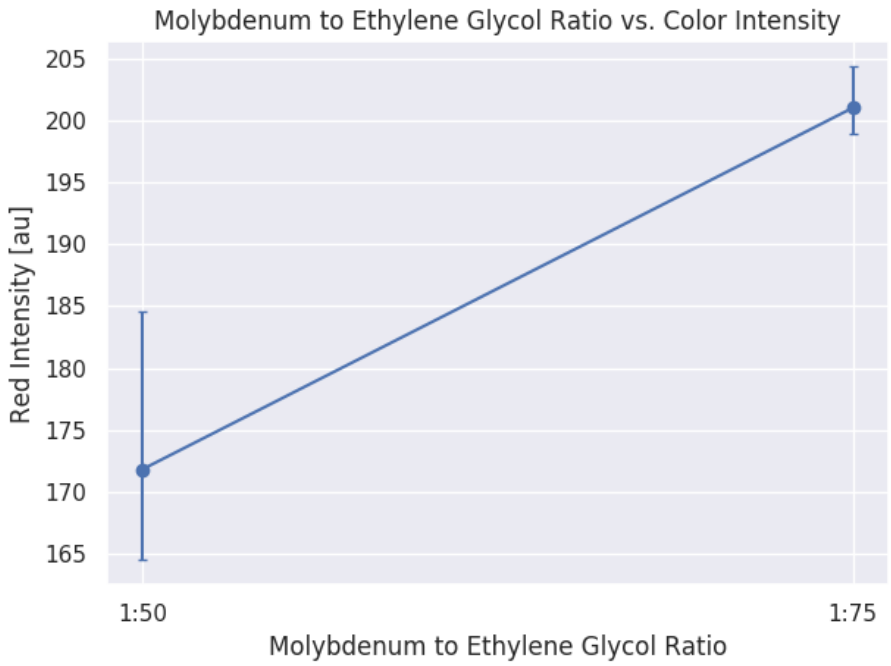

Figure 112. Molybdenum to Ethylene Glycol Ratio vs. Red Intensity [au]

Figure 113. Sample Volume Tests

Figure 112 shows that the color intensity was in fact greater at 1:75 when compared to 1:50. The 1:75 is unfortunately more viscous of course but the added intensity is desirable as it translates to greater sensitivity and a lower limit of detection. Higher ratios were not tested as they would have a negative impact on both flow rate and device operation time. A 1:75 ratio was then chosen for the final device.

4.3.4 Sample Volume

Sample volumes of 25 ppm phosphate solution diluted in water were varied to find which volume produces the best colorimetric response. 10, 15, 20, 25, and 30 μL of sample were tested on the device. Four aliquots of 3 μL of ascorbic acid and 50 μL of a 1:75 molybdenum to ethylene glycol ratio were used for each test. Tests were quantified after five minutes using ImageJ. Photos of the tests and the results are shown in Figures 113 and 114 respectively.

As shown above, sample volume had a significant effect on coloration. This could be due to the dried ascorbic acid in the paper being rehydrated better with higher volumes. 25 μL and 30 μL had very similar results that can't be distinguished using the naked eye. ImageJ results showed that 25 μL had the slight edge and as such was chosen for the device.

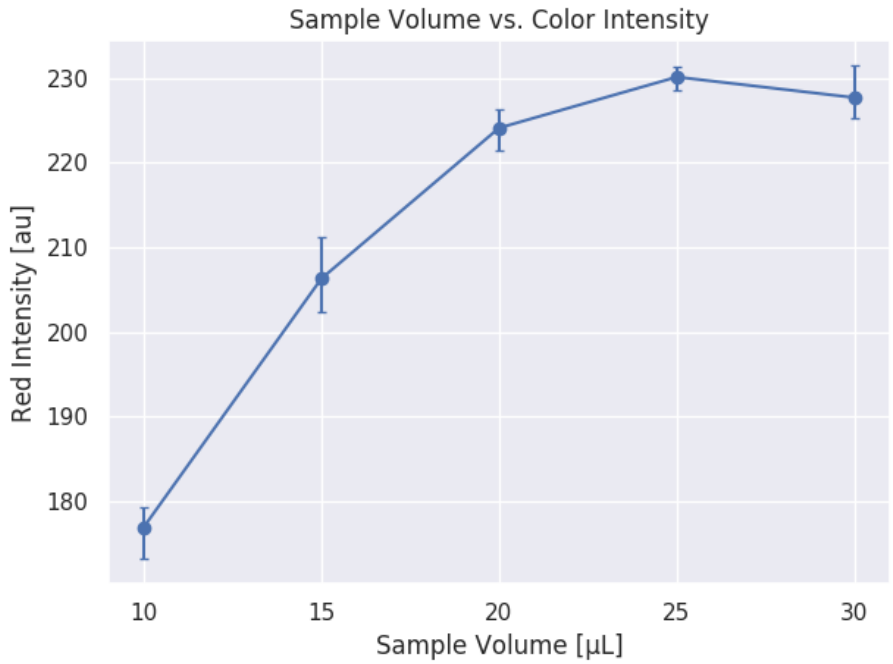

Figure 114. Sample Volume vs. Red Intensity [au]

4.3.5 Stability Tests

Several stability tests were performed by Joanie Racicot comparing the stability of the molybdenum complex on paper with and without ethylene glycol. Figure 115 shows the red intensity value of the paper color for reagents dried on paper and kept in the dark. Results showed that the intensity value quickly changed after only a few days for the complex without ethylene glycol. When ethylene glycol was added, significant changes to the color was observed only after 20 days.

The same was then run except specimens were kept in the refridgerator. Results are shown in Figure 116. As shown, A small change in red intensity occurred around the 4 day mark for the solution with ethylene glycol but the values stayed consistent up to 40 days thereafter. Once again the solution without ethylene glycol was quite unstable and quickly changed color after a few days.

Stability tests with the molybdenum ethylene glycol mix in the bubble storage also showed that no color changed was induced in the dark after several days. A

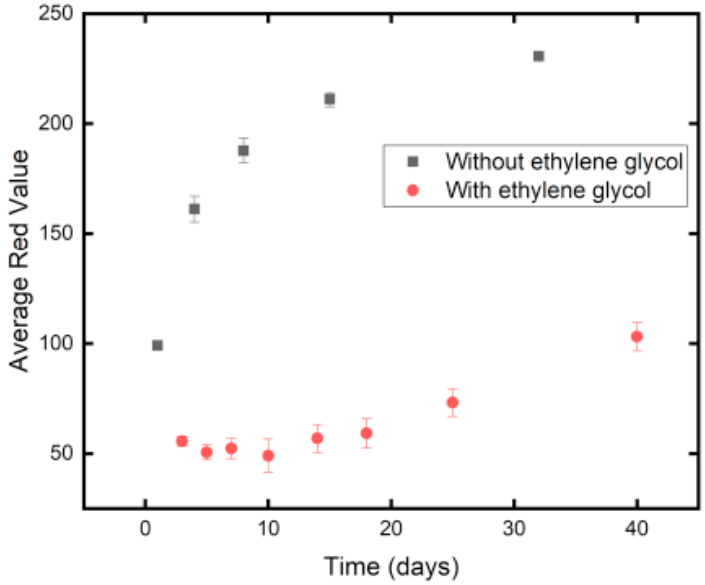

Figure 115. Molybdenum Complex w/ and w/o Ethylene Glycol Dried on Paper and Kept in the Dark

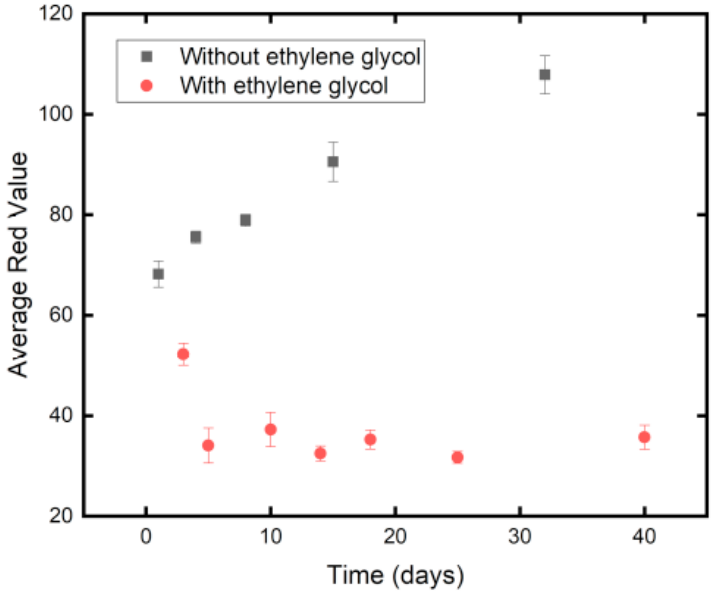

Figure 116. Molybdenum Complex w/ and w/o Ethylene Glycol Dried on Paper and Kept in the Fridge

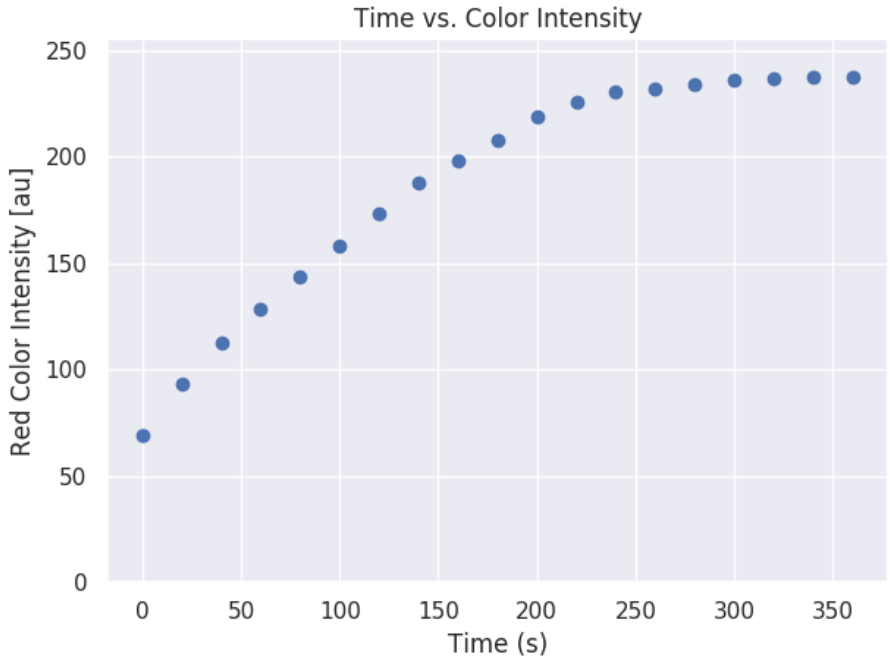

Figure 117. Time vs. Color Intensity

very promising result indicating robustness in a potential devie.

4.3.6 Timing Tests

The color intensity over time was measured using the optimal parameters found in the previous tests. Four aliquots of 3 μL of ascorbic acid was deposited onto the detection zone. 50 μL of 1:75 molybdenum complex to ethylene glycol ratio was used for the reagent. Finally, 25 μL of 10 ppm phosphate solution was added to the detection zone for testing. The test was conducted in triplicates and the average color intensities was taken in intervals of 1 minute. The test ran for 6 minutes in total in a controlled light environment. The results from the test are shown in Figure 117.

As shown in Figure 117, the color intensifies very rapidly initially but then begins to plateau around the 250 second mark. Tests with other concentrations showed that eventually all solutions reach the color intensity present in the plateau.

This signifies that the color should be measured some distance from the 250 second point in order to make quantifiable measurements. An additional test was run with the same parameters except that a blank or control solution of ultra pure water was used. This test was done to find the maximum time that a solution could be left to settle without intensifying in color. Tests showed that it took the control solution over three minutes to begin developing any visible coloration. Three minutes was then chosen for the timing to be used for measurements.

4.3.7 Final Procedure and Parameters

The final device procedure and parameters were chosen following the optimization tests. Based on the tests, four aliquots of 3 μL of ascorbic acid was deposited on the detection zone and allowed to dry. One bubble storage was filled with 120 μL of 1:75 molybdenum complex/ethylene glycol in order to account for any fluid stuck in the bubble. This higher volume does not affect the reaction in any shape or form as the detection zone has a fixed fluid capacity and the laminate layer prevents any fronts from simply flowing over the paper. 25 μL of sample fluid was chosen as the volume to deposit onto the detection zone once the zone became wetted with the reagent.

The commercial device procedure would then be as follows:

1. Open light and humidity sensitive packaging
2. Activate the molybdenum reagent by pressing the button
3. Wait two minutes for the reagent to travel to and cover the detection zone
4. Add 25 μL of sample to the detection zone using a provided mini pipette
5. Wait three minutes for the color to intensify
6. Take a photo using the light box

7. Analyze the center of the detection zone using ImageJ

4.3.8 Limit of Detection

Device performance was measured based on sensitivity and limit of detection. A calibration curve was developed on the device by testing concentrations ranging from 0 to 1 ppm. Each concentration was tested in triplicate format. A limit of detection was subsequently determined based on the slope of the curve obtained and the standard deviation of the lowest concentration. The limit of quantification was found in a similar manner. The equations used to determine the LOD and LOQ are shown in Equations 9 and 10 respectively where σ is the standard deviation and S is the slope of the calibration curve.

$$LOD = \frac{3\sigma}{S}$$

Equation 9

$$LOQ = \frac{10\sigma}{S}$$

Equation 10

The procedure detailed on the last section was used for each test. The resulting curve and calibration curve equation is shown in Figure 118. The equation parameters are as follows: A1 = 17.45, t1 = 0.02, A2 = 9011.48, t2 = 131.17, and y0 = -8816.62. The intensity was plotted without inversion from the raw data in order to fit the curve. This means that lower intensity values in the graph are in fact darker unlike the previous analyses.

As shown in Figure 118, the device performed fairly well at detecting low concentrations. It achieved a final limit of detection of 12 ppb and a limit of quantification of 40 ppb. These results are remarkable and significantly better

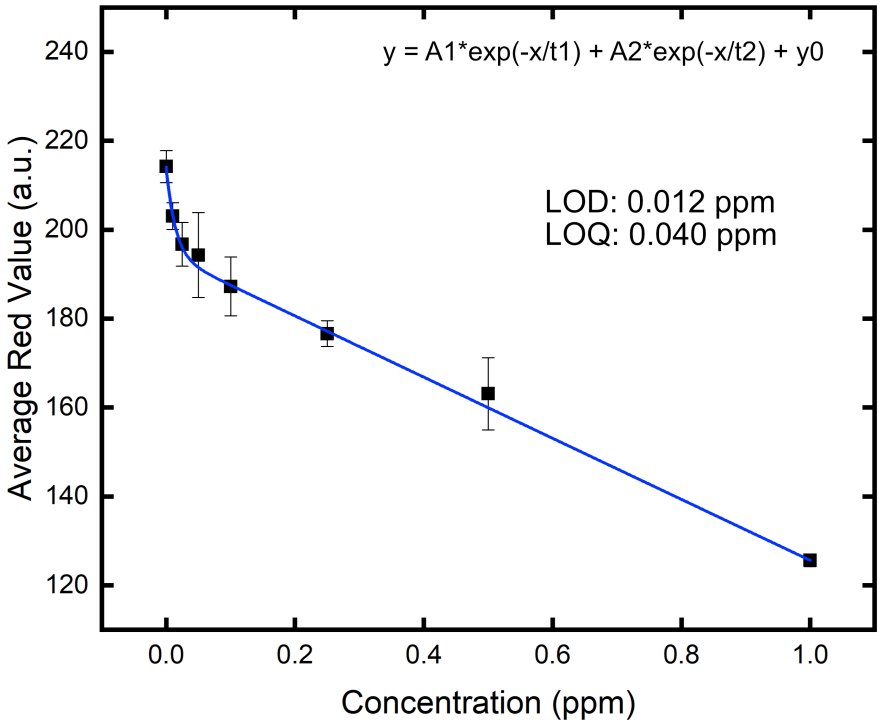

Figure 118. Concentration vs. Color Intensity

than the currently available commercial devices as the Indigo strips and Quantofix phosphate test kit reached limits of detection of 20 and 2 ppm respectively. In addition, there is no handling of dangerous reagents by the user unlike the procedure found in the Quantofix kit. This device has the potential to be very competitive in the market. There are of course some issues present however as the variability found in measurements was shown to be somewhat worrying. Future work will have to be done in reducing the variability in order to launch into the market.

4.4 Infrared Detection Unit

The infrared detection unit was evaluated based on the increase in sensitivity achieved. This performance metric was measured by testing the Quantofix Phosphate Test strips with the box in the same format as in the Commercial Devices section. The results from the test are detailed below.

4.4.1 Efficacy Evaluation on Quantofix Phosphate Kit

The Quantofix test strips were tested in the same format as they were in the Commercial Devices section. Triplicates were run for 0, 0.1, 0.2, 0.5, 1, 2, 5, 10, 20, 50, and 100 ppm. Measurements for each strip were taken directly after the Quantofix reaction procedure. This was done to obtain a directly comparable result between infrared and visual imaging of the Molybdenum Blue method. Imaging in the infrared has some differences to visual light as there is no color. The camera sees in black and white essentially. This gives some interesting properties to the measurements as all color channels should have the same value (greyscale values are simply formed by setting all channels to the same constant value). This was not exactly achieved during testing due to the weighting given to each channel during the demosaicing procedure. The differences are not a concern however, as they are still a linear combination of the raw 'black and white' values and therefore

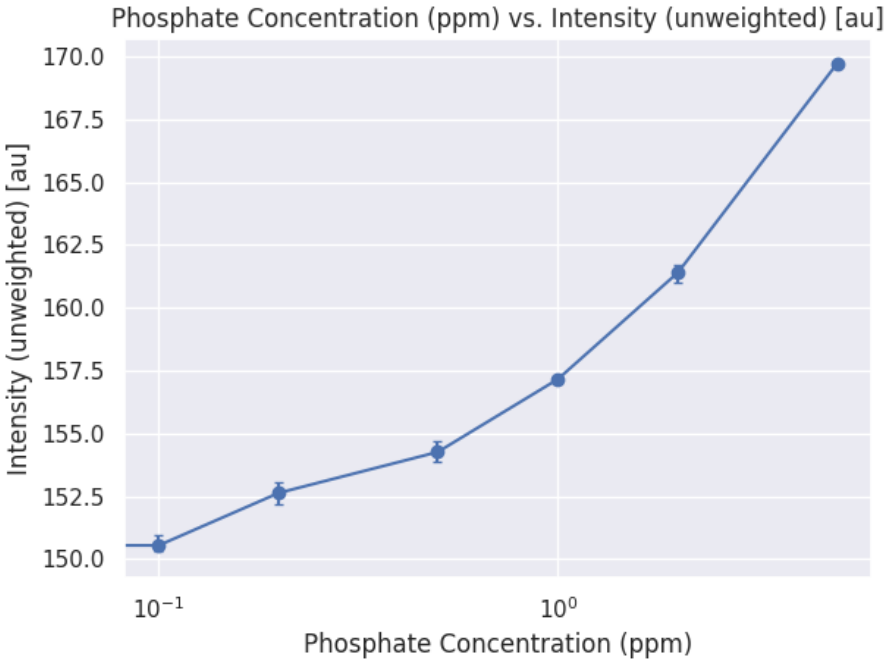

Figure 119. Infrared Imaging - Phosphate Concentration (ppm) vs. Unweighted Intensity

give the same relative changes.

The black and white property of infrared imaging renders the colorimetric optimization technique discussed in the Commercial Devices section irrelevant. Calibration curves were formed using phosphate concentration vs. red, green, blue, unweighted intensity, and weighted intensity values. As expected, they all performed the same due to no color from the visible spectrum being present.

The unweighted intensity measurements vs. phosphate concentration (ppm) are shown in Figure 119.

As shown in Figure 119, the results are extremely positive as distinct changes in intensity can be seen down to 0.1 ppm. This of course means that the method has a limit of detection of 0.2 ppm. This LOD is a very respectable result that is adequate for almost all environmental conditions. The variance for each measurement is also quite low meaning that the system is indeed suitable for commercial

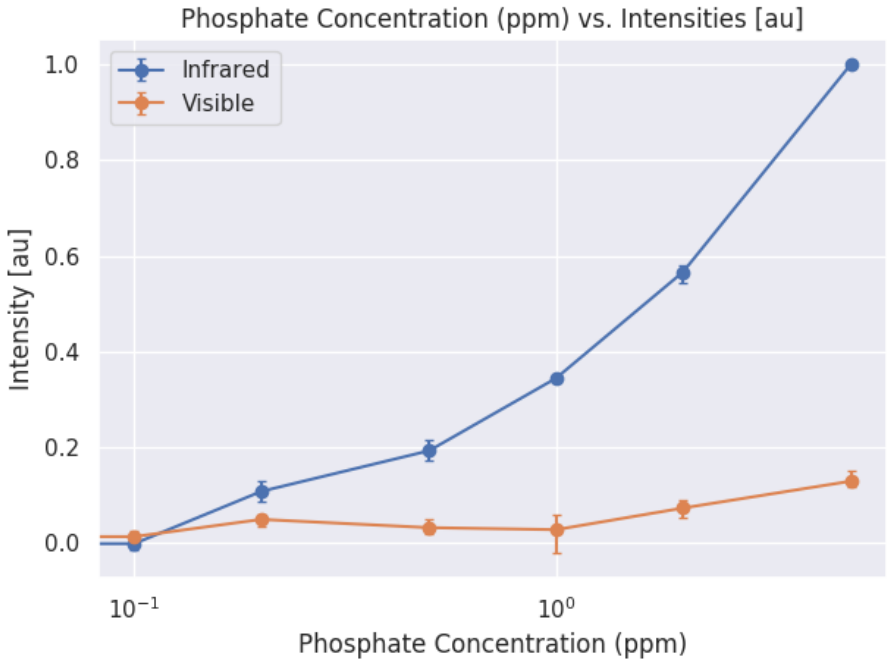

Figure 120. Infrared vs. Visible Imaging

applications. The infrared and red value measurements on the Quantofix strips were then normalized in order to directly compare them in the same plot. The plot is shown in Figure 120.

As shown in Figure 120, the difference is quite astounding. Where as the visual imaging with red intensity values has a limit of detection around 2 - 5 ppm, phosphate concentrations can still be discerned at 0.2 ppm using infrared imaging. An improvement by a factor greater than 10 was achieved.

CHAPTER 5

Conclusion

This research produced a variety of results to help advance the current state of phosphate detection. A device architecture that can mitigate handling of reagents while still offering the potential for high sensitivity was successfully built. High variability was experienced but once resolved could offer a platform that could easily compete with currently available commercial devices. The RGB app and data center developed are a highly scalable system that could improve data collection and analysis in the field. In particular, the ability to instantly quantify colorimetric measurements based on RGB values and pre-programmed calibration curves can significantly speed up detection by citizen scientists and researchers in the field. The data center provides a manner of storing data collected by users in a central database. The public data can then be used for the creation of heat maps and other useful visualizations.

The infrared box developed in this work was a great achievement as it illustrates that expensive spectrometers and sensors are not necessary for taking advantage of infrared spectra. The absorption peak of the molybdenum blue reaction in the near infrared was utilized by use of the box to significantly improve the limit of detection of a popular commercial device. Device sensitivity was improved by a factor greater than 10 from a LOD of 2 - 5 ppm to 0.2 ppm. The architecture used could easily be adapted to an inexpensive commercial platform for use in the field.

Overall this research has provided a multitude of results and ideas that help to further serve the fields of colorimetric reactions and detection.

5.1 Future Work

There is much further work that can be done on the various areas of this study. The device requires improvements to be made in terms of consistency and variability. In addition, it must be adapted to a commercially viable format. The RGB app needs several enhancements in terms of exposure and phone to phone variability. The ideas discussed in the Commercial Devices Section of the Findings chapter provides the basis for an entirely new research topic. Lastly, the infrared box can be refined for commercial use in the field.

5.1.1 Optimization of Colorimetric Detection Methods

As briefly mentioned in the Findings chapter, the colorimetric results observed in the phosphate and nitrate test strips provided an interesting direction for reducing measurement variability. The idea based on absorption spectra can be utilized to improve device sensitivity simply by changing the manner of quantification. Further work must be done to test the theory in absorption spectra where peaks are outside the red, green, and blue wavelengths. A reaction with an absorption peak in the 570 - 590 nm range could be a perfect testing ground for example as it would correspond to yellow in the electromagnetic spectrum. The yellow artificial color channel can then easily be produced by adding the red and green RGB values and dividing by 2 as yellow is (255, 255, 0) in the RGB color space.

Performance between different color channels can be measured by use of the mean squared error. The error may be calculated based on the difference between measurements taken for each concentration and the averages at each concentration. If significant improvement is witnessed, the manipulation of RGB coefficients may provide a 'free' manner of bettering sensitivity in colorimetric reactions.

5.1.2 RGB App

The RGB app has much work to be done in the consistency of results. The issues are present in large part due to errors in the camera API of the Xcode environment. It was observed that locking exposure values programmatically did not work as intended. This of course is a major problem, as the RGB values of an image is highly dependent on the camera's different settings. An update to the API would be the best solution as the code can remain as it is. A quick workaround however may be the addition of an exposure button that must be pressed prior to photo capture. This button would set the exposure values every time it is pressed.

In addition, much work must be done in the area of compatibility. All tests were performed using an iPhone 8 but must be adapted to different phones in the iOS family. Small discrepancies between different phone hardwares may result in large contrasts between measurements. As it stands the app is only available to be used in the Apple ecosystem. An android version must be written in Java as it would significantly enlarge the target population.

5.1.3 Lab-on-Chip Device

There are a variety of improvements that can be made to the lab-on-chip device. In particular, the variability witnessed during testing must be resolved in order to create a device that is both reliable and consistent. The architecture of the device will remain the same but its package must change for commercial use. A larger housing that completely contains the inside fluidics must be developed. This design should be both ergonomic and appealing to the target audience. Tests showed that the device has great promise in terms of sensitivity, these adaptations must be applied however, so that the device could succeed in the market.

5.1.4 Infrared Box

The infrared box provides an inexpensive manner for achieving high sensitivity on the molybdenum blue reaction. While the box developed in this study is both competent and easy to use, many improvements can be made in terms of its architecture and usability. As it stands, the box requires the use of a monitor, keyboard, and mouse for running the python application responsible for measurements. Headless operation of the box is possible through the use of SSH in a separate computer. This is of course simply not good enough for commercial use as it assumes that users are tech-savvy. A program may be written to interface with the Raspberry Pi and SSH in the background while the user has a high-level UI with simple functions.

A brand new architecture based on the current one could also be constructed. The new architecture may utilize an infrared camera similar to the NoIR camera, except that it would interface with a custom board developed specifically for the purpose of taking infrared measurements. This format is ideal as it would be both inexpensive and provide endless operation possibilities.

LIST OF REFERENCES

[1] N. A. of Sciences, Ed., *Clean Coastal Waters: Understanding and Reducing the Effects of Nutrient Pollution.* Washington, DC, United States of America: National Academy Press, 2000.

[2] L. E. Brand, J. Pablo, A. Compton, N. Hammerschlag, and D. C. Mash, "Cyanobacterial blooms and the occurrence of the neurotoxin, beta-n-methylamino-l-alanine (bmaa), in south florida aquatic food webs," *Harmful Algae*, vol. 9, 2010.

[3] T. N, Z. B, S. E, L. E, A. A, C. T, H. J, B. W, H. PL, and S. X, "Assessing cyanobacterial harmful algal blooms as risk factors for amyotrophic lateral sclerosis," *Neurotoxicity Research*, vol. 33, 2018.

[4] United States Environmental Protection Agency. "The mississippi/atchafalaya river basin (marb)." April 2018. [Online]. Available: https://www.epa.gov/ms-htf/mississippiatchafalaya-river-basin-marb

[5] National Oceanic and Atmospheric Administration. "Gulf of mexico 'dead zone' is the largest ever measured." April 2018. [Online]. Available: http://www.noaa.gov/media-release/gulf-of-mexico-dead-zone-is-largest-ever-measured

[6] J. Schmaltz, NASA Earth Observatory.

[7] U. S. E. P. Agency, "A compilation of cost data associated with the impacts and control of nutrient pollution," United States Environmental Protection Agency, Tech. Rep., 2015.

[8] M. Wines. The New York Times. "Behind toledo's water crisis, a long-troubled lake erie." April 2018. [Online]. Available: https://www.nytimes.com/2014/08/05/us/lifting-ban-toledo-says-its-water-is-safe-to-drink-again.html

[9] D. M. Anderson, Y. Kaoru, and A. W. White, "Estimated annual economic impacts from harmful algal blooms (habs) in the united states," Woods Hole Oceanographic Institution, Tech. Rep., 2000.

[10] S. Ara, "The influence of water quality on the demand for residential development around lake erie," Ph.D. dissertation, The Ohio State University, 2007.

[11] I. Sanseverino, D. Conduto, L. Pozzoli, S. Dobricic, and T. Lettieri, "Algal bloom and its economic impact," European Commission Joint Research Centre, Tech. Rep., 2016.

[12] L. J. Puckett, "Identifying the major sources of nutrient water pollution," *Environmental Science and Technology*, vol. 29, 1995.

[13] R. W. Howarth, A. Sharpley, and D. Walker, "Sources of nutrient pollution to coastal waters in the united states: Implications for achieving coastal water quality goals," *Estuaries*, vol. 25, 2002.

[14] N. A. of Sciences, Ed., *Managing Wastewater in Coastal Urban Areas*. Washington, DC, United States of America: National Academies Press, 1993.

[15] S. K. Moran. Scientific American. "Wastewater is key to reducing nitrogen pollution." April 2018. [Online]. Available: https://www.scientificamerican.com/article/wastewater-is-key-to-reducing-nitrogen-pollution/

[16] United States Environmental Protection Agency. "Septic systems overview." April 2018. [Online]. Available: https://www.epa.gov/septic/septic-systems-overview

[17] National Oceanic and Atmospheric Administration. "What is nutrient pollution?" May 2018. [Online]. Available: https://oceanservice.noaa.gov/facts/nutpollution.html

[18] Royal Society of Chemistry. "Phosphorus." May 2018. [Online]. Available: http://www.rsc.org/periodic-table/element/15/phosphorus

[19] B. Oram. Water Research Center. "Phosphate in surface water streams lakes." May 2018. [Online]. Available: https://www.water-research.net/index.php/phosphate-in-water

[20] D. Correll, "Phosphorus: a rate limiting nutrient in surface waters," *Poultry Science*, vol. 78, 1999.

[21] K. M. Mackenthun, Ed., *Toward a Cleaner Aquatic Environment*. Washington, DC, United States of America: Environmental Protection Agency Office of Air and Water Programs, 1973.

[22] M. D. Patey, M. J. Rijkenberg, P. J. Statham, M. C. Stinchcombe, E. P. Achterberg, and M. Mowlem, "Determination of nitrate and phosphate in seawater at nanomolar concentrations," *Trends in Analytical Chemistry*, vol. 27, 2008.

[23] J. Murphy and J. P. Riley, "A modified single solution method for the determination of phosphate in natural waters," *Analytica Chimica Acta*, vol. 27, 1962.

[24] J. Jonca, V. L. Fernández, D. Thouron, A. Paulmier, M. Gracoc, and V. Garcon, "Phosphate determination in seawater: Toward an autonomous electrochemical method," *Talanta*, vol. 87, 2011.

[25] H. N. Lee, K. M. K. Swamy, S. K. Kim, J.-Y. Kwon, Y. Kim, S.-J. Kim, Y. J. Yoon, and J. Yoon, "Simple but effective way to sense pyrophosphate and inorganic phosphate by fluorescence changes," *Organic Letters*, vol. 9, 2007.

[26] S. Islam, M. N. Reza, J.-T. Jeong, and K.-H. Lee, "Sensing technology for rapid detection of phosphorus in water: A review," *Journal of Biosystems Engineering*, vol. 41, 2016.

[27] E. M. Bartlett and D. H. Lewis, "Spectrophotometric determination of phosphate esters in the presence and absence of orthophosphate," *Analytical Biochemistry*, vol. 36, 1970.

[28] K. Itaya and M. Ui, "A new micromethod for the colorimetric determination of inorganic phosphate," *Clinica Chimica Acta*, vol. 14, 1966.

[29] Indigo Instruments. "Phosphate test strips." May 2018. [Online]. Available: https://www.indigoinstruments.com/test_strips/water_quality/phosphate-test-strips-100ppm-33817P.html

[30] Macherey-Nagel. "Quantofix phosphate test strips." May 2018. [Online]. Available: http://www.mn-net.com/Testpapers/QUANTOFIXteststrips/QUANTOFIXPhosphat/tabid/10335/language/en-US/Default.aspx

[31] ThermoFisher Scientific. "Phosphate sensor: Pv4406." May 2018. [Online]. Available: https://www.thermofisher.com/order/catalog/product/PV4406

[32] H. Chen, J. Cogswell, C. Anagnostopoulos, and M. Faghri, "A fluidic diode, valves, and a sequential-loading circuit fabricated on layered paper," *Lab on a Chip*, vol. 12, 2012.

[33] K. Pitchaimani, B. C. Sapp, A. Winter, A. Gispanski, T. Nishida, and Z. H. Fan, "Manufacturable plastic microfluidic valves using thermal actuation," *Lab on a Chip*, vol. 21, 2009.

[34] G. A. Posthuma-Trumpie, J. Korf, and A. van Amerongen, "Lateral flow (immuno)assay: its strengths, weaknesses, opportunities and threats. a literature survey," *Analytical and Bioanalytical Chemistry*, vol. 393, 2009.

[35] "Rapid lateral flow test strips: Considerations for product development," EMD Millipore.

[36] P. Abgrall and A.-M. Gué, "Lab-on-chip technologies: making a microfluidic network and coupling it into a complete microsystem—a review," *Journal of Micromechanics and Microengineering*, vol. 17, 2007.

[37] science photo. Shutterstock. "photo id: 311155133." May 2018. [Online]. Available: https://www.shutterstock.com/image-photo/lab-on-chip-device-integrates-several-311155133?src=cLdu2ev8R_VMau9l2tqYCw-1-3

[38] B. Jayawardane, I. D. McKelvie, and S. D. Kolev, "A paper-based device for measurement of reactive phosphate in water," *Talanta*, vol. 100, 2012.

[39] B. M. Jayawardane, W. Wongwilai, K. Grudpan, S. D. Kolev, M. W. Heaven, D. M. Nash, and I. D. McKelvie, "Evaluation and application of a paper-based device for the determination of reactive phosphate in soil solution," *Journal of Environmental Quality*, vol. 43, 2014.

[40] G. Denigès, *C. R. Acad. Sci.*, vol. 171, 1920.

[41] L. Drummond and W. Maher, "Determination of phosphorus in aqueous solution via formation of the phosphoantimonylmolybdenum blue complex re-examination of optimum conditions for the analysis of phosphate," *Analytica Chimica Acta*, vol. 302, 1995.

[42] K. I. Aspila, H. Agemian, and A. S. Y. Chau, "A semi-automated method for the determination of inorganic, organic and total phosphate in sediments," *Analyst*, vol. 101, 1976.

[43] Z. He and C. W. Honeycutt, "A modified molybdenum blue method for orthophosphate determination suitable for investigating enzymatic hydrolysis of organic phosphates," *Communications in Soil Science and Plant Analysis*, vol. 36, 2005.

[44] K. L. Linge and C. E. Oldham, "Interference from arsenate when determining phosphate by the malachite green spectrophotometric method," *Analytica Chimica Acta*, vol. 450, 2001.

[45] T. Ohno and L. M. Zibilske, "Determination of low concentrations of phosphorus in soil extracts using malachite green," *Soil Science Society of America*, vol. 55, 1991.

[46] S. Motomizu, M. Oshima, and Y. Ojima, "Spectrophotometric determination of silicate in water with molybdate and malachite green," *Analytical Sciences*, vol. 5, 1989.

[47] G. Misson, *Chemiker Zeitung*, vol. 32, 1908.

[48] O. B. Michelsen, "Photometric determination of phosphorus as molybdovanadophosphoric acid," *Analytical Chemistry*, vol. 29, 1957.

[49] E. M. Bartlett and D. H. Lewis, "Spectrophotometric determination of phosphate esters in the presence and absence of orthophosphate," *Analytical Biochemistry*, vol. 36, 1970.

[50] J. Jonca, V. L. Fernández, D. Thouron, A. Paulmier, M. Graco, and V. Garçon, "Phosphate determination in seawater: Toward an autonomous electrochemical method," *Talanta*, vol. 87, 2011.

[51] J. Jonca, W. Giraud, C. Barus, M. Comtat, N. S. D. Thouron, and V. Garçon, "Reagentless and silicate interference free electrochemical phosphate determination in seawater," *Electrochimica Acta*, vol. 88, 2013.

[52] J.-Z. Zhang, C. J. Fischer, and P. B. Ortner, "Optimization of performance and minimization of silicate interference in continuous flow phosphate analysis," *Talanta*, vol. 49, 1998.

[53] S. Cinti, D. Talarico, G. Palleschi, D. Moscone, and F. Arduini, "Novel reagentless paper-based screen-printed electrochemical sensor to detect phosphate," *Analytica Chimica Acta*, vol. 919, 2016.

[54] H. X. Zhao, L. Q. Liu, Z. D. Liu, Y. Wang, X. J. Zhao, and C. Z. Huang, "Highly selective detection of phosphate in very complicated matrixes with an off–on fluorescent probe of europium-adjusted carbon dots," *Chemical Communications*, vol. 47, 2011.

[55] J. Hoffmann, D. Mark, S. Lutz, R. Zengerle, and F. von Stetten, "Pre-storage of liquid reagents in glass ampoules for dna extraction on a fully integrated lab-on-a-chip cartridge," *Lab on a Chip*, vol. 10, 2010.

[56] D. Czurratis, Y. Beyl, S. Zinober, R. Zengerle, and F. Lärmer, "Long-term on-chip storage and release of liquid reagents for diagnostic lab-on-a-chip applications," *International Journal of Physical and Mathematical Sciences*, vol. 7, 2013.

[57] K. Abi-Samra, R. Hanson, M. Madou, and R. A. G. III, "Infrared controlled waxes for liquid handling and storage on a cd-microfluidic platform," *Lab on a Chip*, vol. 11, 2011.

[58] D. K. Bwambok, D. C. Christodouleas, S. A. Morin, H. Lange, S. T. Phillips, and G. M. Whitesides, "Adaptive use of bubble wrap for storing liquid samples and performing analytical assays," *Analytical Chemistry*, vol. 86, 2014.

[59] X. Li, J. Tian, T. Nguyen, and W. Shen, "Paper-based microfluidic devices by plasma treatment," *Analytical Chemistry*, vol. 80, 2008.

[60] K. N. Han, J.-S. Choi, and J. Kwon, "Three-dimensional paper-based slip device for one-step point-of-care testing," *Scientific Reports*, vol. 6, 2016.

[61] H. Noh and S. T. Phillips, "Metering the capillary-driven flow of fluids in paper-based microfluidic devices," *Analytical Chemistry*, vol. 82, 2010.

[62] B. Lutz, T. Liang, E. Fu, S. Ramachandran, P. Kauffman, and P. Yager, "Dissolvable fluidic time delays for programming multi-step assays in instrument-free paper diagnostics," *Lab on a Chip*, vol. 13, 2013.

[63] Y. . Lai, J. . Tsai, J. . Hsu, and Y. . Lu, "Automated paper-based devices by microfluidic timing-valve for competitive elisa," in *2017 IEEE 30th International Conference on Micro Electro Mechanical Systems (MEMS)*, 2017.

[64] C. K. W. Koo, F. He, and S. R. Nugen, "An inkjet-printed electrowetting valve for paper-fluidic sensors," *Analyst*, vol. 138, 2013.

[65] X. Li, P. Zwanenburg, and X. Liu, "Magnetic timing valves for fluid control in paper-based microfluidics," *Lab on a Chip*, vol. 13, 2013.

[66] T. Kong, S. Flanigan, M. Weinstein, U. Kalwa, C. Legner, and S. Pandey, "A fast, reconfigurable flow switch for paper microfluidics based on selective wetting of folded paper actuator strips," *Lab on a Chip*, vol. 17, 2017.

[67] J. B. Knight, A. Vishwanath, J. P. Brody, and R. H. Austin, "Hydrodynamic focusing on a silicon chip: Mixing nanoliters in microseconds," *Physical Review Letters*, vol. 80, 1998.

[68] R. H. Liu, M. A. Stremler, K. V. Sharp, M. G. Olsen, J. G. Santiago, R. J. Adrian, H. Aref, and D. J. Beebe, "Passive mixing in a three-dimensional serpentine microchannel," *Journal of Microelectromechanical Systems*, vol. 9, 2000.

[69] R. H. Liu, J. Yang, R. Lenigk, J. Bonanno, and P. Grodzinski, "Self-contained, fully integrated biochip for sample preparation, polymerase chain reaction amplification, and dna microarray detection," *Analytical Chemistry*, vol. 76, 2004.

[70] A. R. Rezk, A. Qi, J. R. Friend, W. H. Li, and L. Y. Yeo, "Uniform mixing in paper-based microfluidic systems using surface acoustic waves," *Lab on a Chip*, vol. 12, 2012.

[71] E. W. Washburn, "The dynamics of capillary flow," *The Physical Review*, vol. 17, 1921.

[72] R. Lucas, "Ueber das zeitgesetz des kapillaren aufstiegs von flüssigkeiten," *Colloid and Polymer Science*, vol. 23, 1918.

[73] H. Darcy, *Les Fontaines Publiques de la Ville de Dijon*, 1856.

[74] E. Fu, S. A. Ramsey, P. Kauffman, B. Lutz, and P. Yager, "Transport in two-dimensional paper networks," *Microfluidics and Nanofluidics*, vol. 10, 2011.

[75] Brigham Young University. "Regions of the electromagnetic spectrum." January 2019. [Online]. Available: https://www.physics.byu.edu/faculty/christensen/physics%20137/Figures/Energy/Regions%20of%20the%20Electromagnetic%20Spectrum.htm

[76] E. Fest, *Stray Light Analysis and Control*. SPIE Press, 2013, ch. 2.

[77] D. Swinehart, "The beer-lambert law," *Journal of Chemical Education*, vol. 39, 1962.

[78] N. A. Ibraheem, M. M. Hasan, R. Z. Khan, and P. K. Mishra, "Understanding color models: A review," *ARPN Journal of Science and Technology*, vol. 2, 2012.

[79] Appalachian State University. "Spectral sensitivity of photoreceptors." January 2019. [Online]. Available: http://www.appstate.edu/~steelekm/classes/psy3215/Color/absorption_spectrum.jpg

[80] Edmund Optics. "Imaging electronics 101: Understanding camera sensors for machine vision applications." January 2019. [Online]. Available: https://www.edmundoptics.com/resources/application-notes/imaging/understanding-camera-sensors-for-machine-vision-applications/

[81] B. E. Bayer, United States of America Patent US3 971 065A, 1975.

[82] Nikon. "Understanding maximum aperture." January 2019. [Online]. Available: https://www.nikonusa.com/en/learn-and-explore/a/tips-and-techniques/understanding-maximum-aperture.html

[83] Photography Life. "Introduction to shutter speed in photography." January 2019. [Online]. Available: https://photographylife.com/what-is-shutter-speed-in-photography

[84] Nikon. "Understanding iso sensitivity." January 2019. [Online]. Available: https://www.nikonusa.com/en/learn-and-explore/a/tips-and-techniques/understanding-iso-sensitivity.html

[85] PetaPixel. "The exposure triangle: Making sense of aperture, shutter speed, and iso." January 2019. [Online]. Available: https://petapixel.com/2017/03/25/exposure-triangle-making-sense-aperture-shutter-speed-iso/

[86] Nikon. "Setting white balance." January 2019. [Online]. Available: https://www.nikonusa.com/en/learn-and-explore/a/tips-and-techniques/setting-white-balance.html

[87] Envato. “How to use white balance creatively.” January 2019. [Online]. Available: https://photography.tutsplus.com/articles/how-to-use-white-balance-creatively--photo-9121

[88] Autodesk. “Inventor.” November 2018. [Online]. Available: https://www.autodesk.com/products/inventor/overview

[89] ELEDLIGHTS.com. “A quick guide to lighting-related color temperatures.” November 2018. [Online]. Available: https://www.eledlights.com/blog/post/a-quick-guide-to-lighting-color-temperature/

[90] LEDsupply. “Waterproof ip65 led flex strip.” November 2018. [Online]. Available: https://www.ledsupply.com/led-strips/waterproof-12v-led-strip

[91] raise3d. “Raise3d n2 plus.” November 2018. [Online]. Available: https://www.raise3d.com/pages/raise3d-n2-plus

[92] raise3d. “ideamaker.” November 2018. [Online]. Available: https://www.raise3d.com/pages/ideamaker

[93] National Institutes of Health. “Imagej.” September 2018. [Online]. Available: https://imagej.nih.gov/ij/

[94] Apple. “Swift 4.” December 2018. [Online]. Available: https://developer.apple.com/swift/

[95] Apple. “Xcode 10.” December 2018. [Online]. Available: https://developer.apple.com/xcode/

[96] CocoaPods. “Cocoapods.” December 2018. [Online]. Available: https://cocoapods.org/

[97] GitHub. “Alamofire.” December 2018. [Online]. Available: https://github.com/Alamofire/Alamofire

[98] GitHub. “Swiftyjson.” December 2018. [Online]. Available: https://github.com/SwiftyJSON/SwiftyJSON

[99] GitHub. “Charts.” December 2018. [Online]. Available: https://github.com/danielgindi/Charts

[100] OpenWeatherMap. “Weather api.” December 2018. [Online]. Available: https://openweathermap.org/api

[101] Flask. “Flask.” December 2018. [Online]. Available: http://flask.pocoo.org/

[102] Bootstrap. “Bootstrap.” December 2018. [Online]. Available: https://getbootstrap.com/

[103] CorelDRAW. "Coreldraw." December 2018. [Online]. Available: https://www.coreldraw.com/en/

[104] Affinity Designer. "Affinity designer." December 2018. [Online]. Available: https://affinity.serif.com/en-us/designer/

[105] Raspberry Pi. "Raspberry pi 3 model b+." February 2019. [Online]. Available: https://www.raspberrypi.org/products/raspberry-pi-3-model-b-plus/

[106] Raspberry Pi. "Pi noir camera v2." February 2019. [Online]. Available: https://www.raspberrypi.org/products/pi-noir-camera-v2/

[107] Raspberry Pi. "Raspbian." February 2019. [Online]. Available: https://www.raspberrypi.org/downloads/raspbian/

[108] Thonny. "Thonny." February 2019. [Online]. Available: https://thonny.org/

[109] Thingiverse. "Raspberry pi 3 (b/b+), pi 2 b, and pi 1 b+ case with vesa mounts and more." February 2019. [Online]. Available: https://www.thingiverse.com/thing:922740

[110] Everlight. "Technical data sheet 5mm infrared led, t-1 3/4." February 2019. [Online]. Available: http://www.everlight.com/file/ProductFile/201407061534026941.pdf

[111] Read the Docs - Pi Camera. "Advanced recipes." February 2019. [Online]. Available: https://picamera.readthedocs.io/en/release-1.12/recipes2.html#raw-bayer-data-captures

[112] M. Irandoust, M. Shariati-Rad, and M. Haghighi, "Nitrite determination in water samples based on a modified griess reaction and central composite design," *Analytical Methods*, vol. 21, 2013.

[113] E. Evans, E. F. M. Gabriel, W. K. T. Coltro, and C. D. Garcia, "Rational selection of substrates to improve color intensity and uniformity on microfluidic paper-based analytical devices," *Analyst*, vol. 139, 2014.

[114] N. Walji and B. D. MacDonald, "Influence of geometry and surrounding conditions on fluid flow in paper-based devices," *Micromachines*, vol. 7, 2016.

APPENDIX A

Paper Flow Rate Experiments

The study detailed below evaluated flow rates on a paper-based device while varying paper types, channel widths, and suppliers. The objective of this study was to determine what factors significantly affect the flow in these devices. This knowledge was used to develop and improve the paper-based designs presented in this thesis.

A.1 Test Specimen

The test specimen was designed as a lateral flow strip such as a pregnancy test. The specimen and its dimensions are shown in Figures A.121 and A.122 respectively.

A.2 Procedure

Many factors affect the flow rate of microfluidic paper-based devices. Three factors were narrowed down as the most important to investigate in this study. Those factors are: paper type, channel width, and supplier. Supplier was considered as a blocking factor for this experiment. Three levels were considered for each

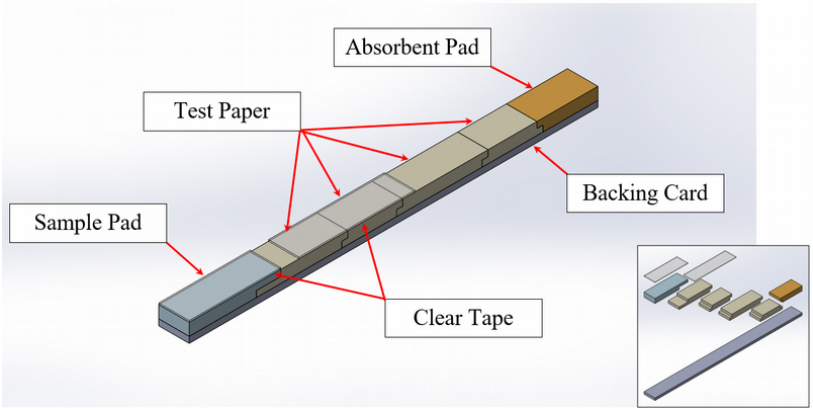

Figure A.121. Test Specimen

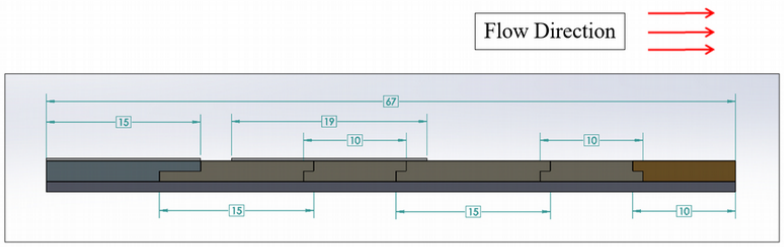

Figure A.122. Test Specimen Dimensions

factor. Whatman grades 1, 4, and 41 were considered for paper types while widths of 6, 8, and 10 mm were considered for channel width. Three different suppliers were also used in the design where each supplier manufactured their respective test devices to be run. A two factor factorial design with one blocking factor was used for this study. The fixed effects statistical model for this design is shown below in Equation A.1:

$$y_{ijk} = \mu + \tau_i + \beta_j + (\tau\beta)_{ij} + \delta_k + \epsilon_{ijk}$$

Equation A.1

The overall mean in this model is μ. τ_i is the factor effect due to the paper type while β_j is the factor effect due to the channel width. $(\tau\beta)_{ij}$ is then the interaction between the paper type and channel width factors in this case. δ_k is the effect due to the block of supplier. Finally ϵ_{ijk} is the random error component. The runs in this design were randomized within blocks as the blocks present a restriction on randomization. The experimental matrix for this design is shown below in Figure A.123.

The experimental procedure was as follows:

1. Each supplier constructed their various devices with all configurations needed for the tests as shown in Figure A.124 below

Operator	1			2			3		
Paper Type	1	4	41	1	4	41	1	4	41
Width (mm) 6									
8									
10									

Figure A.123. Experimental Matrix

Figure A.124. Manufacturing Process

2. Tests were then performed based on the randomized run order generated by Minitab

3. The operator would dip the strip up to the black line in a beaker of green colored fluid for five seconds. A second person would time the operator and signify when to pull the strip when the five seconds have elapsed.

4. The strip was then placed on a hydrophobic surface and the time it took the fluid to reach the waste pad at the end of the strip was measured as shown in Figure A.125. This time will be the response variable.

5. Steps 3 and 4 were then repeated until all tests were completed.

ANOVA was performed using Minitab after all the test runs were completed. The ANOVA table was used to determined which factors and interactions were significant in the design. Main effects plots and interaction plots were also used to determine the fastest and slowest configurations among the various parameters.

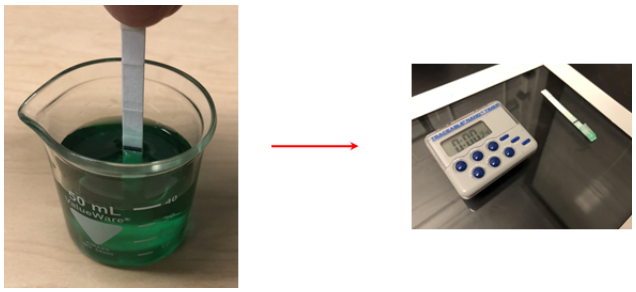

Figure A.125. Test Process

Supplier	1			2			3		
Paper Type	1	4	41	1	4	41	1	4	41
Width (mm)	296	214	149	289	181	135	275	167	111
6	289	201	138	286	175	127	258	175	110
	331	208	135	262	180	127	262	181	110
8	310	191	121	255	180	120	253	182	122
	309	202	114	258	169	110	242	168	108
	291	202	129	242	167	116	241	173	102
10	253	199	118	262	179	118	231	183	109
	258	184	113	246	181	116	244	166	100
	285	192	116	257	158	122	272	158	93

Figure A.126. Experimental Data

A.3 Results

The experimental data is shown in Figure A.126 below. All analyses were performed with a significance level α of 0.05. The ANOVA table for the data is shown below in Figure A.127.

As shown above in Figure A.127, all three factors, paper type, channel width, and supplier were shown to be significant while the interaction between paper type and channel width was not. Unfortunately, the lack of fit was very significant with a p-value of 0.006. This signifies that there were interactions present between the supplier (block) and the other two factors, paper type and channel width. It is quite clear from the ANOVA table that assuming the supplier to be a block was incorrect and it should in fact be considered as another factor in the experiment.

Analysis of Variance

Source	DF	Seq SS	Contribution	Adj SS	Adj MS	F-Value	P-Value
Paper Type	2	308783	92.33%	308783	154392	1099.67	0.000
Width	2	4007	1.20%	4007	2004	14.27	0.000
Block	2	11058	3.31%	11058	5529	39.38	0.000
Paper Type*Width	4	740	0.22%	740	185	1.32	0.272
Error	70	9828	2.94%	9828	140		
Lack-of-Fit	16	4220	1.26%	4220	264	2.54	0.006
Pure Error	54	5608	1.68%	5608	104		
Total	80	334416	100.00%				

= Significant

Figure A.127. ANOVA Table - Supplier as Block

Since the runs in the experiment were completely randomized from the start, the model could simply be changed in Minitab to include the interactions with the supplier. The ANOVA table for this modified design is shown below in Figure A.128.

There is no lack of fit present in the ANOVA for this case. The table shows that all three factors i.e. paper type, channel width, and supplier are significant. In addition, the interaction between paper type and supplier and the interaction between width and supplier were also shown to be significant.

The normal probability plot of the residuals is shown below in Figure A.129.

The various residual plots of residuals vs. fitted values, residuals vs. main factors, residuals vs. response, and residuals vs. run order are shown below in Figures A.130 - A.135.

The power curve obtained for three levels of each factor with a standard deviation of 10 and maximum difference between sample means of 30 is shown below in Figure A.136.

The main effects plots are shown below in Figure A.137.

The interaction plots are shown below in Figure A.138.

Analysis of Variance

Source	DF	Seq SS	Contribution	Adj SS	Adj MS	F-Value	P-Value
Supplier	2	11058	3.31%	11058	5529	53.24	0.000
Paper Type	2	308783	92.33%	308783	154392	1486.65	0.000
Width	2	4007	1.20%	4007	2004	19.29	0.000
Supplier*Paper Type	4	1842	0.55%	1842	460	4.43	0.004
Supplier*Width	4	1185	0.35%	1185	296	2.85	0.032
Paper Type*Width	4	740	0.22%	740	185	1.78	0.146
Supplier*Paper Type*Width	8	1194	0.36%	1194	149	1.44	0.203
Error	54	5608	1.68%	5608	104		
Total	80	334416	100.00%				

= Significant

Figure A.128. ANOVA Table - Supplier as Factor

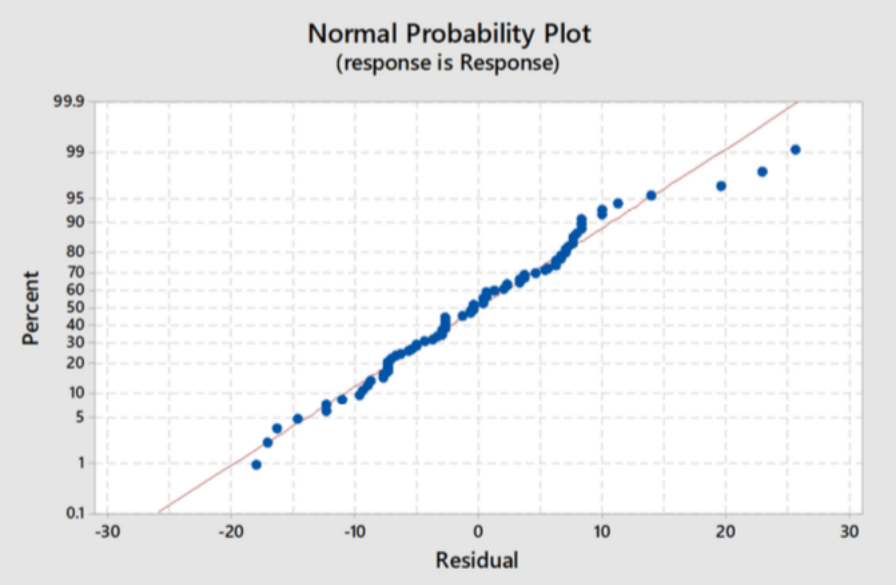

Figure A.129. Normal Probability Plot

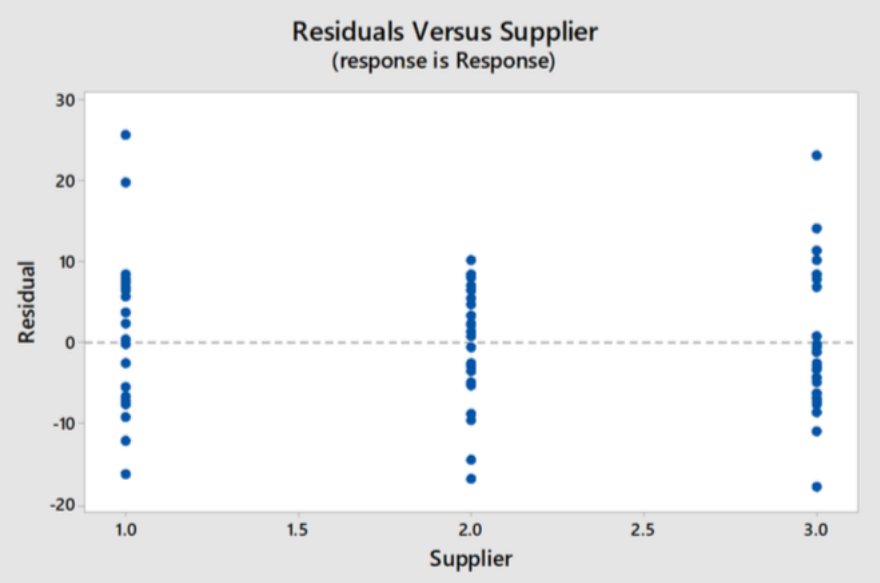

Figure A.130. Residuals vs. Supplier

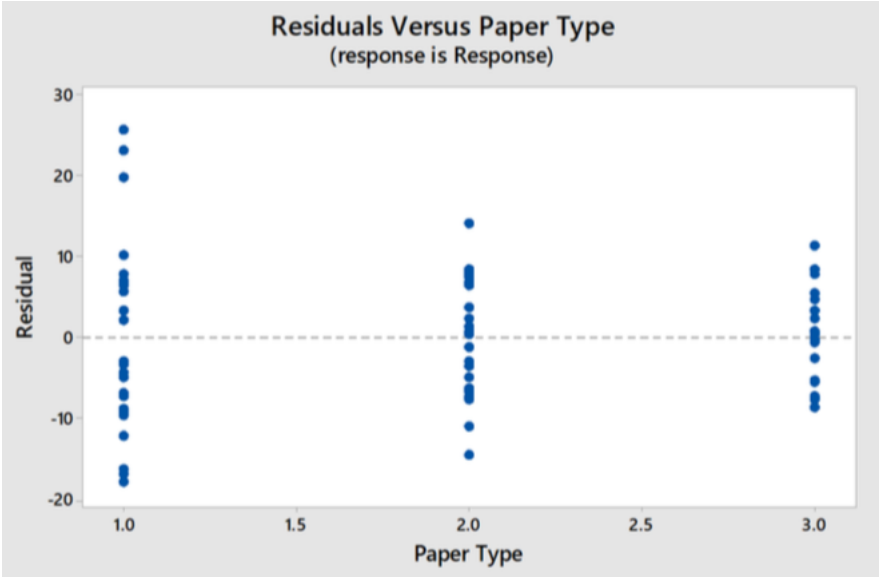

Figure A.131. Residuals vs. Paper Type

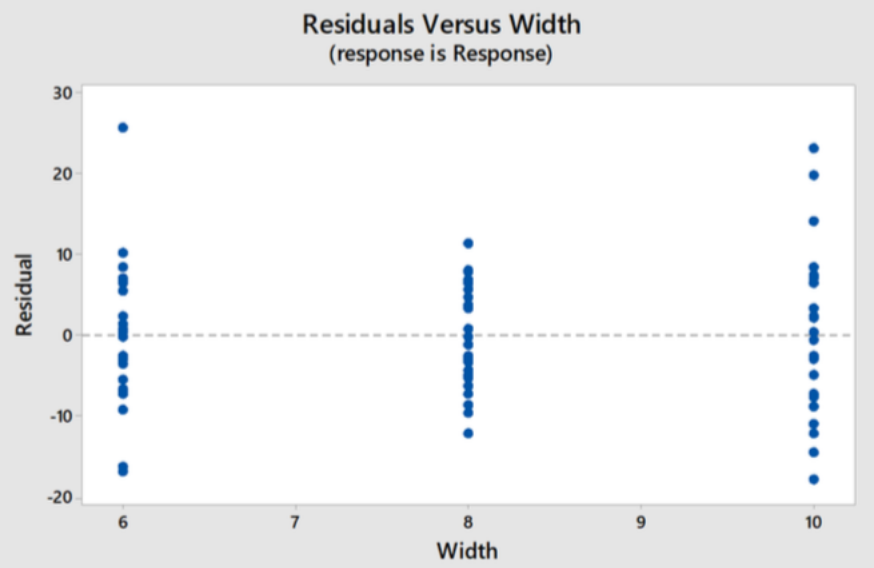

Figure A.132. Residuals vs. Channel Width

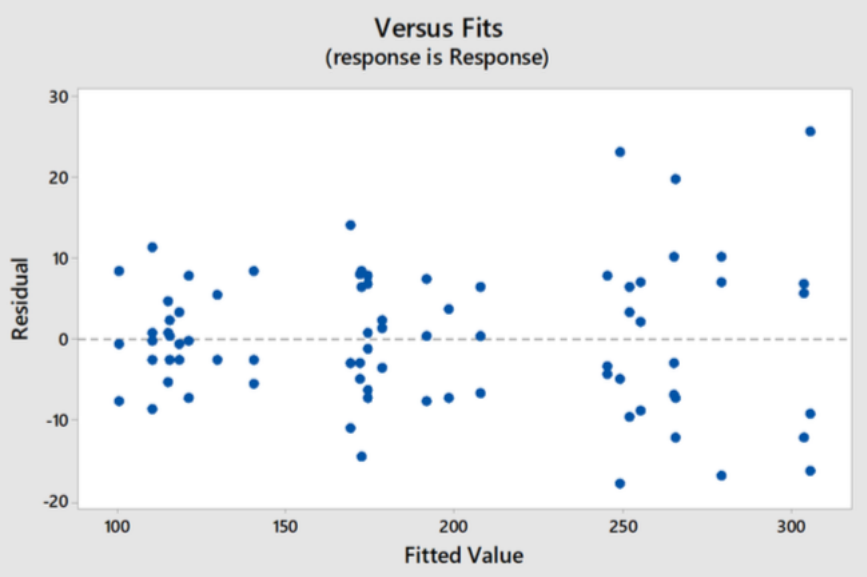

Figure A.133. Residuals vs. Fits

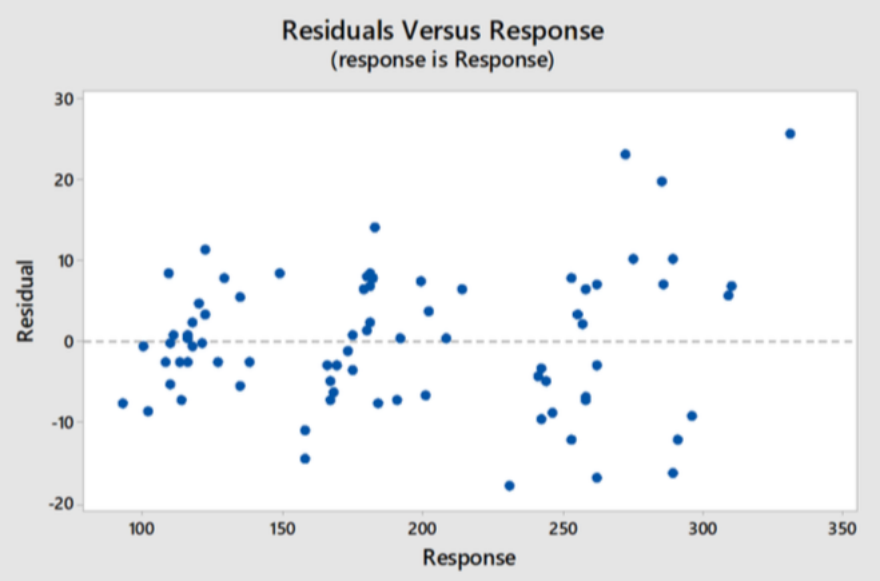

Figure A.134. Residuals vs. Response

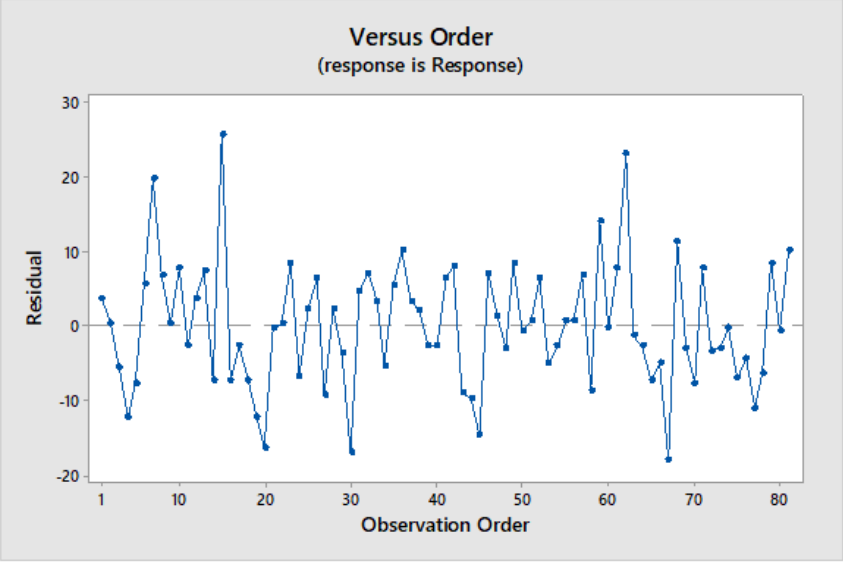

Figure A.135. Residuals vs. Run Order

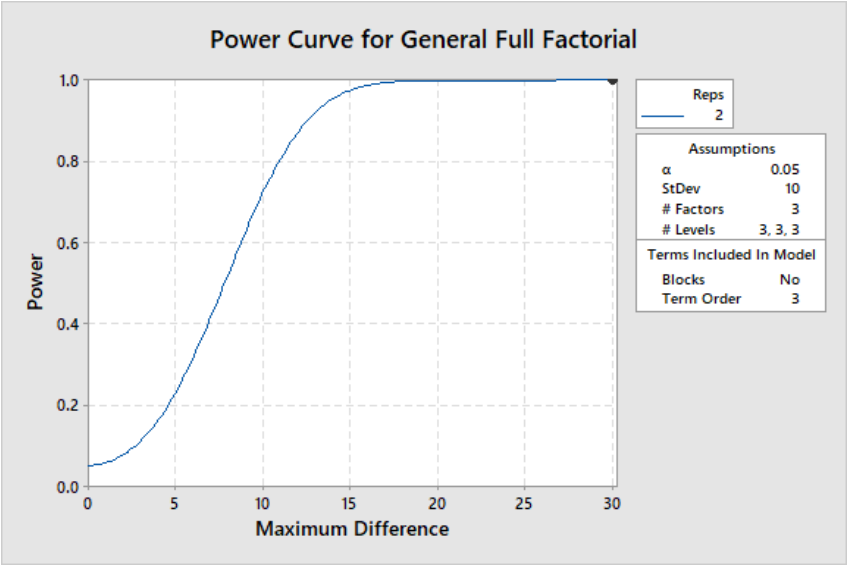

Figure A.136. Power Curve

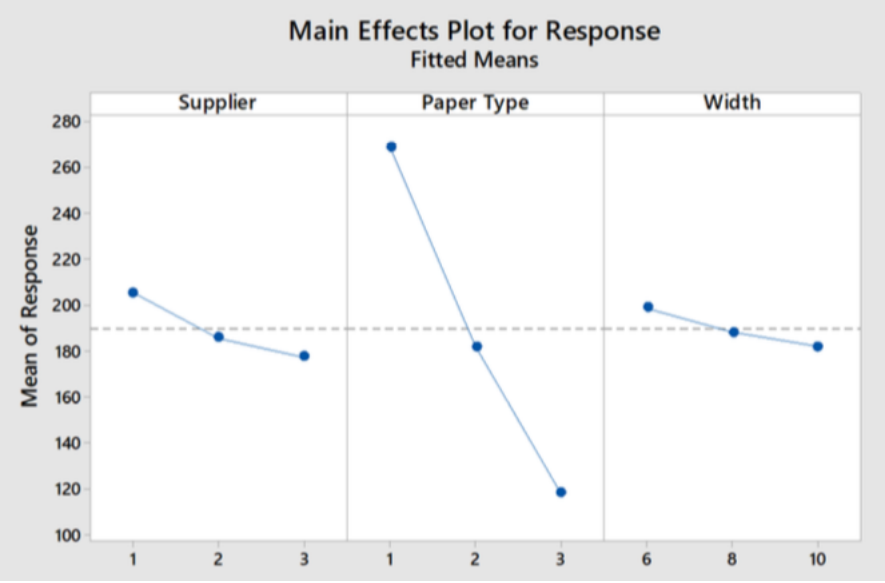

Figure A.137. Main Effects Plot

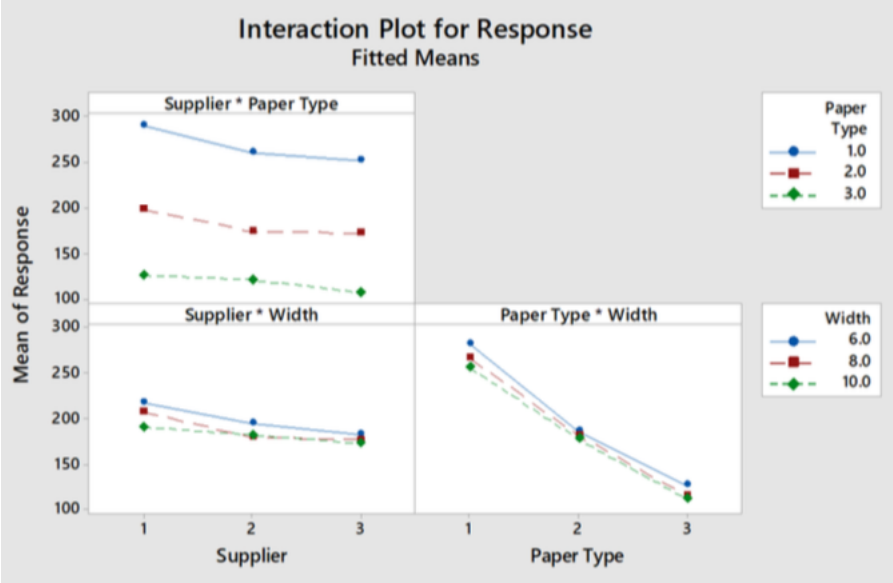

Figure A.138. Interaction Plot

A.4 Discussion

The first ANOVA table showed that the lack of fit was very significant with a p-value of 0.006. As mentioned in the results, this signified that it was incorrect to assume that supplier should be treated as a block. A second ANOVA was performed with the supplier treated as a factor instead of a block. The results showed that all three factors, paper type, channel width, and supplier were significant. The interaction between paper type and supplier and the interaction between channel width and supplier were also shown to be significant. This result was to be expected as the suppliers were responsible for the manufacturing of all of their respective test devices. As such, the effects experienced by channel width and paper type should also depend on each supplier's respective technique and skill in the manufacturing of the devices.

The normal probability plot of the residuals appeared to be quite satisfactory with the vast majority of the points lying along the line. The other various residual plots of residuals vs. fitted values, residuals vs. main factors, residuals vs.

response, and residuals vs. run order were also shown to be adequate. As shown in Figure A.136, the power sample curve reaches a power greater than 90% with a sample size of two and maximum difference between means of 15. This power level is more than satisfactory. It is then safe to assume that no normality assumptions were broken in the experiment and that the number of replicates were suitable. As such the model used in this design was found to be undoubtedly adequate.

The main effects plot showed that Whatman Grade 41 paper was the fastest along with the largest channel width of 10 mm. The plot also showed that Whatman Grade 1 paper was the slowest along with the smallest channel width of 6 mm. The interaction plots agreed with the results found in the main effects plot for the fastest and slowest configurations. The fastest configuration was found to be Whatman Grade 41 paper, 10 mm channel width, and supplier 3 (Wayne). The slowest configuration was found to be Whatman Grade 1 paper, 6 mm channel width, and supplier 1 (Amer).

These results confirm what was expected when running this study. Supplier was expected to be significant since assembly of cards and cutting of test devices were all done manually. The majority of overlaps between different sections on the card were 1 mm as can be seen below in Figure A.139 which meant that the tolerance for error while building the cards was very small. The interaction can be explained since individual suppliers will have a different application while building and cutting the card.

Dependence of flow rate on channel width confirms to previously published results [113] [114] showing that flow rate is faster for wider channels as can be seen below in Figures A.140 and A.141.

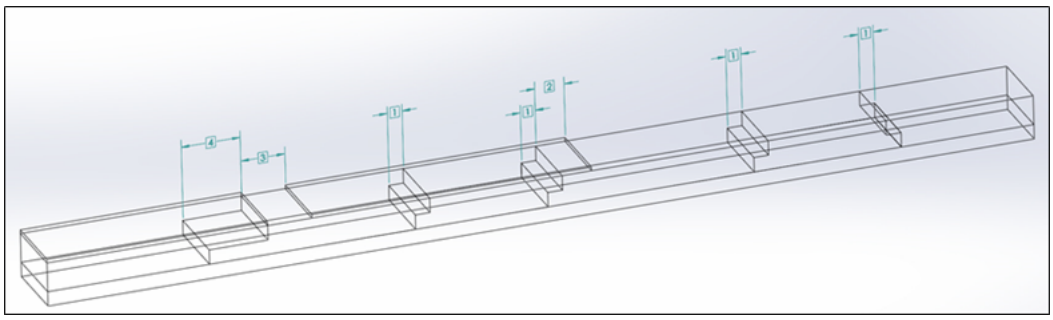

Figure A.139. Specimen Overlap Sections

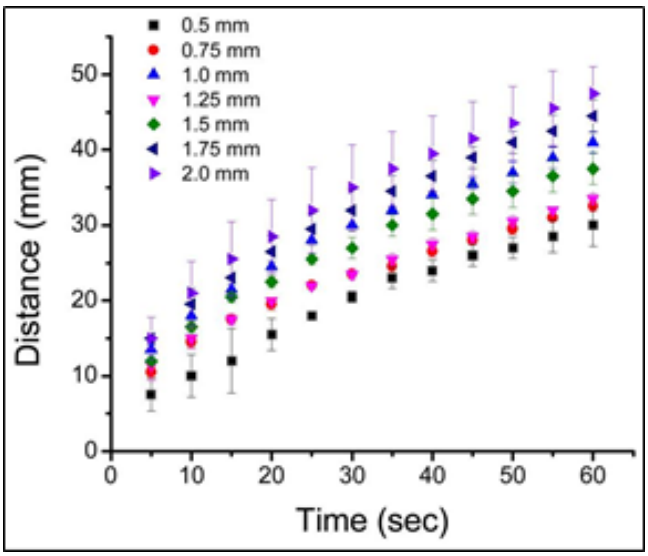

Figure A.140. Flow Rate for Grade 1 Paper, 0.5 - 2.0 mm Widths [113]

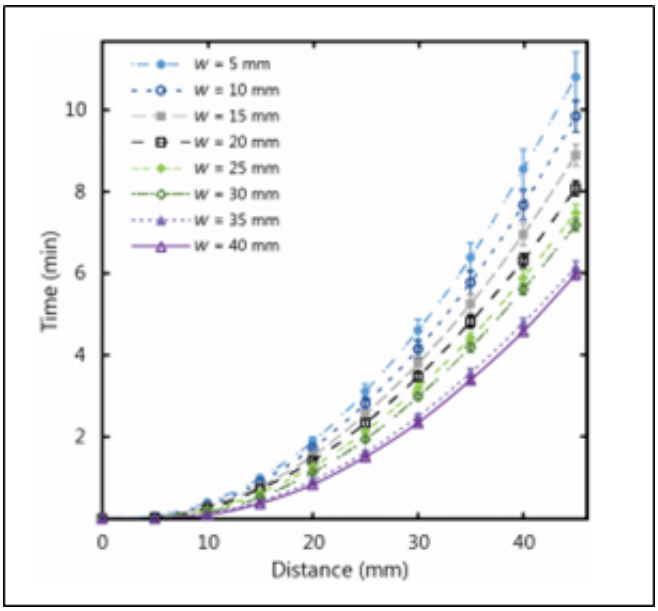

Figure A.141. Flow Rate for Grade 1 Paper, 5 - 40 mm Widths [114]

A.5 Conclusion and Recommendations

The supplier was shown to be significant and had significant interactions as well. It had to be considered as a factor instead of a block. All main factors: paper type, channel width, and supplier are significant. The interactions between paper type/supplier and channel width/supplier are also significant. Whatman Grade 41 paper with 10 mm channel width had the fastest flow rate. Whatman Grade 1 paper with 6 mm channel width had the slowest flow rate.

The desired flow rate for a given application dictates which configuration is best suited for a particular paper-based device. It may be desirable to achieve fast flow rates in some devices in order to have a rapid test while slow flow rates may be desirable in others due to functional and binding requirements between different analytes and their respective binding molecules. Whatman Grade 1 paper may then be a great candidate for timing channels used to slow down flow while Whatman Grade 41 paper would be most suited for rapid test devices.

APPENDIX B

Light Box Schematics

Schematics and drawings for the light box are shown in this appendix. All dimensions and sizes are in mm.

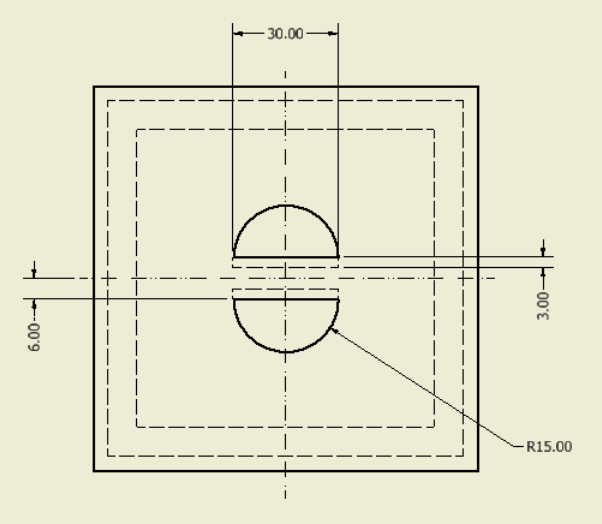

Figure B.142. Platform - Bottom

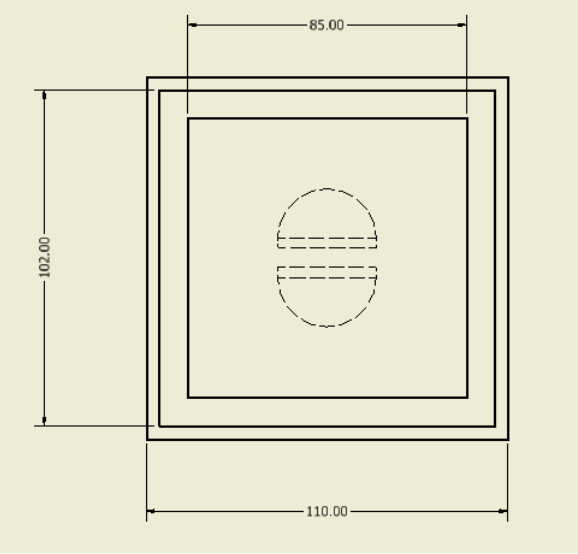

Figure B.143. Platform - Top

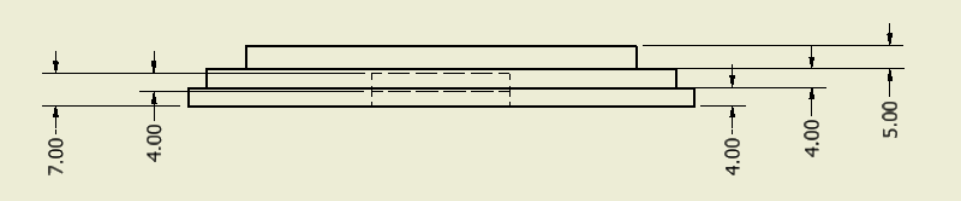

Figure B.144. Platform - Side

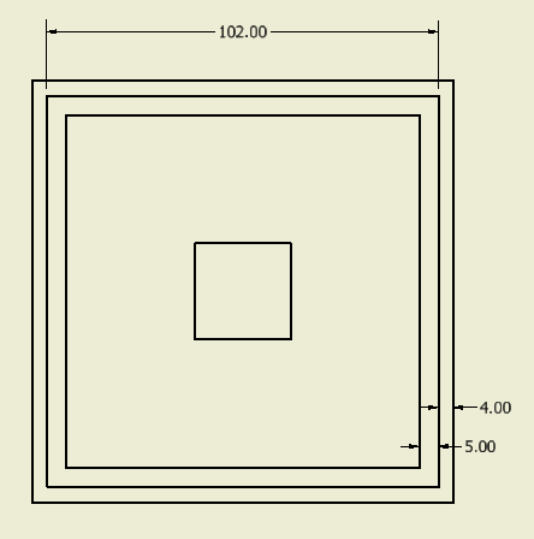

Figure B.145. Top Cover - Bottom

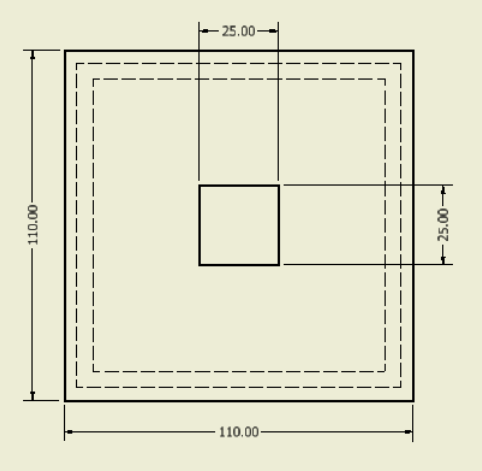

Figure B.146. Top Cover - Top

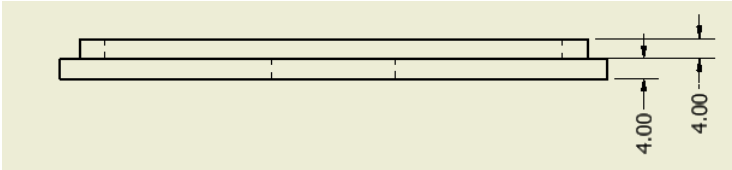

Figure B.147. Top Cover - Side

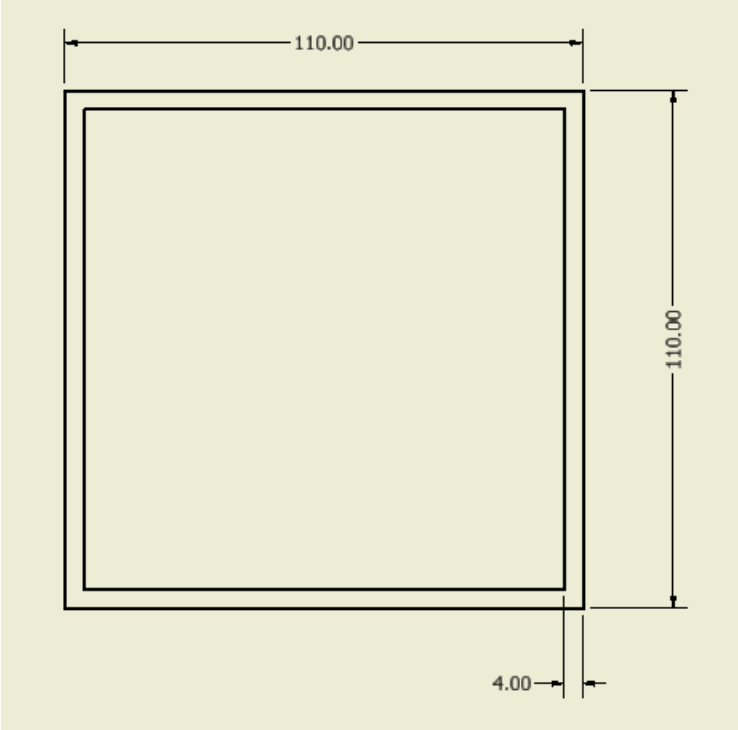

Figure B.148. Sleeve - Top

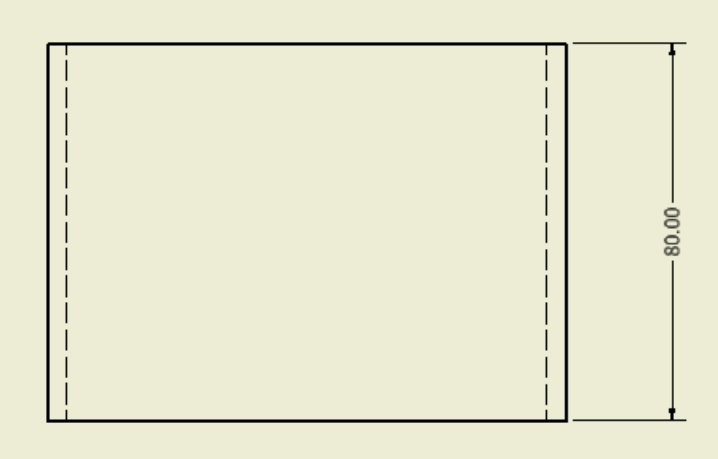

Figure B.149. Sleeve - Side

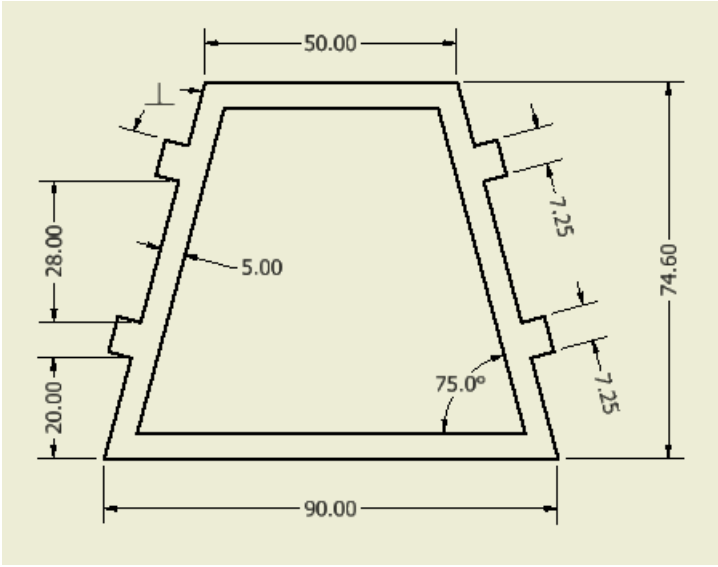

Figure B.150. Male Pyramid - Front

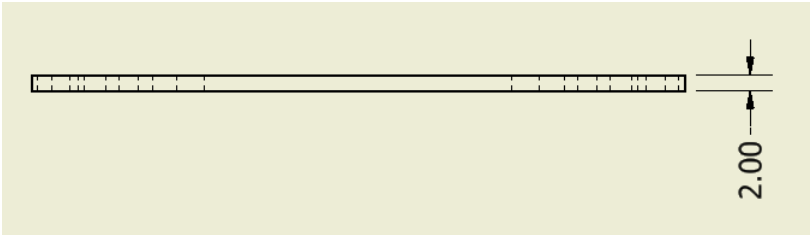

Figure B.151. Male Pyramid - Side

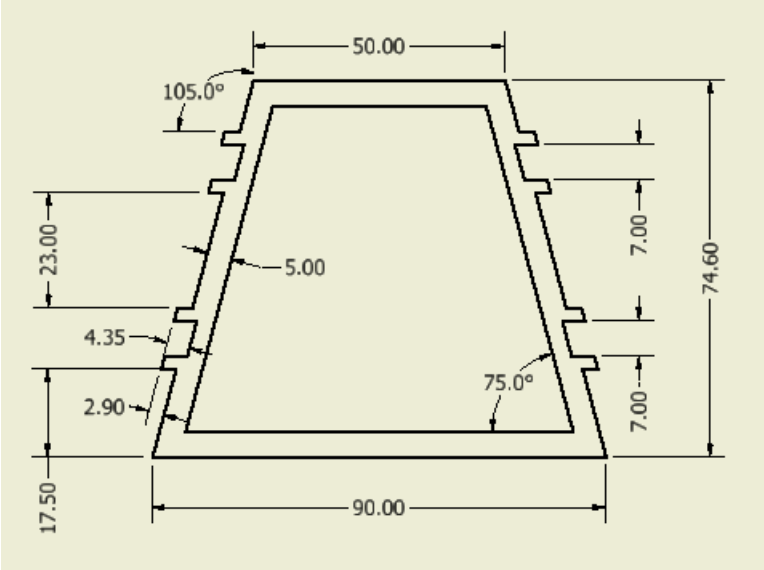

Figure B.152. Female Pyramid - Front

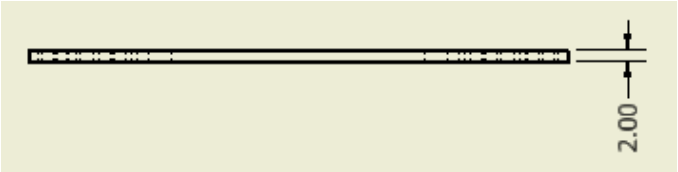

Figure B.153. Female Pyramid - Side

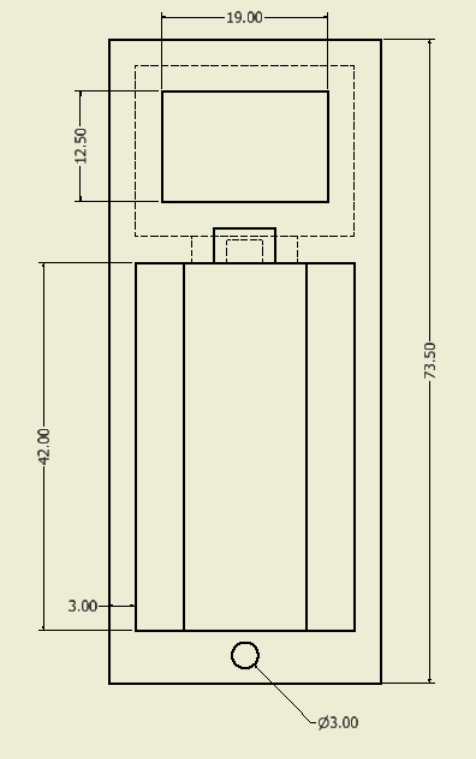

Figure B.154. Electronic Box - Front

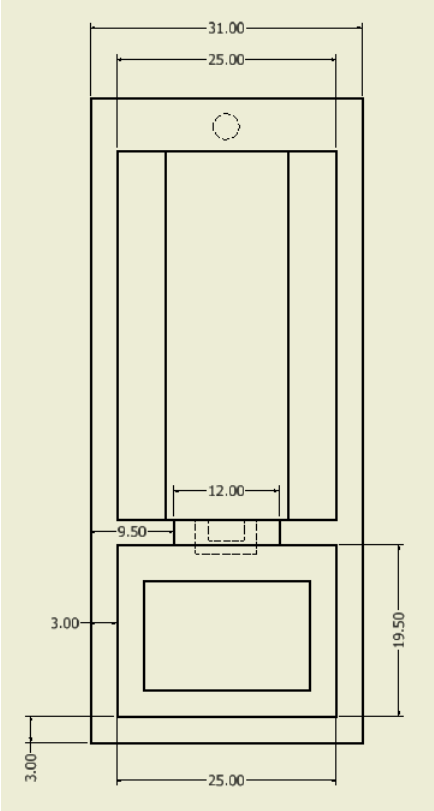

Figure B.155. Electronic Box - Bottom

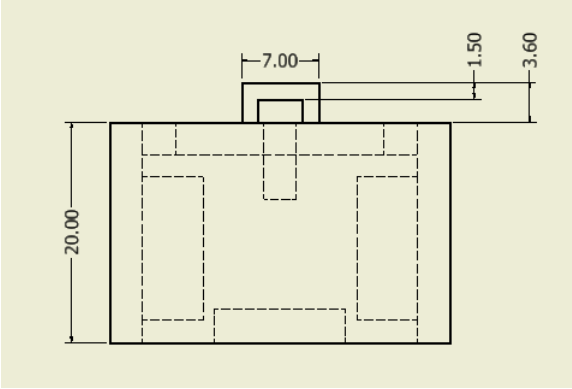

Figure B.156. Electronic Box - Top

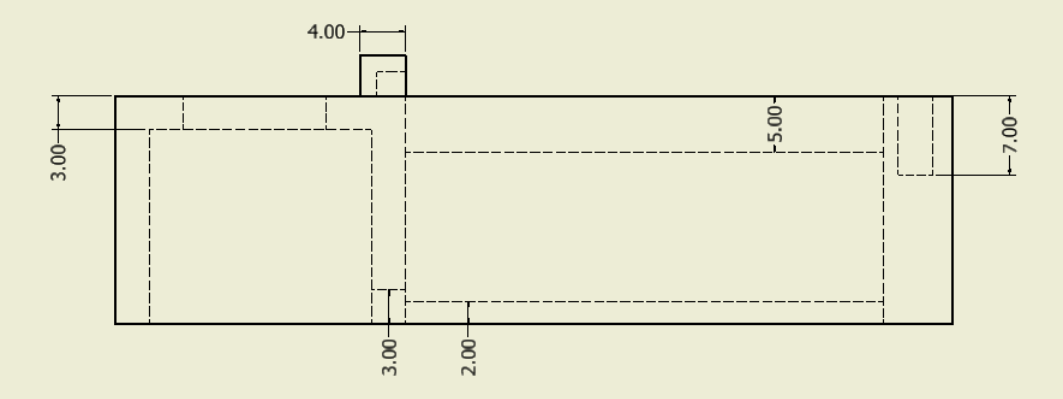

Figure B.157. Electronic Box - Side

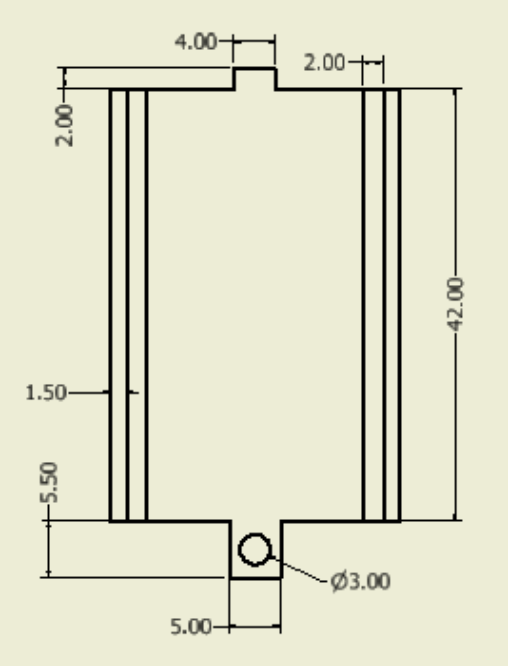

Figure B.158. Electronic Box Cover - Bottom

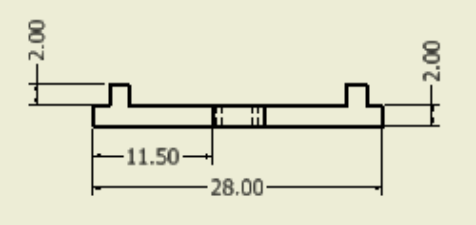

Figure B.159. Electronic Box Cover - Side

APPENDIX C

RGB App

This Appendix features the code behind some of the main features in the RGB App. The function responsible for retrieving RGB values from an image is shown below:

```
func getAvgPixelColorFromBox(box: UILabel) -> RGBValues {

        let pixelData = self.cgImage!.dataProvider!.data
        let data: UnsafePointer<UInt8> = CFDataGetBytePtr(pixelData)
        var counter: Float = 0
        var R: Float = 0
        var G: Float = 0
        var B: Float = 0
        let pos = box.frame.origin
        let width = box.frame.size.width
        let height = box.frame.size.height

        var RH: [Float] = []
        var BH: [Float] = []
        var GH: [Float] = []
        var IH: [Float] = []

        for i in Int(pos.x + 1)...Int(pos.x + width - 1) {
            for j in Int(pos.y + 1)...Int(pos.y + height - 1) {
                let point = CGPoint(x: i, y: j)
                let pixelInfo = ((Int(self.size.width) * Int(point.y)
) + Int(point.x)) * 4
                let r = CGFloat(data[pixelInfo])
                RH.append(Float(r))
```

```
                let g = CGFloat(data[pixelInfo+1])
                GH.append(Float(g))
                let b = CGFloat(data[pixelInfo+2])
                BH.append(Float(b))
                let intensity = 0.299*r + 0.587*g + 0.114*b
                IH.append(Float(intensity))
                counter += 1
                R += Float(r)
                G += Float(g)
                B += Float(b)
            }
        }

        let avgR = R / counter
        let avgG = G / counter
        let avgB = B / counter

        return RGBValues(red: avgR, green: avgG, blue: avgB, rh: RH,
    gh: GH, bh: BH, ih: IH)
    }
```

The camera view controller code which features UI components, API calls, an functions is shown below:

```
//
//  ViewController.swift
//  RGB
//
//  Created by Brenno Ribeiro on 9/1/18.
//  Copyright 2018 Brenno Ribeiro. All rights reserved.
//

import UIKit
```

```
import AVFoundation
import CoreData
import CoreLocation

var RH = [Float]()
var GH = [Float]()
var BH = [Float]()
var IH = [Float]()

enum flashState {
    case on
    case off
}

enum modeState {
    case Phosphate
    case Nitrate
    case pH
}

class CameraVC: UIViewController, CLLocationManagerDelegate {

    var captureSession: AVCaptureSession!
    var cameraOutput: AVCapturePhotoOutput!
    var previewLayer: AVCaptureVideoPreviewLayer!
    let locationManager = CLLocationManager()

    var photoData: Data?

    var flashControlState: flashState = .off
    var mode: modeState = .Phosphate
```

```
var lvl = 0

var latitude = "-"
var longitude = "-"

// IB Outlets
@IBOutlet weak var cameraView: UIView!
@IBOutlet weak var dash: UIView!
@IBOutlet weak var sizingLbl: UILabel!
@IBOutlet weak var captureImageView: UIImageView!
@IBOutlet weak var rgbLbl: UILabel!
@IBOutlet weak var shapeSelector: UIButton!
@IBOutlet weak var shapeView: RoundedShadowView!
@IBOutlet weak var previewImageView: UIImageView!
@IBOutlet weak var flashBtn: UIButton!
@IBOutlet weak var modeBtn: UIButton!
@IBOutlet weak var modeView: UIView!
@IBOutlet weak var advancedStatsBtn: UIButton!
@IBOutlet weak var dataBtn: RoundedShadowButton!


// Mode Btns
@IBOutlet weak var phosphateBtn: UIButton!
@IBOutlet weak var nitrateBtn: UIButton!
@IBOutlet weak var pHBtn: UIButton!

// Constraint Outlets
@IBOutlet weak var dashHeight: NSLayoutConstraint!
@IBOutlet weak var shapeViewWidth: NSLayoutConstraint!
@IBOutlet weak var flashBtnY: NSLayoutConstraint!
@IBOutlet weak var modeViewHeight: NSLayoutConstraint!
```

```
let shapeLayer = CAShapeLayer()
let circleLayer = CAShapeLayer()
var shapeStatus = "square"

override func viewDidLoad() {
    super.viewDidLoad()

    let width = self.cameraView.frame.size.width
    let height = self.cameraView.frame.size.height
    let trueWidthCenter = ceil(cameraView.frame.origin.x + width
/ 2)
    print(trueWidthCenter)
    let trueHeightCenter = ceil(cameraView.frame.origin.y +
height / 2)
    print(trueHeightCenter)
    let boxWidth = CGFloat(90)
    let boxHeight = CGFloat(90)
    let heightPos = height / 2 - boxHeight / 2
    shapeViewWidth.constant = 0
    modeViewHeight.constant = 0
    phosphateBtn.isHidden = true
    nitrateBtn.isHidden = true
    pHBtn.isHidden = true
    advancedStatsBtn.isHidden = true

    shapeLayer.bounds = CGRect(x: 0, y:0, width: boxWidth, height
: boxHeight)
    shapeLayer.lineWidth = 1
    shapeLayer.fillColor = nil
    shapeLayer.strokeColor = UIColor.red.cgColor
    shapeLayer.path = UIBezierPath(rect: shapeLayer.bounds).
cgPath
```

```
        shapeLayer.position = CGPoint(x: trueWidthCenter, y:
trueHeightCenter)
        self.view.layer.addSublayer(shapeLayer)
        sizingLbl.frame.origin.x = shapeLayer.frame.origin.x
        sizingLbl.frame.origin.y = heightPos
        sizingLbl.frame.size = shapeLayer.frame.size

        let circlePath = UIBezierPath(arcCenter: CGPoint(x:
trueWidthCenter,y: trueHeightCenter), radius: CGFloat(70),
startAngle: CGFloat(0), endAngle:CGFloat(Double.pi * 2), clockwise
: true)

        circleLayer.path = circlePath.cgPath

        // change the fill color
        circleLayer.fillColor = UIColor.clear.cgColor
        circleLayer.strokeColor = UIColor.red.cgColor
        circleLayer.lineWidth = 1

        view.layer.addSublayer(circleLayer)
        circleLayer.isHidden = true

        modeBtn.setTitle(" Mode: \(mode)", for: .normal)
        modeBtn.backgroundColor = #colorLiteral(red: 0.3452148438,
green: 0.8467610677, blue: 1, alpha: 0.4574593322)

        // location
        locationManager.requestWhenInUseAuthorization()
        if CLLocationManager.locationServicesEnabled() {
            locationManager.delegate = self
            locationManager.desiredAccuracy =
kCLLocationAccuracyNearestTenMeters
```

```
            locationManager.startUpdatingLocation()
        }

        updateWeather()

        _ =  Timer.scheduledTimer(timeInterval: 120.0, target: self,
    selector: #selector(updateWeather), userInfo: nil, repeats: true)

    }

    override func viewWillAppear(_ animated: Bool) {
        super.viewWillAppear(animated)

        let tap = UITapGestureRecognizer(target: self, action: #
    selector(didTapCameraView))
        tap.numberOfTapsRequired = 1

        let zoom = UIPinchGestureRecognizer(target:self, action: #
    selector(pinch))

        captureSession = AVCaptureSession()
//          captureSession.sessionPreset = .photo

        let backCamera = AVCaptureDevice.default(for: AVMediaType.
    video)

        if (backCamera?.isFocusModeSupported(.continuousAutoFocus))!
    {
            try! backCamera!.lockForConfiguration()
            backCamera!.focusMode = .continuousAutoFocus
            print("Focusing")
            backCamera!.unlockForConfiguration()
```

```
        }

        // White Balance
        if (backCamera?.isWhiteBalanceModeSupported(.locked))! {
            try! backCamera!.lockForConfiguration()
            backCamera?.setWhiteBalanceModeLocked(with:
    AVCaptureDevice.WhiteBalanceGains.init(redGain: 2.0, greenGain:
    1.0, blueGain: 2.0), completionHandler: nil)
//              backCamera!.whiteBalanceMode = .locked
            print(backCamera!.deviceWhiteBalanceGains)
            print("White")
            print(backCamera!.whiteBalanceMode.rawValue)
            backCamera!.unlockForConfiguration()
        }

        // Exposure
        if (backCamera?.isExposureModeSupported(.custom))! {
            try! backCamera!.lockForConfiguration()
            print(backCamera!.activeFormat.minISO)
            print(backCamera!.activeFormat.maxISO)
            backCamera?.setExposureModeCustom(duration: CMTime(value:
     1, timescale: 180), iso: backCamera!.activeFormat.minISO,
    completionHandler: nil)
            print("Exposure")
            print(backCamera!.exposureMode)
            print(backCamera!.exposureDuration)
//              backCamera?.exposureMode = .locked
            backCamera!.unlockForConfiguration()
        }

        do {
            let input = try AVCaptureDeviceInput(device: backCamera!)
```

```
            if captureSession.canAddInput(input) == true {
                captureSession.addInput(input)
            }

            cameraOutput = AVCapturePhotoOutput()

            if captureSession.canAddOutput(cameraOutput) == true {
                captureSession.addOutput(cameraOutput!)
                captureSession.commitConfiguration()

                previewLayer = AVCaptureVideoPreviewLayer(session:
captureSession!)
                previewLayer.videoGravity = AVLayerVideoGravity.
resizeAspect
                previewLayer.connection?.videoOrientation =
AVCaptureVideoOrientation.portrait

                cameraView.layer.addSublayer(previewLayer!)
                cameraView.addGestureRecognizer(tap)
                cameraView.addGestureRecognizer(zoom)
                captureSession.startRunning()
            }
        } catch {
            debugPrint(error)
        }
    }

    @objc func didTapCameraView() {
        let settings = AVCapturePhotoSettings()

        let previewPixelType = settings.
availablePreviewPhotoPixelFormatTypes.first!
```

```
        let previewFormat = [kCVPixelBufferPixelFormatTypeKey as
String: previewPixelType, kCVPixelBufferWidthKey as String: 160,
kCVPixelBufferHeightKey as String: 160]

        settings.previewPhotoFormat = previewFormat

        if flashControlState == .off {
            settings.flashMode = .off
        } else {
            settings.flashMode = .on
        }

        advancedStatsBtn.isHidden = false
        dashHeight.constant = 180 // Default: 150
        cameraOutput.capturePhoto(with: settings, delegate: self)
    }

    override func viewDidAppear(_ animated: Bool) {
        super.viewDidAppear(animated)
        previewLayer.frame = cameraView.bounds
    }


    func analyzeRGB(box: UILabel) {
        switch shapeStatus {
        case "square":
            let RGB = captureImageView.image?.getAvgPixelColorFromBox
(box: box)
            RGBValuesSetup(RGB: RGB!)
        case "circle":
            let RGB = captureImageView.image?.
getAvgPixelColorFromCircle(box: box)
```

```
            RGBValuesSetup(RGB: RGB!)
        default:
            break
        }
    }

    func RGBValuesSetup(RGB: RGBValues) {
        switch mode {
        case .Phosphate:
            lvl = phosphateLvl(red: RGB.red)
        case .Nitrate:
            lvl = nitrateLvl(red: RGB.red)
        case .pH:
            lvl = pHLvl(green: RGB.green)
        }
        rgbLbl.text = "Red: \(RGB.red) \nGreen: \(RGB.green) \nBlue:
\(RGB.blue) \nIntensity \(0.299*RGB.red + 0.587*RGB.green + 0.114*
RGB.blue)\n\(mode): \(lvl) ppm"
        RH = (RGB.rh)
        GH = (RGB.gh)
        BH = (RGB.bh)
        IH = (RGB.ih)

        if let locValue: CLLocationCoordinate2D = self.
locationManager.location?.coordinate {
            latitude = String(format: "%.3f", locValue.latitude)
            longitude = String(format: "%.3f", locValue.longitude)
        } else {
            latitude = "-"
            longitude = "-"
        }
```

```
        let temperature = currentTemperature
        let humidity = currentHumidity
        storeRGBData(date: Date(), location: latitude + ", " +
longitude, chemical: "\(mode)", concentration: lvl, temperature:
temperature, humidity: humidity)
    }

    func newMode(newMode: modeState, color: UIColor) {
        modeViewHeight.constant = 0
        phosphateBtn.isHidden = true
        nitrateBtn.isHidden = true
        pHBtn.isHidden = true
        mode = newMode
        modeBtn.backgroundColor = color
        modeBtn.setTitle(" Mode: \(mode)", for: .normal)
    }

    var selectorState = 0

    @IBAction func shapeSelectorBtnWasPressed(_ sender: Any) {
        if selectorState == 0 {
            shapeViewWidth.constant = 60
            flashBtnY.constant = shapeView.frame.height + 15
            selectorState = 1
        }
        else {
            shapeViewWidth.constant = 0
            flashBtnY.constant = 10
            selectorState = 0
        }
    }
```

```
@IBAction func squareBtnWasPressed(_ sender: Any) {
    shapeChange(shape: "square")
    selectorState = 0
}


@IBAction func circleBtnWasPressed(_ sender: Any) {
    shapeChange(shape: "circle")
    selectorState = 0
}

func shapeChange(shape: String) {
    shapeSelector.setImage(UIImage(named: "shapeSelector-\(shape)
"), for: .normal)
    if shape == "circle" {
        self.shapeLayer.isHidden = true
        self.circleLayer.isHidden = false
    } else {
        self.shapeLayer.isHidden = false
        self.circleLayer.isHidden = true
    }
    shapeViewWidth.constant = 0
    flashBtnY.constant = 10
    shapeStatus = shape
}

@IBAction func flashBtnWasPressed(_ sender: Any) {
    switch flashControlState {
    case .off:
        flashBtn.setImage(UIImage(named: "flashOn"), for: .normal
)
        flashControlState = .on
```

```
        case .on:
            flashBtn.setImage(UIImage(named: "flashOff"), for: .
normal)
            flashControlState = .off
        }
    }

    @IBAction func modeBtnWasPressed(_ sender: Any) {
        modeViewHeight.constant = 150
        phosphateBtn.isHidden = false
        nitrateBtn.isHidden = false
        pHBtn.isHidden = false
    }

    @IBAction func phosphateBtnWasPressed(_ sender: Any) {
        newMode(newMode: .Phosphate, color: #colorLiteral(red:
0.3452148438, green: 0.8467610677, blue: 1, alpha: 0.4574593322))
    }

    @IBAction func nitrateBtnWasPressed(_ sender: Any) {
        newMode(newMode: .Nitrate, color: #colorLiteral(red:
0.9204101563, green: 0.5655110677, blue: 1, alpha: 0.4574593322))
    }

    @IBAction func pHBtnWasPressed(_ sender: Any) {
        newMode(newMode: .pH, color: #colorLiteral(red: 0.3894585504,
 green: 0.8467610677, blue: 0.335015191, alpha: 0.4574593322))
    }

    @IBAction func advancedStatsBtnWasPressed(_ sender: Any) {
        performSegue(withIdentifier: "advancedStatsSegue", sender:
nil)
```

```
}

@IBAction func dataBtnWasPressed(_ sender: Any) {
    performSegue(withIdentifier: "dataSegue", sender: nil)
}



let minimumZoom: CGFloat = 1.0
let maximumZoom: CGFloat = 3.0
var lastZoomFactor: CGFloat = 1.0

@objc func pinch(_ pinch: UIPinchGestureRecognizer) {
    guard let device = AVCaptureDevice.default(for: AVMediaType.
video) else { return }

    // Return zoom value between the minimum and maximum zoom
values
    func minMaxZoom(_ factor: CGFloat) -> CGFloat {
        return min(min(max(factor, minimumZoom), maximumZoom),
device.activeFormat.videoMaxZoomFactor)
    }

    func update(scale factor: CGFloat) {
        do {
            try device.lockForConfiguration()
            defer { device.unlockForConfiguration() }
            device.videoZoomFactor = factor
        } catch {
            print("\(error.localizedDescription)")
        }
    }
```

```
        let newScaleFactor = minMaxZoom(pinch.scale * lastZoomFactor)

        switch pinch.state {
        case .began: fallthrough
        case .changed: update(scale: newScaleFactor)
        case .ended:
            lastZoomFactor = minMaxZoom(newScaleFactor)
            update(scale: lastZoomFactor)
        default: break
        }
    }

    func storeRGBData(date: Date, location: String, chemical: String,
    concentration: Int, temperature: String, humidity: String) {
        let appDelegate = UIApplication.shared.delegate as!
AppDelegate
        let context = appDelegate.persistentContainer.viewContext
        let newData = NSEntityDescription.insertNewObject(
forEntityName: "RGB_Data", into: context)
        newData.setValue(date, forKey: "date")
        newData.setValue(location, forKey: "location")
        newData.setValue(chemical, forKey: "chemical")
        newData.setValue(concentration, forKey: "concentration")
        newData.setValue(temperature, forKey: "temperature")
        newData.setValue(humidity, forKey: "humidity")

        do {
            try context.save()
            print("SAVED")
        } catch
        {
```

```
                print("ERROR")
            }
        }

        // Weather data timer

        @objc func updateWeather()
        {
            if let locValue: CLLocationCoordinate2D = self.
        locationManager.location?.coordinate {
                let urlString = "http://api.openweathermap.org/data/2.5/
        weather?lat=\(locValue.latitude)&lon=\(locValue.longitude)"
                WeatherService().getWeatherData(urlString: urlString)
            }
        }

}

extension CameraVC: AVCapturePhotoCaptureDelegate {
    func photoOutput(_ output: AVCapturePhotoOutput,
    didFinishProcessingPhoto photo: AVCapturePhoto, error: Error?) {
        if let error = error {
            debugPrint(error)
        } else {
            photoData = photo.fileDataRepresentation()

            let image = UIImage(data: photoData!)
            self.captureImageView.image = image
            analyzeRGB(box: sizingLbl)

            let backCamera = AVCaptureDevice.default(for: AVMediaType
        .video)
```

```
        print(backCamera?.exposureDuration)

        func cropImage(image: UIImage, toRect rect: CGRect) ->
UIImage? {
            var rect = rect
            print("scale: \(image.scale)")
            rect.size.width = rect.width * image.scale
            rect.size.height = rect.height * image.scale
            print("rect width: \(rect.width)")
            print("rect height: \(rect.height)")
            print("rect x: \(rect.minX) \(rect.maxX)")
            guard let imageRef = image.cgImage?.cropping(to: rect
) else {
                return nil
            }

            let contextImage: UIImage = UIImage(cgImage: image.
cgImage!)
            let contextSize: CGSize = contextImage.size
            print(contextSize.height)
            print(contextSize.width)

            let croppedImage = UIImage(cgImage:imageRef, scale:
image.scale, orientation: image.imageOrientation)
            return croppedImage
        }

        func cropBottomImage(image: UIImage) -> UIImage {
            print(self.view.frame.width)
            print(self.view.frame.height)
            let rect = CGRect(x: self.view.frame.height + 70, y:
self.view.frame.width - 70, width: 420, height: 420)
```

```
                return cropImage(image: image, toRect: rect)!
            }

            let newImg = cropBottomImage(image: image!)
            self.previewImageView.image = newImg
        }
    }
}
```

APPENDIX D

Lab-on-Chip Device Schematics

Schematics and drawings for the lab-on-chip device are shown in this appendix. All dimensions and sizes are in mm.

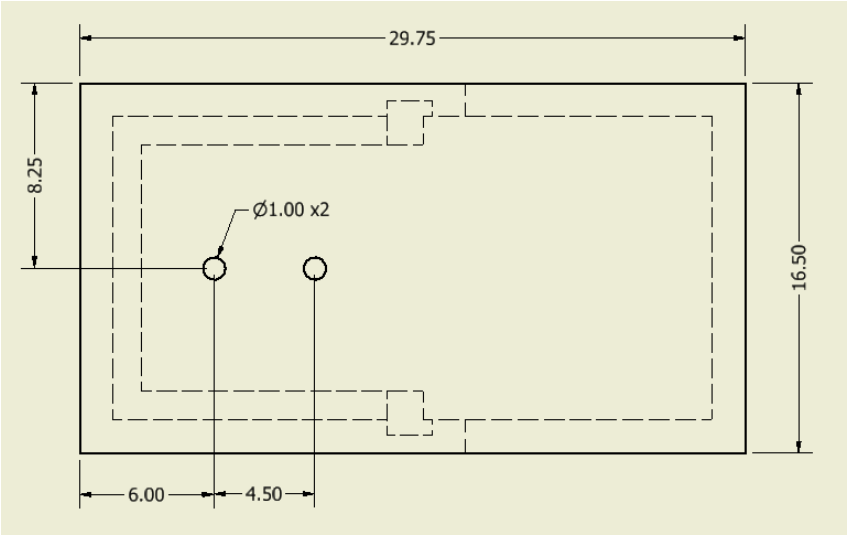

Figure D.160. LOC Base - Bottom

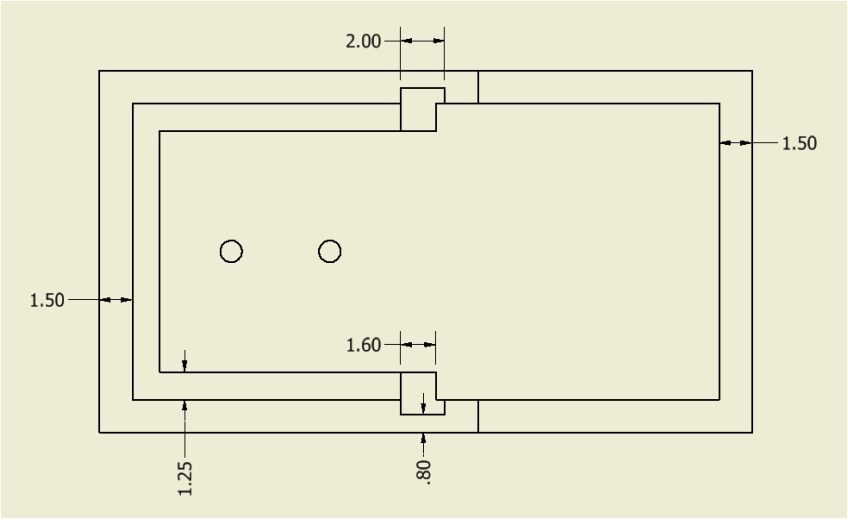

Figure D.161. LOC Base - Top

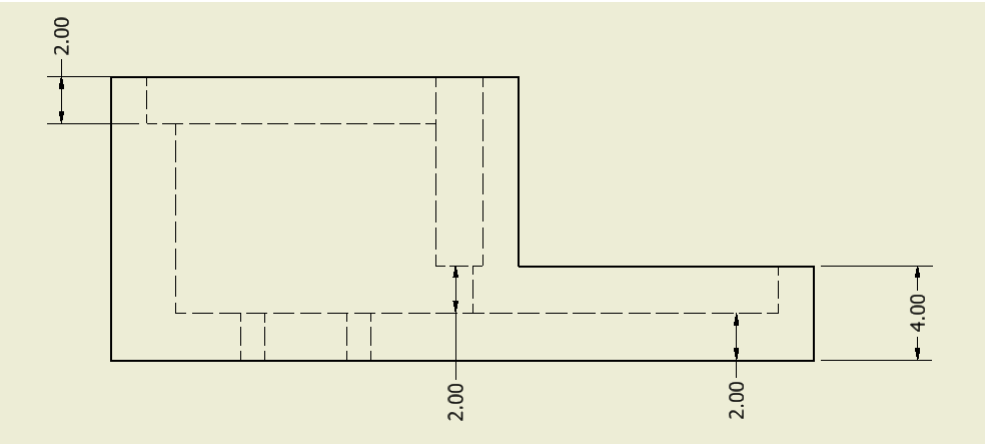

Figure D.162. LOC Base - Side

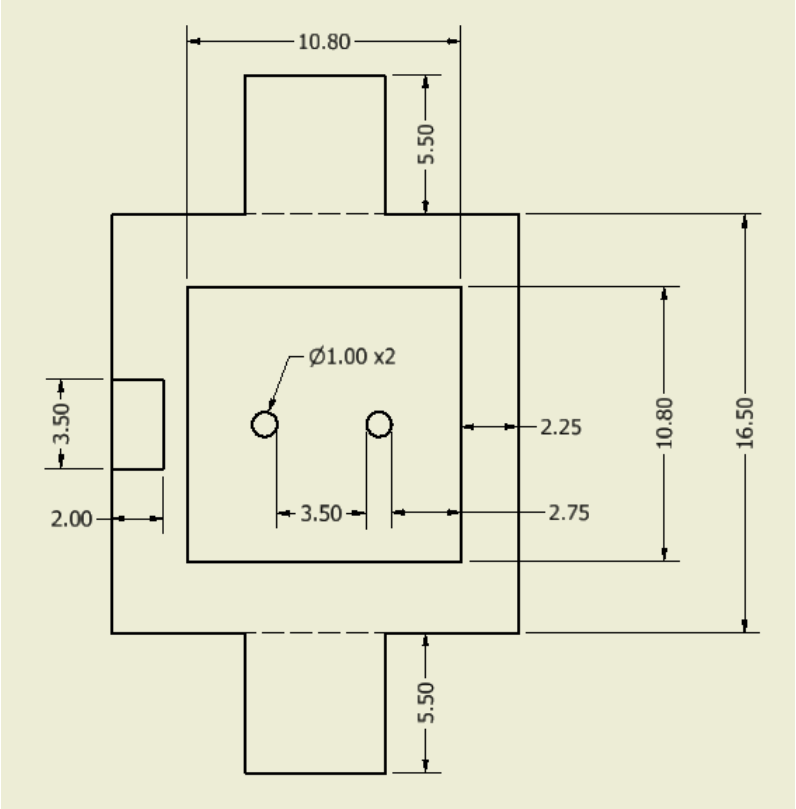

Figure D.163. LOC Button - Bottom

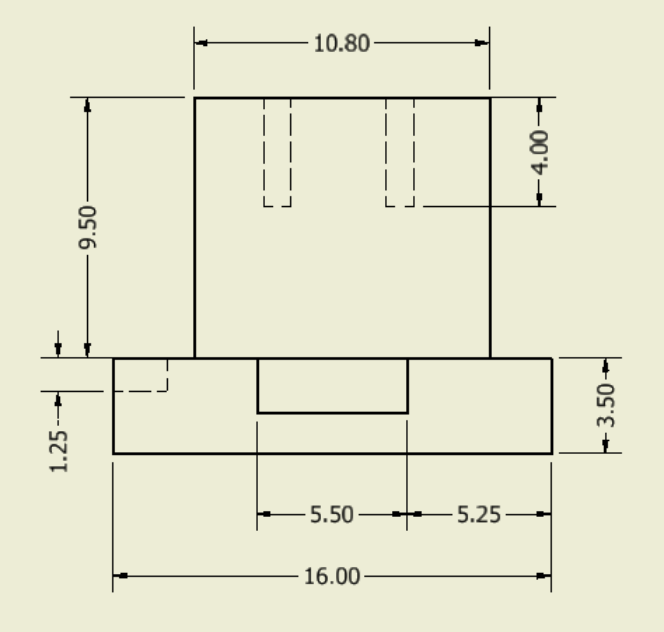

Figure D.164. LOC Button - Side

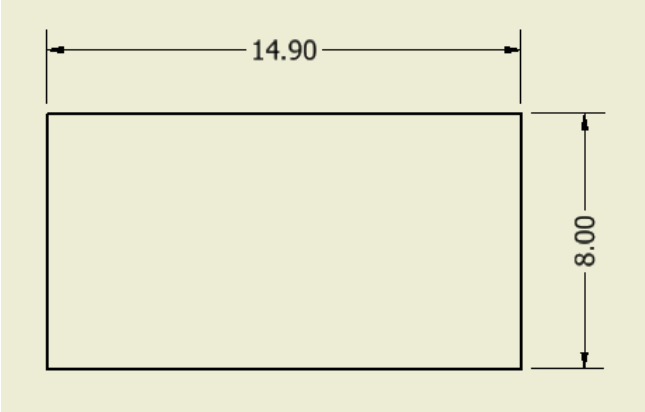

Figure D.165. LOC Sleeve - Top

Figure D.166. LOC Sleeve - Side

APPENDIX E

Infrared Box Schematics

Schematics and drawings for the infrared box are shown in this appendix. All dimensions and sizes are in mm.

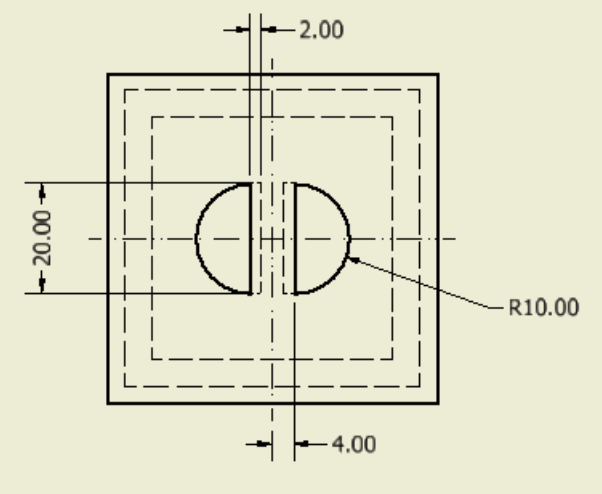

Figure E.167. IR Platform - Bottom

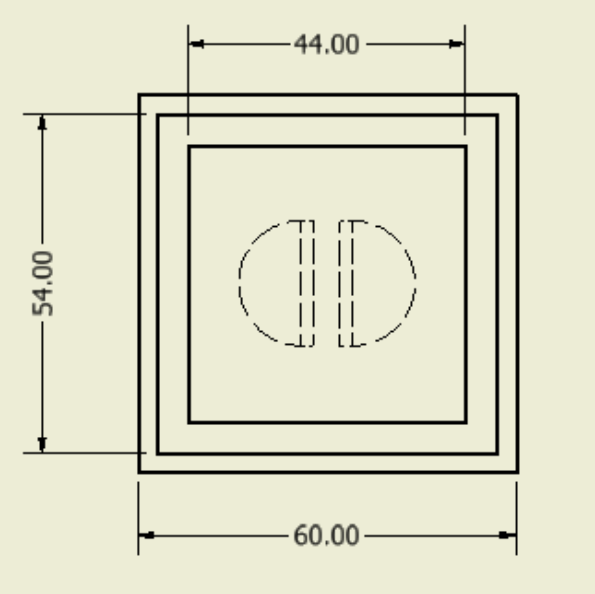

Figure E.168. IR Platform - Top

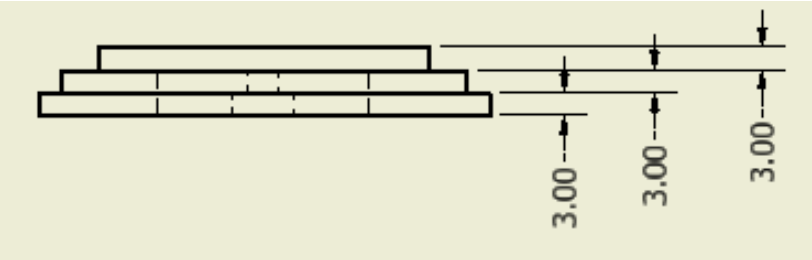

Figure E.169. IR Platform - Side

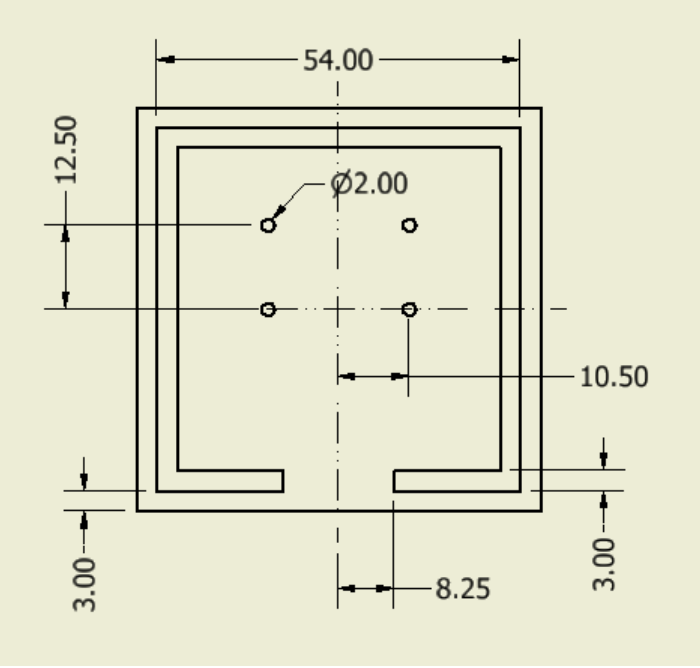

Figure E.170. IR Cover - Bottom

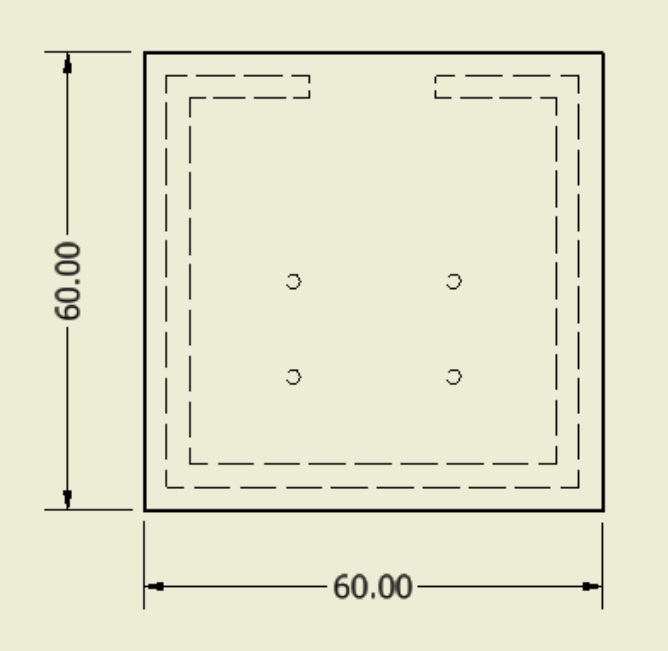

Figure E.171. IR Cover - Top

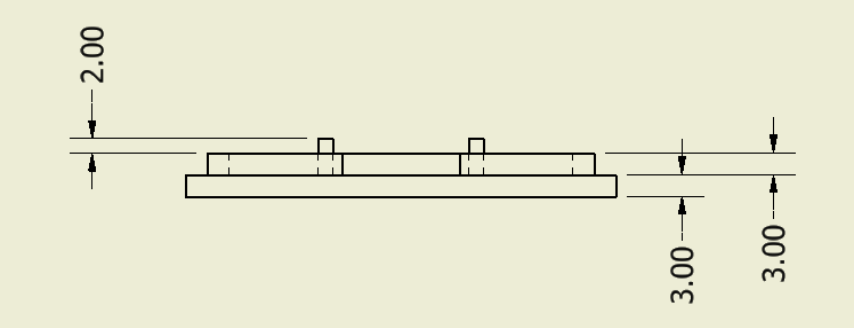

Figure E.172. IR Cover - Side

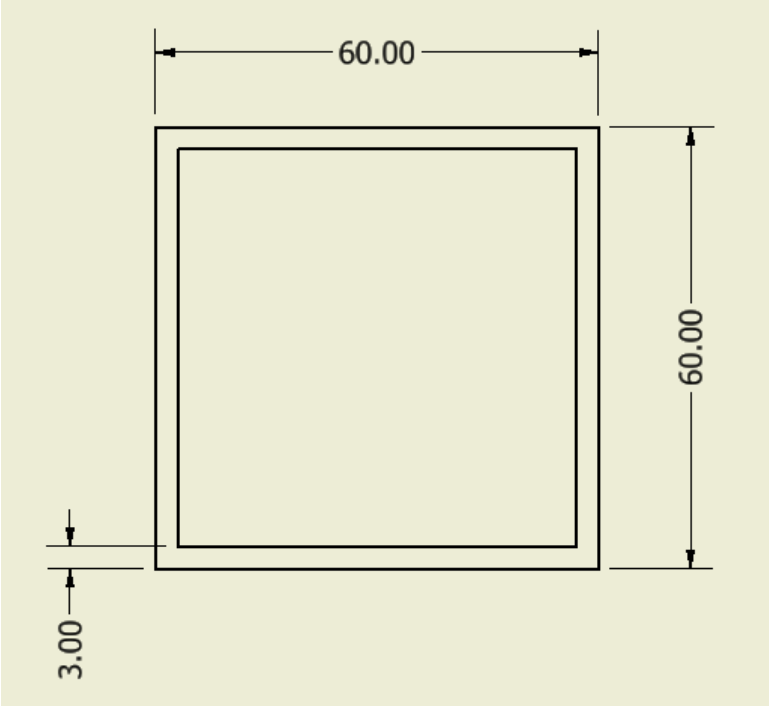

Figure E.173. IR Sleeve - Top

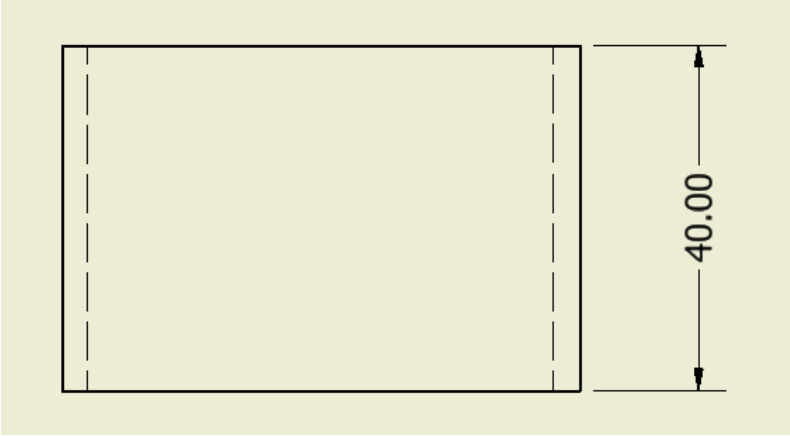

Figure E.174. IR Sleeve - Side

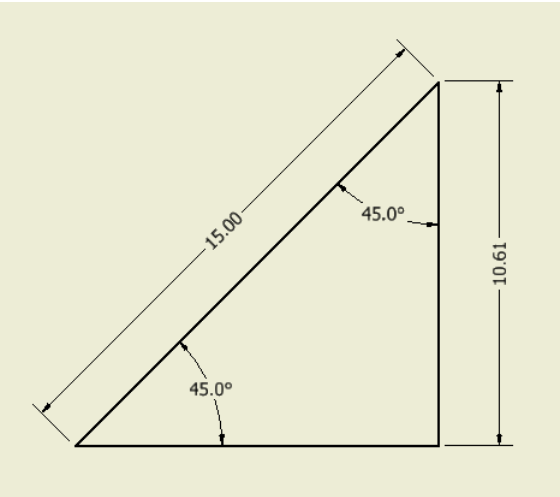

Figure E.175. IR Support - Top

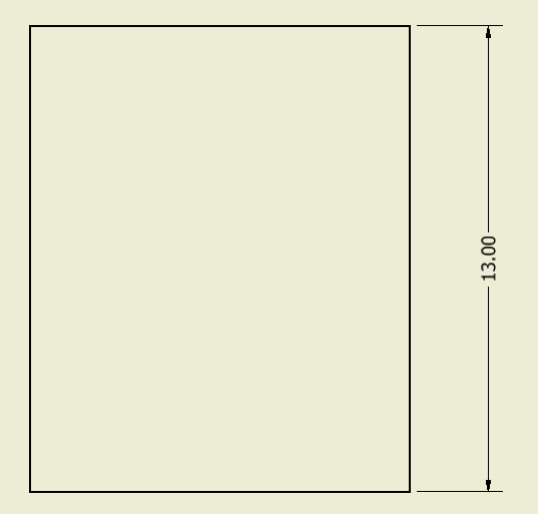

Figure E.176. IR Support - Side

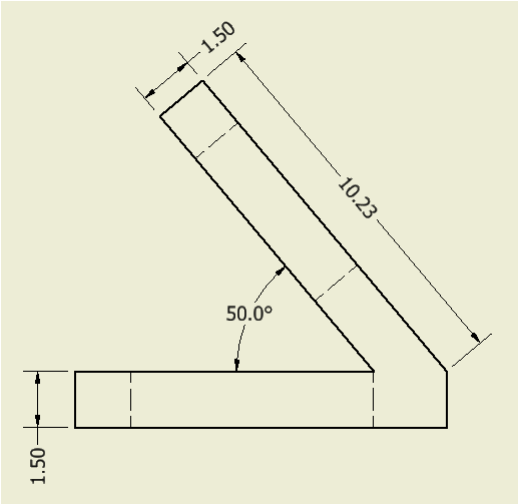

Figure E.177. IR Bracket - Side

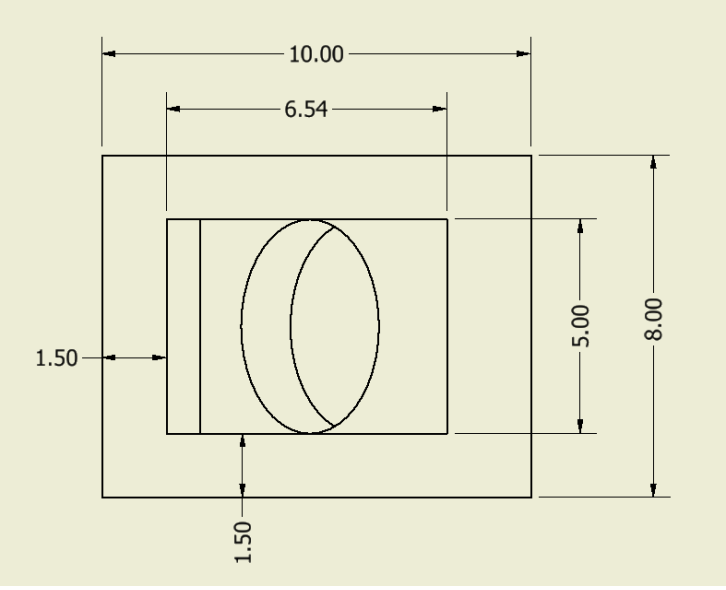

Figure E.178. IR Bracket - Bottom

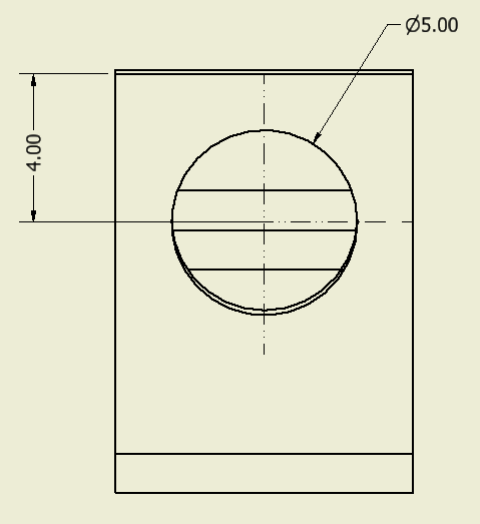

Figure E.179. IR Bracket - Top

BIBLIOGRAPHY

Abgrall, P. and Gué, A.-M., "Lab-on-chip technologies: making a microfluidic network and coupling it into a complete microsystem—a review," *Journal of Micromechanics and Microengineering*, vol. 17, 2007.

Abi-Samra, K., Hanson, R., Madou, M., and III, R. A. G., "Infrared controlled waxes for liquid handling and storage on a cd-microfluidic platform," *Lab on a Chip*, vol. 11, 2011.

Affinity Designer. "Affinity designer." December 2018. [Online]. Available: https://affinity.serif.com/en-us/designer/

Agency, U. S. E. P., "A compilation of cost data associated with the impacts and control of nutrient pollution," United States Environmental Protection Agency, Tech. Rep., 2015.

Anderson, D. M., Kaoru, Y., and White, A. W., "Estimated annual economic impacts from harmful algal blooms (habs) in the united states," Woods Hole Oceanographic Institution, Tech. Rep., 2000.

Appalachian State University. "Spectral sensitivity of photoreceptors." January 2019. [Online]. Available: http://www.appstate.edu/~steelekm/classes/psy3215/Color/absorption_spectrum.jpg

Apple. "Swift 4." December 2018. [Online]. Available: https://developer.apple.com/swift/

Apple. "Xcode 10." December 2018. [Online]. Available: https://developer.apple.com/xcode/

Ara, S., "The influence of water quality on the demand for residential development around lake erie," Ph.D. dissertation, The Ohio State University, 2007.

Aspila, K. I., Agemian, H., and Chau, A. S. Y., "A semi-automated method for the determination of inorganic, organic and total phosphate in sediments," *Analyst*, vol. 101, 1976.

Autodesk. "Inventor." November 2018. [Online]. Available: https://www.autodesk.com/products/inventor/overview

Bartlett, E. M. and Lewis, D. H., "Spectrophotometric determination of phosphate esters in the presence and absence of orthophosphate," *Analytical Biochemistry*, vol. 36, 1970.

Bartlett, E. M. and Lewis, D. H., "Spectrophotometric determination of phosphate esters in the presence and absence of orthophosphate," *Analytical Biochemistry*, vol. 36, 1970.

Bayer, B. E., United States of America Patent US3 971 065A, 1975.

Bootstrap. "Bootstrap." December 2018. [Online]. Available: https://getbootstrap.com/

Brand, L. E., Pablo, J., Compton, A., Hammerschlag, N., and Mash, D. C., "Cyanobacterial blooms and the occurrence of the neurotoxin, beta-n-methylamino-l-alanine (bmaa), in south florida aquatic food webs," *Harmful Algae*, vol. 9, 2010.

Brigham Young University. "Regions of the electromagnetic spectrum." January 2019. [Online]. Available: https://www.physics.byu.edu/faculty/christensen/physics%20137/Figures/Energy/Regions%20of%20the%20Electromagnetic%20Spectrum.htm

Bwambok, D. K., Christodouleas, D. C., Morin, S. A., Lange, H., Phillips, S. T., and Whitesides, G. M., "Adaptive use of bubble wrap for storing liquid samples and performing analytical assays," *Analytical Chemistry*, vol. 86, 2014.

Chen, H., Cogswell, J., Anagnostopoulos, C., and Faghri, M., "A fluidic diode, valves, and a sequential-loading circuit fabricated on layered paper," *Lab on a Chip*, vol. 12, 2012.

Cinti, S., Talarico, D., Palleschi, G., Moscone, D., and Arduini, F., "Novel reagentless paper-based screen-printed electrochemical sensor to detect phosphate," *Analytica Chimica Acta*, vol. 919, 2016.

CocoaPods. "Cocoapods." December 2018. [Online]. Available: https://cocoapods.org/

CorelDRAW. "Coreldraw." December 2018. [Online]. Available: https://www.coreldraw.com/en/

Correll, D., "Phosphorus: a rate limiting nutrient in surface waters," *Poultry Science*, vol. 78, 1999.

Czurratis, D., Beyl, Y., Zinober, S., Zengerle, R., and Lärmer, F., "Long-term on-chip storage and release of liquid reagents for diagnostic lab-on-a-chip applications," *International Journal of Physical and Mathematical Sciences*, vol. 7, 2013.

Darcy, H., *Les Fontaines Publiques de la Ville de Dijon*, 1856.

Denigès, G., *C. R. Acad. Sci.*, vol. 171, 1920.

Drummond, L. and Maher, W., "Determination of phosphorus in aqueous solution via formation of the phosphoantimonylmolybdenum blue complex reexamination of optimum conditions for the analysis of phosphate," *Analytica Chimica Acta*, vol. 302, 1995.

Edmund Optics. "Imaging electronics 101: Understanding camera sensors for machine vision applications." January 2019. [Online]. Available: https://www.edmundoptics.com/resources/application-notes/imaging/understanding-camera-sensors-for-machine-vision-applications/

ELEDLIGHTS.com. "A quick guide to lighting-related color temperatures." November 2018. [Online]. Available: https://www.eledlights.com/blog/post/a-quick-guide-to-lighting-color-temperature/

"Rapid lateral flow test strips: Considerations for product development," EMD Millipore.

Envato. "How to use white balance creatively." January 2019. [Online]. Available: https://photography.tutsplus.com/articles/how-to-use-white-balance-creatively--photo-9121

Evans, E., Gabriel, E. F. M., Coltro, W. K. T., and Garcia, C. D., "Rational selection of substrates to improve color intensity and uniformity on microfluidic paper-based analytical devices," *Analyst*, vol. 139, 2014.

Everlight. "Technical data sheet 5mm infrared led, t-1 3/4." February 2019. [Online]. Available: http://www.everlight.com/file/ProductFile/20140706153402694l.pdf

Fest, E., *Stray Light Analysis and Control*. SPIE Press, 2013, ch. 2.

Flask. "Flask." December 2018. [Online]. Available: http://flask.pocoo.org/

Fu, E., Ramsey, S. A., Kauffman, P., Lutz, B., and Yager, P., "Transport in two-dimensional paper networks," *Microfluidics and Nanofluidics*, vol. 10, 2011.

GitHub. "Alamofire." December 2018. [Online]. Available: https://github.com/Alamofire/Alamofire

GitHub. "Charts." December 2018. [Online]. Available: https://github.com/danielgindi/Charts

GitHub. "Swiftyjson." December 2018. [Online]. Available: https://github.com/SwiftyJSON/SwiftyJSON

Han, K. N., Choi, J.-S., and Kwon, J., "Three-dimensional paper-based slip device for one-step point-of-care testing," *Scientific Reports*, vol. 6, 2016.

He, Z. and Honeycutt, C. W., "A modified molybdenum blue method for orthophosphate determination suitable for investigating enzymatic hydrolysis of organic phosphates," *Communications in Soil Science and Plant Analysis*, vol. 36, 2005.

Hoffmann, J., Mark, D., Lutz, S., Zengerle, R., and von Stetten, F., "Pre-storage of liquid reagents in glass ampoules for dna extraction on a fully integrated lab-on-a-chip cartridge," *Lab on a Chip*, vol. 10, 2010.

Howarth, R. W., Sharpley, A., and Walker, D., "Sources of nutrient pollution to coastal waters in the united states: Implications for achieving coastal water quality goals," *Estuaries*, vol. 25, 2002.

Ibraheem, N. A., Hasan, M. M., Khan, R. Z., and Mishra, P. K., "Understanding color models: A review," *ARPN Journal of Science and Technology*, vol. 2, 2012.

Indigo Instruments. "Phosphate test strips." May 2018. [Online]. Available: https://www.indigoinstruments.com/test_strips/water_quality/phosphate-test-strips-100ppm-33817P.html

Irandoust, M., Shariati-Rad, M., and Haghighi, M., "Nitrite determination in water samples based on a modified griess reaction and central composite design," *Analytical Methods*, vol. 21, 2013.

Islam, S., Reza, M. N., Jeong, J.-T., and Lee, K.-H., "Sensing technology for rapid detection of phosphorus in water: A review," *Journal of Biosystems Engineering*, vol. 41, 2016.

Itaya, K. and Ui, M., "A new micromethod for the colorimetric determination of inorganic phosphate," *Clinica Chimica Acta*, vol. 14, 1966.

Jayawardane, B. M., Wongwilai, W., Grudpan, K., Kolev, S. D., Heaven, M. W., Nash, D. M., and McKelvie, I. D., "Evaluation and application of a paper-based device for the determination of reactive phosphate in soil solution," *Journal of Environmental Quality*, vol. 43, 2014.

Jayawardane, B., McKelvie, I. D., and Kolev, S. D., "A paper-based device for measurement of reactive phosphate in water," *Talanta*, vol. 100, 2012.

Jonca, J., Fernández, V. L., Thouron, D., Paulmier, A., Graco, M., and Garçon, V., "Phosphate determination in seawater: Toward an autonomous electrochemical method," *Talanta*, vol. 87, 2011.

Jonca, J., Fernández, V. L., Thouron, D., Paulmier, A., Gracoc, M., and Garcon, V., "Phosphate determination in seawater: Toward an autonomous electrochemical method," *Talanta*, vol. 87, 2011.

Jonca, J., Giraud, W., Barus, C., Comtat, M., Thouron, N. S. D., and Garçon, V., "Reagentless and silicate interference free electrochemical phosphate determination in seawater," *Electrochimica Acta*, vol. 88, 2013.

Knight, J. B., Vishwanath, A., Brody, J. P., and Austin, R. H., "Hydrodynamic focusing on a silicon chip: Mixing nanoliters in microseconds," *Physical Review Letters*, vol. 80, 1998.

Kong, T., Flanigan, S., Weinstein, M., Kalwa, U., Legner, C., and Pandey, S., "A fast, reconfigurable flow switch for paper microfluidics based on selective wetting of folded paper actuator strips," *Lab on a Chip*, vol. 17, 2017.

Koo, C. K. W., He, F., and Nugen, S. R., "An inkjet-printed electrowetting valve for paper-fluidic sensors," *Analyst*, vol. 138, 2013.

Lai, Y. ., Tsai, J. ., Hsu, J. ., and Lu, Y. ., "Automated paper-based devices by microfluidic timing-valve for competitive elisa," in *2017 IEEE 30th International Conference on Micro Electro Mechanical Systems (MEMS)*, 2017.

LEDsupply. "Waterproof ip65 led flex strip." November 2018. [Online]. Available: https://www.ledsupply.com/led-strips/waterproof-12v-led-strip

Lee, H. N., Swamy, K. M. K., Kim, S. K., Kwon, J.-Y., Kim, Y., Kim, S.-J., Yoon, Y. J., and Yoon, J., "Simple but effective way to sense pyrophosphate and inorganic phosphate by fluorescence changes," *Organic Letters*, vol. 9, 2007.

Li, X., Zwanenburg, P., and Liu, X., "Magnetic timing valves for fluid control in paper-based microfluidics," *Lab on a Chip*, vol. 13, 2013.

Li, X., Tian, J., Nguyen, T., and Shen, W., "Paper-based microfluidic devices by plasma treatment," *Analytical Chemistry*, vol. 80, 2008.

Linge, K. L. and Oldham, C. E., "Interference from arsenate when determining phosphate by the malachite green spectrophotometric method," *Analytica Chimica Acta*, vol. 450, 2001.

Liu, R. H., Stremler, M. A., Sharp, K. V., Olsen, M. G., Santiago, J. G., Adrian, R. J., Aref, H., and Beebe, D. J., "Passive mixing in a three-dimensional serpentine microchannel," *Journal of Microelectromechanical Systems*, vol. 9, 2000.

Liu, R. H., Yang, J., Lenigk, R., Bonanno, J., and Grodzinski, P., "Self-contained, fully integrated biochip for sample preparation, polymerase chain reaction amplification, and dna microarray detection," *Analytical Chemistry*, vol. 76, 2004.

Lucas, R., "Ueber das zeitgesetz des kapillaren aufstiegs von flüssigkeiten," *Colloid and Polymer Science*, vol. 23, 1918.

Lutz, B., Liang, T., Fu, E., Ramachandran, S., Kauffman, P., and Yager, P., "Dissolvable fluidic time delays for programming multi-step assays in instrument-free paper diagnostics," *Lab on a Chip*, vol. 13, 2013.

Macherey-Nagel. "Quantofix phosphate test strips." May 2018. [Online]. Available: http://www.mn-net.com/Testpapers/QUANTOFIXteststrips/QUANTOFIXPhosphat/tabid/10335/language/en-US/Default.aspx

Mackenthun, K. M., Ed., *Toward a Cleaner Aquatic Environment*. Washington, DC, United States of America: Environmental Protection Agency Office of Air and Water Programs, 1973.

Michelsen, O. B., "Photometric determination of phosphorus as molybdovanadophosphoric acid," *Analytical Chemistry*, vol. 29, 1957.

Misson, G., *Chemiker Zeitung*, vol. 32, 1908.

Moran, S. K. Scientific American. "Wastewater is key to reducing nitrogen pollution." April 2018. [Online]. Available: https://www.scientificamerican.com/article/wastewater-is-key-to-reducing-nitrogen-pollution/

Motomizu, S., Oshima, M., and Ojima, Y., "Spectrophotometric determination of silicate in water with molybdate and malachite green," *Analytical Sciences*, vol. 5, 1989.

Murphy, J. and Riley, J. P., "A modified single solution method for the determination of phosphate in natural waters," *Analytica Chimica Acta*, vol. 27, 1962.

N, T., B, Z., E, S., E, L., A, A., T, C., J, H., W, B., PL, H., and X, S., "Assessing cyanobacterial harmful algal blooms as risk factors for amyotrophic lateral sclerosis," *Neurotoxicity Research*, vol. 33, 2018.

National Institutes of Health. "Imagej." September 2018. [Online]. Available: https://imagej.nih.gov/ij/

National Oceanic and Atmospheric Administration. "Gulf of mexico 'dead zone' is the largest ever measured." April 2018. [Online]. Available: http://www.noaa.gov/media-release/gulf-of-mexico-dead-zone-is-largest-ever-measured

National Oceanic and Atmospheric Administration. "What is nutrient pollution?" May 2018. [Online]. Available: https://oceanservice.noaa.gov/facts/nutpollution.html

Nikon. "Setting white balance." January 2019. [Online]. Available: https://www.nikonusa.com/en/learn-and-explore/a/tips-and-techniques/setting-white-balance.html

Nikon. "Understanding iso sensitivity." January 2019. [Online]. Available: https://www.nikonusa.com/en/learn-and-explore/a/tips-and-techniques/understanding-iso-sensitivity.html

Nikon. "Understanding maximum aperture." January 2019. [Online]. Available: https://www.nikonusa.com/en/learn-and-explore/a/tips-and-techniques/understanding-maximum-aperture.html

Noh, H. and Phillips, S. T., "Metering the capillary-driven flow of fluids in paper-based microfluidic devices," *Analytical Chemistry*, vol. 82, 2010.

of Sciences, N. A., Ed., *Managing Wastewater in Coastal Urban Areas*. Washington, DC, United States of America: National Academies Press, 1993.

of Sciences, N. A., Ed., *Clean Coastal Waters: Understanding and Reducing the Effects of Nutrient Pollution*. Washington, DC, United States of America: National Academy Press, 2000.

Ohno, T. and Zibilske, L. M., "Determination of low concentrations of phosphorus in soil extracts using malachite green," *Soil Science Society of America*, vol. 55, 1991.

OpenWeatherMap. "Weather api." December 2018. [Online]. Available: https://openweathermap.org/api

Oram, B. Water Research Center. "Phosphate in surface water streams lakes." May 2018. [Online]. Available: https://www.water-research.net/index.php/phosphate-in-water

Patey, M. D., Rijkenberg, M. J., Statham, P. J., Stinchcombe, M. C., Achterberg, E. P., and Mowlem, M., "Determination of nitrate and phosphate in seawater at nanomolar concentrations," *Trends in Analytical Chemistry*, vol. 27, 2008.

PetaPixel. "The exposure triangle: Making sense of aperture, shutter speed, and iso." January 2019. [Online]. Available: https://petapixel.com/2017/03/25/exposure-triangle-making-sense-aperture-shutter-speed-iso/

Photography Life. "Introduction to shutter speed in photography." January 2019. [Online]. Available: https://photographylife.com/what-is-shutter-speed-in-photography

Pitchaimani, K., Sapp, B. C., Winter, A., Gispanski, A., Nishida, T., and Fan, Z. H., "Manufacturable plastic microfluidic valves using thermal actuation," *Lab on a Chip*, vol. 21, 2009.

Posthuma-Trumpie, G. A., Korf, J., and van Amerongen, A., "Lateral flow (immuno)assay: its strengths, weaknesses, opportunities and threats. a literature survey," *Analytical and Bioanalytical Chemistry*, vol. 393, 2009.

Puckett, L. J., "Identifying the major sources of nutrient water pollution," *Environmental Science and Technology*, vol. 29, 1995.

raise3d. "ideamaker." November 2018. [Online]. Available: https://www.raise3d.com/pages/ideamaker

raise3d. "Raise3d n2 plus." November 2018. [Online]. Available: https://www.raise3d.com/pages/raise3d-n2-plus

Raspberry Pi. "Pi noir camera v2." February 2019. [Online]. Available: https://www.raspberrypi.org/products/pi-noir-camera-v2/

Raspberry Pi. "Raspberry pi 3 model b+." February 2019. [Online]. Available: https://www.raspberrypi.org/products/raspberry-pi-3-model-b-plus/

Raspberry Pi. "Raspbian." February 2019. [Online]. Available: https://www.raspberrypi.org/downloads/raspbian/

Read the Docs - Pi Camera. "Advanced recipes." February 2019. [Online]. Available: https://picamera.readthedocs.io/en/release-1.12/recipes2.html#raw-bayer-data-captures

Rezk, A. R., Qi, A., Friend, J. R., Li, W. H., and Yeo, L. Y., "Uniform mixing in paper-based microfluidic systems using surface acoustic waves," *Lab on a Chip*, vol. 12, 2012.

Royal Society of Chemistry. "Phosphorus." May 2018. [Online]. Available: http://www.rsc.org/periodic-table/element/15/phosphorus

Sanseverino, I., Conduto, D., Pozzoli, L., Dobricic, S., and Lettieri, T., "Algal bloom and its economic impact," European Commission Joint Research Centre, Tech. Rep., 2016.

Schmaltz, J., NASA Earth Observatory.

science photo. Shutterstock. "photo id: 311155133." May 2018. [Online]. Available: https://www.shutterstock.com/image-photo/lab-on-chip-device-integrates-several-311155133?src=cLdu2ev8R_VMau9l2tqYCw-1-3

Swinehart, D., "The beer-lambert law," *Journal of Chemical Education*, vol. 39, 1962.

ThermoFisher Scientific. "Phosphate sensor: Pv4406." May 2018. [Online]. Available: https://www.thermofisher.com/order/catalog/product/PV4406

Thingiverse. "Raspberry pi 3 (b/b+), pi 2 b, and pi 1 b+ case with vesa mounts and more." February 2019. [Online]. Available: https://www.thingiverse.com/thing:922740

Thonny. "Thonny." February 2019. [Online]. Available: https://thonny.org/

United States Environmental Protection Agency. "The mississippi/atchafalaya river basin (marb)." April 2018. [Online]. Available: https://www.epa.gov/ms-htf/mississippiatchafalaya-river-basin-marb

United States Environmental Protection Agency. "Septic systems overview." April 2018. [Online]. Available: https://www.epa.gov/septic/septic-systems-overview

Walji, N. and MacDonald, B. D., "Influence of geometry and surrounding conditions on fluid flow in paper-based devices," *Micromachines*, vol. 7, 2016.

Washburn, E. W., "The dynamics of capillary flow," *The Physical Review*, vol. 17, 1921.

Wines, M. The New York Times. "Behind toledo's water crisis, a long-troubled lake erie." April 2018. [Online]. Available: https://www.nytimes.com/2014/08/05/us/lifting-ban-toledo-says-its-water-is-safe-to-drink-again.html

Zhang, J.-Z., Fischer, C. J., and Ortner, P. B., "Optimization of performance and minimization of silicate interference in continuous flow phosphate analysis," *Talanta*, vol. 49, 1998.

Zhao, H. X., Liu, L. Q., Liu, Z. D., Wang, Y., Zhao, X. J., and Huang, C. Z., "Highly selective detection of phosphate in very complicated matrixes with an off–on fluorescent probe of europium-adjusted carbon dots," *Chemical Communications*, vol. 47, 2011.